An experimental study of single hole spin qubit coherence in a GaAs/AlGaAs double quantum dot device

by

Victor John Marton

A thesis

presented to the University of Waterloo

in fulfillment of the

thesis requirement for the degree of

Master of Science

in

Physics (Quantum Information)

Waterloo, Ontario, Canada, 2024

Author's Declaration

This thesis consists of material all of which I authored or co-authored: see Statement of Contributions included in the thesis. This is a true copy of the thesis, including any required final revisions, as accepted by my examiners.

I understand that my thesis may be made electronically available to the public.

Statement of Contributions

Before the experiments detailed in this thesis began, a great deal of preliminary and preparatory work was performed by various members of the research group at the National Research Council (NRC) in Ottawa. This included the initial testing of various similar devices in order to identify the premier candidate for further experimentation, the wiring of the dilution refrigerator, the modification of hardware such as bias tees, and the creation of software libraries to control the utilized hardware were all conducted in the years prior to my own involvement in the project. These preparations were followed by a number of experiments leading to papers, all of which built towards the beginning of the project contained in this thesis. The contributing researchers include Drs. Sergei Studenikin, Alex Bogan, Andrew Sachrajda, Marek Korkusinski, Guy Austing, and Louis Gaudreau, as well as Piotr Zawadski. The device was itself fabricated at Sandia National Laboratories by Lisa Tracy, John Reno, and Terry Hargett.

My own contribution to this project spans all of the experiments whose results are presented in this thesis, except where otherwise specified. Together with Drs. Studenikin and Bogan, I helped to plan each of the experiments. Using the "Platypus" library originally created by Dr. Bogan to control the hardware at the laboratory, I produced the code to perform these experiments. As well, I was tasked with the daily maintenance of the wet dilution refrigerator, including the regular filling with liquid helium. After collecting the data, I also processed the data by iterating on Dr. Bogan's initial code. I created all figures and diagrams in this thesis, as well as in the paper published based on this research, except where otherwise specified.

Abstract

This thesis discusses a series of experiments performed on a p-type laterally-gated GaAs/AlGaAs double quantum dot device [1]. The main purpose of these experiments was to explore the potential of a theoretically-predicted increase in the spin coherence time T_2^* for the usage of a single hole pseudo-spin in GaAs, as opposed to a conduction-band electron.

The "Introduction" section provides a brief overview of the history of the Loss-DiVincenzo spin qubit and the motivation to iterate upon its implementations in light of the DiVincenzo criteria for quantum computing. It also places the experiments in this thesis in context with regard to preceding experiments of a similar nature performed in the same research group.

The "Relevant Background Information" section provides an exploration of a number of topics that aid the non-expert in familiarizing themselves with the principles of semiconductor quantum dots, understanding the functionality of the device and methods used, and interpreting the results of the experiments.

The "Readout" section explains the process by which the single-shot experiments and spin-to-charge readout scheme are prepared, performed, and detected by room-temperature electronics. The process by which the various tunneling times of the system are tuned in order for the pulsing scheme to function is then discussed. Finally, the energy level alignments for successful hole transfer are identified experimentally.

The "Results and Discussion" section presents and describes the results of the various experiments performed in order to fully characterize the coherence characteristics of the device. Following successful spin excitation via EDSR, the state of the hole pseudo-spin was manipulated via Rabi experimentation. Methods for maximizing device performance are motivated, explained, and displayed. The coherence times T_2^* and T_2^{CPMG} are then determined via Ramsey, Hahn-echo, and CPMG experiments. These results are then discussed and compared to contemporaries. The spin relaxation time T_1 is extracted and compared with previous results on the same device. Finally, an additional functionality is explored in which the dot effective g-factor is tuned electrically via gate voltage pulsing within each single-shot experiment.

Acknowledgments

Throughout my time as a graduate student at the University of Waterloo, I have had the pleasure of collaborating with numerous experts from the National Research Council, as well as from the University itself. On many an occasion, I have recognized the privilege of "standing on the shoulders of giants", so to speak, and though it is not possible to thank each of them properly in so short an excerpt, I will make an attempt, nonetheless.

Foremost, I would like to extend my gratitude my co-supervising professors, Drs. Sergei Studenikin and Jan Kycia. It has been through their support that I ever came to be a student at the University of Waterloo. In particular, I would like to thank Sergei for spending such a great deal of his time and effort to include me directly in such a fascinating project. Through this help, I was fortunate enough to join a promising project *in medias res*, timed perfectly to partake in the culmination of a years-long endeavour and produce meaningful results. Together with Drs. Jonathan Baugh and Robert Hill, these four gentlemen also made up my advisory and thesis defense committees, providing me with ample guidance throughout the culmination of two years' work. I would like to thank the four of them once again for their support.

I would also like to express my sincerest thanks to Piotr Zawadzki. Undoubtedly, Piotr has had a profound contribution to my graduate work; beyond "just" his expertise with regard to cryogenics, which he selflessly shared with me out of his own volition, Piotr has been an invaluable friend. I hope now, with his well-deserved retirement upon him, Piotr will be able to turn his attention to sharpening his chess acumen.

My earnest appreciation is also extended to Drs. Andy Sachrajda, Marek Korkusinski, Louis Gaudreau, and Guy Austing for providing direct and indirect support of my research, both through thought-provoking discussions and explicit feedback upon my writing and presentations. It has proven invaluable to have had the chance to take part in the research process with each of you. Many thanks also to the NRC for allowing me to conduct my research at their facilities in Ottawa. These experiments, and indeed this thesis, could not have existed without such an opportunity.

I would also like to express particular gratitude to Dr. Alex Bogan, whose breadth and depth of expertise was made available to me unconditionally and at any time; a particular incident involving an overnight power outage at the NRC exemplifies this disposition. Alex is an excellent researcher and a selfless individual, donating his help to me even when it was inconvenient for him to do so.

Any academic endeavour of mine owes substantial attribution to the continued support of Dr. Justin Teeuwen. Justin has taught me a great deal within and beyond the classroom as a mentor and friend. Certainly, he is deserving of hearty approbation and lavish praise.

Finally, it is my great pleasure to highlight and appreciate the immense contribution of my mother, Irene Marton. Her unwavering support underpins all of my achievements. Surely, nothing I can write on a page is sufficient to express my gratitude.

Dedication

This thesis is dedicated to Irene, Zoltan, and Jessica Marton.

Table of Contents

List of Figures

List of Tables

List of Abbreviations

2DHG: Two-dimensional hole gas

AWG: Arbitrary waveform generator

CPMG: Carr-Purcell-Meiboom-Gill

DQD: Double quantum dot

EDSR: Electric dipole spin resonance

GQF: Gate quality factor

MW: Microwave

NMR: Nuclear magnetic resonance

QD: Quantum dot

QQF: Qubit quality factor

RF: Radio frequency

SD: Stability diagram

SOI: Spin-orbit interaction

TN: Telegraphic noise

Introduction

Before the idea of quantum computing was introduced, a proposal for reversible computing was presented by Rolf Landauer in 1961 [2], highlighting how classical computing methods lose energy to the environment while destroying information. Yuri Manin and Richard Feynman proposed quantum computing as a solution to this issue in 1980 [3] and 1981 [4], respectively, beginning the search for a successful implementation of the scheme. By employing the phenomena of superposition and entanglement, quantum computers perform operations encoded in the quantum mechanical properties of subatomic particles and thus cannot be fully simulated on their classical counterparts. In the many years since their proposal, it has been demonstrated theoretically that once sufficiently large arrays of quantum computing bits, or qubits, are assembled, quantum computers will outperform their classical counterparts in specific applications such as the Deutsch-Jozsa [5], Grover's search [6], and Shor's prime factoring algorithms [7]. The strength of Shor's algorithm in factoring large numbers necessitates that security systems must be redeveloped in the case that the creation of large-scale quantum computers becomes feasible. In order to be realized, quantum computers must first overcome the hurdles of error correction, state decoherence, and scalability, necessary characteristics for a quantum computer outlined by DiVincenzo's Criteria [8].

The first physical implementations of quantum logic gates were realized on the Cirac-Zoller trapped ion infrastructure for a controlled-NOT (CNOT) gate [9] by Monroe et al. in 1995 [10]. Other implementations were theorized and realized concurrently, such as quantum operator expectation value measurements via nuclear magnetic resonance (NMR) by Cory et al. in 1997 [11]. It was in the same year that Loss and DiVincenzo [12] proposed that quantum computations be performed using the spin states of electrons located on quantum dots. However, the usage of quantum dots in quantum computation was discussed as early as 1995 by Barenco et al [13]. in a paper that outlined two physical phenomena by which a CNOT gate could be realized using electron spins, including a lateral double quantum dot (DQD) device.

Since their inception, quantum dots (QDs) have been a promising candidate for the physical implementation of quantum computers. Also known as artificial atoms, semiconductor QDs are attractive in that existing manufacturing infrastructure can be co-opted to mass-produce them following the requisite modifications to the production process. Fabrication methods have matured for long-standing candidate materials such as gallium arsenide (GaAs), contributing to its longevity as a material of choice in QD fabrication. While silicon is ubiquitous in the fabrication of classical computers, the level of precision needed to create functional QDs consistently is higher than for modern transistors. In comparison, the relatively small effective mass of GaAs conductance band electrons permits larger dot geometry, reducing the need for precision. Nevertheless, the substantial coherence times measured on Si-based QD devices [14] [15] have motivated development in Si QD manufacturing techniques. By contrast, the decreased effective mass of holes in germanium allows QDs to be made larger, much like with GaAs devices, easing manufacturing constraints [16].

Quantum dots are engineered to reduce the spatial degrees of freedom of an electron, easing the electric manipulation of its spin state. The vertical layers of a laterally-gates QD device, as explored in the "Double Quantum Dot (DQD) Device" section below for the device used in the experiments covered by this work, include a contact of materials that produces a band structures that limits the motion of charge carriers to the two-dimensional interface of the layers. Electrostatic

gates placed over this interface deplete the two-dimensional "gas" of charge carriers underneath when an electric potential is applied, motivating the "laterally-gated" descriptor. The population of each QD can be controlled by "tuning" these gate voltages and observing the resultant changes in dot occupation. These devices must be kept at milli-Kelvin temperatures to reduce the occurrence of lattice vibrational modes ("phonons") and spin state excitations, both of which lead to the loss of quantum information due to environmental noise. The electronic properties of these dots can, however, be tuned via electrostatic gate voltages controlled by room-temperature electronics. As a testament of their future viability and scalability, laterally-gated QDs have been successfully created and tested in double [17] [18] [19], triple [20] [21] [22], and larger sets [23] [24] [25].

Each material used to implement semiconductor QD devices has its own advantages and disadvantages. In the case of recent QD devices implemented on germanium and silicon platforms, the lack of a direct band gap impedes their integration into hybrid quantum systems involving photonic information transfer. Gallium arsenide, while having a direct band gap, lacks where germanium and silicon excel: electronic QD qubits in GaAs suffer from much shorter spin coherence times than those in Ge and Si. This reduction is caused by the hyperfine interaction between the electron spins and the effective magnetic field produced by the nuclear spins of the lattice atomic nuclei. To overcome this difficulty, a change of carriers is an attractive prospect: a shift to holes is predicted to produce longer coherence times due to the lower hyperfine interaction of holes with the atomic nucleus in comparison to electrons [26] [27] [28]. The QDs in p-type devices, however, can be as much as 10 times smaller than their electron-based counterparts due to their greater effective mass: heavy holes in GaAs have an effective mass of 0.4 times the electron rest mass m_0, whereas electrons have mass $0.067m_0$ [1] [29]. This reduced size makes the fabrication of such devices at high quality more difficult, contributing to the historic lack of availability of hole QD devices.

The experiments in this work consist of the adaptation and testing of the latched spin-to-charge readout method in order to test the coherence time of the single-hole GaAs QD qubit using the pseudo-spin of a single heavy hole. However, a change of carrier type creates new challenges. Chiefly, the development of a new spin readout method is necessitated, as the Pauli spin blockade method is rendered inapt due to an increase in the strength of the spin-orbit interaction in the valence band. Isolating single carriers is no trivial task: a single electron was first successfully isolated in a lateral GaAs QD only in 2000 [30], while single-hole tunneling events were not observed until 2013 [31].

A single heavy hole was first successfully isolated on a GaAs/AlGaAs double quantum dot (DQD) device in 2017 [32] [33], after which a modified version of a "latched" hole spin-to-charge readout method proposed by Bogan et al. in 2019 [34] was applied. By observing the changes in the proportion of charge-detection measurements corresponding to the excited state of the hole, the coherence characteristics of the device were measured. Experiments involved Rabi, Ramsey, Hahn-echo, and CPMG pulsing schemes delivered via DC pulses and microwave oscillations in gate voltage that induce electric dipole spin resonance (EDSR) of the hole spin. The resultant spin state is then converted to the occupation of an auxiliary QD for charge sensing readout. These results constitute the first study of the coherence characteristics of a single hole spin of a semiconductor QD device conducted in the "latching regime", explored in detail in this thesis. The electric tuning of the effective "g-factor", a proportionality constant between the energy level difference between the spin states and the external magnetic field strength, is also demonstrated. This constitutes an important property for large-scale quantum computing applications.

Relevant Background Information

Electron Holes

The absence of an electron around an atom can be treated as a quasi-particle with a positive unit charge, called an electron hole or simply a "hole". In a semiconductor lattice, holes are produced when an electron is promoted to the conduction band and is allowed to move through the lattice. The absence of an electron that is left behind in the valence band is the hole, akin to a bubble of air in water. The movement of holes is therefore equivalent to the flow of positive charge (i.e., "conventional current") through a semiconductor lattice.

The collective behaviour of surrounding particles in the lattice makes holes equivalent to a positively charged particle with an effective mass and a pseudo-spin, henceforth referenced simply as the hole's spin. Holes can be categorized according to their effective mass into two groups: light and heavy holes. The Hamiltonian defined by the spin-orbit interaction between the lattice atomic nuclei and the angular momenta of the holes has two solutions, leading to the two possible effective masses [35].

On the Loss-DiVincenzo spin qubit, holes can be used as the charge carrier by encoding quantum information in their spin states rather than in the spin states of electrons. Though valence heavy holes have total spin 3/2, a two-level system can be defined that is analogous to that of a spin-1/2 particle by separating the heavy-hole band states (of $J = \pm 3/2$) from the light-hole band states (of $J = \pm 1/2$). It is predicted that due to the lower hyperfine interaction between atomic nuclei and holes in the valence band, the coherence times of such p-type spin qubit devices may be longer than their electron-based counterparts [36]. However, theoretical analysis such as those presented by Fischer et al. [26] [27] suggest that this benefit may sometimes be less significant than expected due to a mixing of the light and heavy hole subbands in dots caused by strain. Regardless, the potential for an increase in coherence times motivated an investigation of single-hole devices, leading to this project.

The Quantum Dot (QD), Gallium Arsenide (GaAs)

Quantum dots (QDs), also called artificial atoms, were first observed in glass by Alexei I. Ekimov et al. in 1981 [37]. The atom-like properties of QDs have made them, among other applications, a prime candidate for spin-qubit implementation. After the initial theoretical proposal for the QD spin qubit implementation by Loss and DiVincenzo in 1998 [12], many early semiconductor quantum dot qubits were implemented in n-type gallium arsenide (GaAs). The device employed in this work differs in that it implements a p-type QD structure.

GaAs long stood as the leading material for the experimental study of quantum phenomena due to the record-high carrier mobility ahead of other semiconductor structures available at the time. This was achieved via the technique of modulation doping, as first demonstrated by Dingle et al. in 1978 [38]. By means of molecular beam epitaxy, this process places dopant atoms in the AlGaAs layer sufficiently far from either of its boundaries to separate the electron donors from the GaAs/AlGaAs material interface at which the electrons are accumulated.

GaAs remains an apt material for semiconductor quantum devices due to its various advantageous properties:

1. Direct Band Gap

The band structure of a semiconductor material is an important consideration for spin qubit applicability. For semiconductor lattices with indirect band gaps such as germanium and silicon, electrons require both an increase in energy and a change in momentum in order to be promoted from the valence band edge to the conduction band edge. If an electron is promoted to higher-energy conduction band states that do align with the valence band edge, they may be promoted to an excited state or have an unpredictable momentum. This unpredictable behaviour can lead to decoherence if quantum information is encoded in the electron spin state. In contrast, lattices with direct band gaps, such as GaAs and InSb, require only an increase in energy, as the momentum of the valence and conduction band edge electrons is the same. This is an important property for future hybrid quantum devices, as the direct emission or absorption of a photon is required in such applications as quantum repeaters and entanglement distribution [39].

2. Strong spin-orbit coupling

In order for quantum computing to become a viable alternative to classical computation in any application, it is vital that gate operations be performed on minimal timescales. For semiconductor spin qubits, the rate at which spins can be manipulated depends on the strength of the spin-orbit coupling, covered in detail in the "Spin-Orbit Interaction (SOI)" section below. Experiments leading up to and including those in this work involve electrical manipulation of hole spins due to their strong spin-orbit interaction, giving p-type devices in GaAs the potential to perform gate operations at higher frequency than their electron-based counterparts [40].

3. Tunable effective hole g-factor

In the future, quantum computers must be scaled sufficiently in order to implement quantum algorithms involving numerous logical qubits, constituting a great number more physical qubits in order to perform the requisite error correction algorithms. Such scalability would be realized in semiconductor spin qubits via the creation of arrays of quantum dot qubits. To address individual qubits in the array while leaving the others unaltered, the Larmor frequency of the spin in any QD must be selectable. This functionality has been demonstrated on the same device used in this work by changing the effective hole g-factor by altering the angle of the applied magnetic field [32] and via the spin-orbit interaction with an ancillary QD [41]. In this thesis, an additional method is presented in the "Electrically Tunable Dot Effective g-Factor" section; gate voltages are altered within the single-shot cycle, causing a reproducible linear change in the effective g-factor.

4. Lower hyperfine interaction between holes & nuclei

Hole-based devices in GaAs were predicted to have longer coherence times due to reduced hyperfine interaction between holes and the nucleus in comparison to those of electrons [26] [27] [28]. The potential maximization of state coherence is vital for the successful implementation of quantum computers, making p-type devices attractive for further investigation.

The Loss-DiVincenzo Spin Qubit

Proposed in 1998 [12], the Loss-DiVincenzo qubit is a potential quantum computing implementation that encodes its quantum information in spin states of an electron (or hole) confined in a QD. The up and down states of an electron (or hole) spin constitute a well-defined two-level system. Qubit states can be prepared and controlled electronically through a universal set of one- and two-qubit gates. After the application of a quantum algorithm, the resultant states can then be measured via such readout techniques as the Elzerman and Pauli spin blockade methods [42] [43] [44].

Whether electrons or holes are used, carriers are confined in quantum dots laid out vertically or laterally. Gate voltage and/or magnetic field modulation are used to perform one- and two-qubit gate operations on coupled dots [45]. Semiconductor-based spin qubits benefit from a circumstantial advantage over other quantum computing implementations in that electronics manufacturing infrastructure can be repurposed to create quantum dot devices, though new challenges in device manufacture preclude a seamless transition.

The Double Quantum Dot (DQD) Device

The device upon which experiments were conducted in this work is a gate-defined lateral double quantum dot (DQD) implemented in a gallium arsenide/aluminum gallium arsenide (GaAs/AlGaAs) heterostructure and fabricated at Sandia National Labs in New Mexico [18] [33]. A scanning electron microscope (SEM) image of a similar device is shown in Figure 1. a).

The device was grown at a temperature of 630 degrees Celsius by means of molecular beam epitaxy and consists, from bottom to top, of the following layers, as shown in Figure 1.b):

0. GaAs substrate, upon which the layers are deposited

1. GaAs "buffer layer" - 300 nm

This "semi-insulating" [46, pp. 112113-1] layer is sufficiently thick to reduce the effect of any structural defects in the substrate on the remaining layers of the heterostructure that would impact performance. GaAs lattices tend to reduce their surface area during growth, meaning that uneven features of the surface upon which the crystal is grown are gradually smoothed.

2. "Superlattice" layer - 300 repetitions of the following alternating layers: 10 nm of $Al_{0.5}Ga_{0.5}As$, 3 nm of GaAs

This layer is deposited in order to reduce the strain that will be experienced by the epitaxial (top) layer. Impurities and structural defects, such as dislocations, are trapped at the interfaces of adjacent layers so that their effects are reduced or eliminated at the active layer. Given that the previous layer is a GaAs wafer, any defects and impurities originating in the substrate will still be present at its top surface. The alternating superlattice layers include planar crystals that gradually segregate impurities and reduce imperfections in the top layer.

a)

Courtesy of Sandia National Laboratories

b)
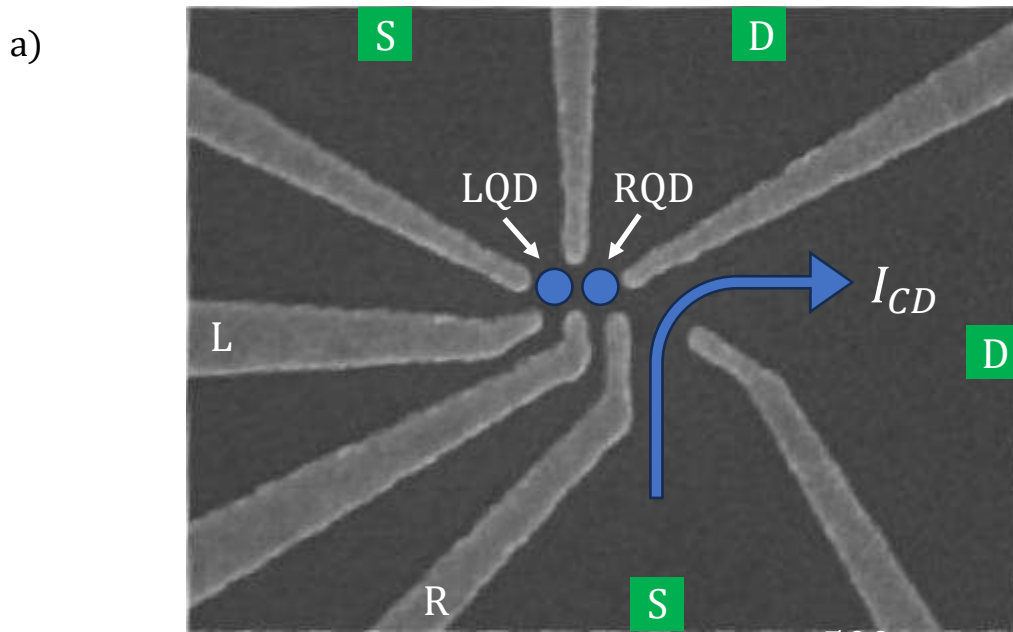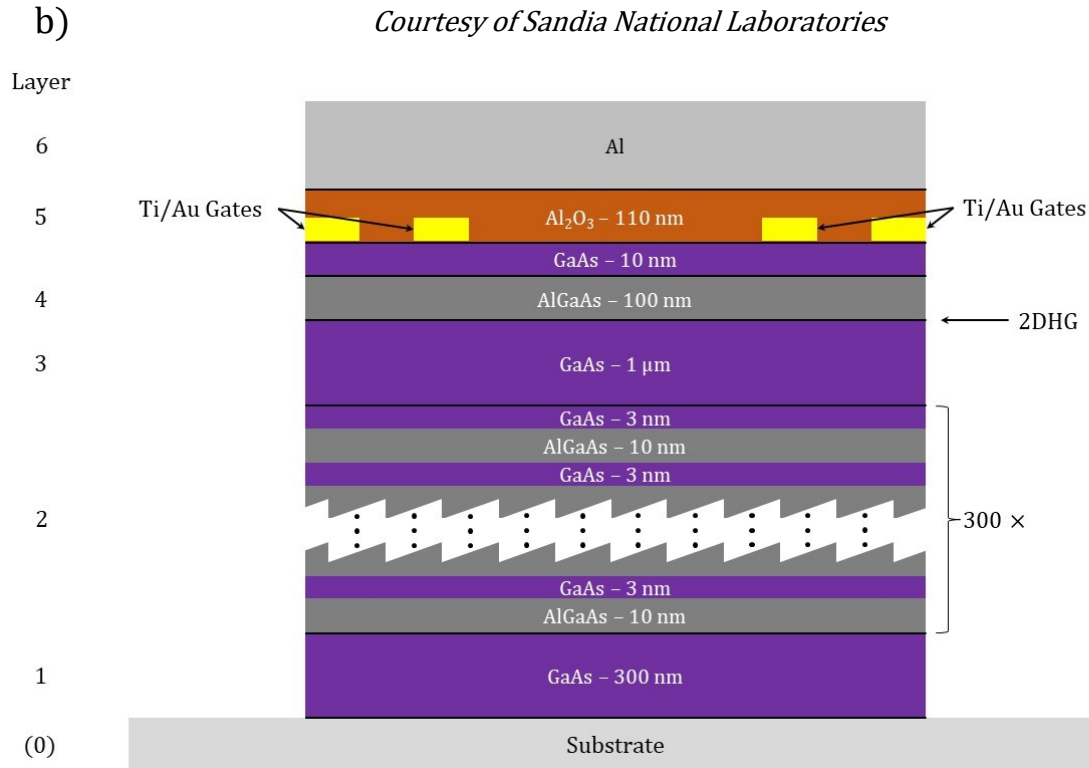
Figure 1: a) Scanning electron microscope image of a GaAs DQD device similar to the one used in this work. Not shown is the global gate that is located over the area in the image. The blue circles represent the approximate positions of the left and right quantum dots (LQD and RQD, respectively), while the large blue arrow on the right signifies the charge detection current I_{CD} that passes through the quantum point contact. The four green squares represent ohmic contacts, labelled "S" ("D") for "source" ("drain"); b) Illustration of the various layers of the device. Layer thicknesses are labelled but not to scale. Numbered layers are separated by a horizontal black line. The white dotted section of layer 2 replaces the many repetitions of alternating layers, the number of which is indicated. The location of the 2DHG is also labelled.

6

3. GaAs layer - 1 µm

The interface of the top surface of this layer with the bottom surface of the subsequent $Al_{0.5}Ga_{0.5}As$ layer accumulates the two-dimensional hole gas (2DHG) necessary for charge carrier confinement.

4. $Al_{0.5}Ga_{0.5}As$ "barrier layer" - 100 nm

This layer is made sufficiently thick to shield the below and above undoped GaAs layers from one another, thereby separating the 2DHG from non-active layers. Due to their different work functions, a transfer of charge occurs between GaAs and AlGaAs layers in contact, forming a p-n junction with a high potential difference. Holes are attracted to the negative voltage of the gates but cannot cross due to the potential barrier. Thus, these charge carriers accumulate at a potential minimum that forms adjacent to the interface of the two crystals, just inside the GaAs layer beneath.

5. GaAs "cap layer" - 10 nm

This layer separates the gates from direct contact with the AlGaAs layer while also preventing the oxidation of the AlGaAs when exposed to air, mitigating device aging.

6. Ti/Au depletion gates and Al_2O_3 insulating layer - 110 nm

This layer houses the Ti/Au depletion gates that define the DQD device, laid directly on top of the GaAs cap layer. When a voltage more positive than that of the global accumulation gate is applied to these gates, the 2DHG is depleted underneath to produce the desired geometry, separate the two QDs, and adjust the tunneling rates between the dots and reservoirs. The remainder of the layer is fulfilled with Al_2O_3 in order to insulate the gates from the overlaid global gate.

7. Al global accumulation gate layer

This layer is used to accumulate carriers in the 2DHG by applying a negative voltage over the entire area of the heterostructure. In comparison to the voltages applied to the gates below (± 0.5 V and smaller), the voltage applied to the global gate is much larger in magnitude (-6.6 V). This is necessary in order to produce sufficient carrier density due to its greater distance from the 2DHG.

Visible in Figure 1.a) in light gray are the seven Ti/Au depletion gates. Not shown are the Al_2O_3 insulating layer and the large global gate overlaid on top of the imaged layer. The left and right QDs are labeled LQD and RQD, respectively. The device is "gate-defined" in that the QDs are confined by the electric fields produced by the gates.

For experiments involving current flow across the device, the source-drain current I_{SD} is measured via the ohmic contacts attached to the leads at the top of the image (green squares). However, this method was not employed in the experiments in this body of work. Instead, the charge occupation of the dots was probed via a quantum point contact (QPC) created near the right QD by

the QPC gate at the bottom right of the SEM image in Figure 1.a). The characteristics of the quantum point contact are explored briefly in the "Quantum Point Contact (QPC)" section below.

Equipment and Experimental Apparatus

Semiconductor spin qubits require near-zero temperatures for operation, as the introduction of environmental noise is minimized. Only when the energy level splitting between the ground and excited states exceeds the magnitude of thermal excitations can randomly-occurring promotions to the excited state be eliminated. The exact temperature at which this condition is achieved differs by device due to factors such as its material composition. All experiments in this work were conducted while the GaAs/AlGaAs DQD device was cooled to ultra-low temperatures inside an Oxford Instruments Kelvinox-400 wet dilution refrigerator, with a carrier temperature of 102 mK measured on the device in previous experiments [47].

The sample mount consisted of nineteen Au contact voltage pins that were connected to the sample via aluminum bonding wires. To each pin, a specially-designed Cu DC voltage line was connected that was biased by room-temperature electronics outside of the fridge. These lines were each interrupted by a 60 cm segment of nichrome thermo-coax cable between the 1.5K and mixing chamber stages in order to insulate the system from high-frequency fluctuations in temperature and excessive thermal load [48].

In order to apply gate voltage changes from room-temperature electronics while the sample is supercooled, a total of 19 copper DC lines are routed to the sample mount from the top of the unit, including two ground lines. The sample remains thermally stable, as each of the lines is thermally anchored to two copper plates at the 1.5 K and mixing chamber stages.

Certain experiments in this work involved the voltage of the L gate with microwave (MW) frequency bursts in addition to DC bias pulses. To facilitate this functionality, the DC and MW signals were combined by a modified Anritsu V251 bias tee and connected to the corresponding voltage pin via Cu coaxial cable; the original tee included capacitors that were replaced with capacitors with a cryogenic performance of 100 nF.

While the DC line was connected from room-temperature electronics to the tee via regular Cu DC wiring, the MW signal was transmitted via a series of coaxial cables of different material. The high-frequency voltage steps for the pulsing scheme were produced by a Tektronix AWG70002A Arbitrary Waveform Generator (AWG), while the MW bursts were created by a Keysight N5183A Microwave Analog Signal Generator. The devices were clock-synchronized and had their outputs routed into a single coaxial cable by a room-temperature splitter of 3 dB attenuation. Between these room-temperature signal generators and the 1.5 K stage, the signal was transmitted via Cu/Be coaxial cable. At the 1.5 K stage, an Anritsu 20dB radio frequency (RF) inline attenuator was used to reduce signal intensity, and also to thermally anchor the line and prevent heat transfer into the continuing Nb coaxial cable below. At temperatures below 1 K, Nb has a reduced heat conductance while maintaining performance as an electrical conductor [49], making it an ideal material to connect the bias tee to the attenuator and thus to the signal generators above.

The magnetic field oriented normal to the plane of the DQD device was generated by a superconducting magnet installed in the bottom of the dilution refrigerator. Its placement was such that when the dilution unit was installed, the sample mount was located at the centre of its cylindrical

bore to optimize the direction and uniformity of the field applied to the DQD. Though the magnet was able to produce fields of up to 16 T at 4K, only field strengths between approximately 0.7 T and 1 T were employed in the experiments in this work due to the thermal energy produced by the MW generator, as well as its upper output frequency limit of 20 GHz.

Connected to the drain of the quantum point contact (QPC) was a Basel Precision Instruments SP983C current-voltage converter at room temperature in order to amplify the signal produced by the quantum point contact (QPC) charge sensor. This voltage was measured by connecting the converter to an Agilent 3458A Digital Multimeter with the number of power line cycles (NPLC) set to one, resulting in a measurement interval of 16 ms.

Quantum Point Contacts (QPCs)

The first quantum point contact (QPC) was discovered by van Wees et al. in 1988 [50] while experimenting on a two-dimensional electron gas (2DEG) on a GaAs/AlGaAs heterostructure; in the experiments in this work, a two-dimensional hole gas (2DHG) is employed to similar effect. When the width of a point contact in a semiconductor heterostructure at mK temperatures is on the order of the Fermi wavelength of a free hole, the conductance becomes quantized in multiples of the conductance quantum, $e^2/\hbar$. (In the case of the data shown in Figure 2 below, the fractional steps in units of the conductance quantum and curvature of the conductance are due to the non-ideal split-gate charge sensor, involving side reflections and localizations that introduce deviations from standard QPC behaviour.) Changes in the voltage applied to the gates defining the point contact adjust the width of the contact, as the field produced by the gates depletes the 2DHG beneath.

QPCs are now often used in semiconductor quantum dot (QD) architectures in order to detect changes in quantum dot occupation, including on the device used in this work. In experiments involving charge detection, gate voltages are carefully tuned so that the conductance of the QPC is
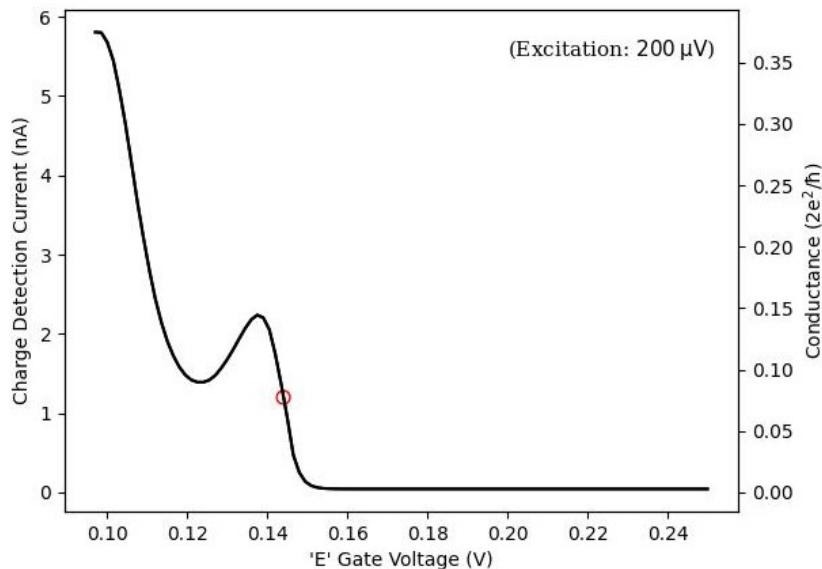
Figure 2: Charge detection current measured as a function of the voltage applied to the 'E' gate according to the labelling in <u>*Appendix A*</u>*. The red circle highlights the charge detection current at the chosen gate voltage, placed on the slope preceding the last step to maximize readout fidelity. The excitation (200 µV) is also shown.*

9

intermediate on the slope leading to the last quantized step, as shown in Figure 2. When the occupation of either quantum dot is changed, the resultant change in potential nearby creates a detectable change in the current across the QPC. The QPC current for any QD occupation can be determined by measuring a charge stability diagram, making QPC current a reliable probe for dot occupation [51].

Charge Stability Diagrams

Charge stability diagrams are experiments conducted on QD devices in order to determine and calibrate the charge occupation of the QDs as a function of the voltages applied to the gates defining the device. The occupation is denoted by (n_L, n_R), where n_L (n_R) is the number of holes on the left (right) QD. Two gate voltages are varied, thereby changing the chemical potential of the QDs, while measuring either the source-drain or QPC current to determine the boundaries of regions in the voltage parameter space for which the occupation of the QDs is constant, as well as "triple points" where three occupations coincide in energy. An example of a charge stability diagram is shown in Figure 6.

In ideal conditions, each gate would only affect the chemical potential of one QD at a time. However, QDs in practice are capacitively coupled to all gates defining the device at varying strengths. Thus, variations in voltage of any gate will alter the chemical potential of all QDs and can cause a change in dot occupation if a large enough change occurs in the potential at the QD.

Spin-Orbit Interaction

The spin-orbit interaction (SOI) occurs between the spin of an electron and its orbital angular momentum. In the reference frame of the electron, the moving electric field of the nucleus produces an effective magnetic field $\vec{B}_{SO}$ that interacts with the magnetic moment of the electron's spin $\vec{\mu}_s$, causing a torque on the spin's magnetic dipole moment and altering the energy of the electron by the amount ΔE_{SO}:

$$\Delta E_{SO} = -\vec{\mu}_s \cdot \vec{B}_{SO} \tag{1}$$

For electrons in GaAs, there are two mechanisms for the SOI: the Rashba and the Dresselhaus. Both effects arise from types of asymmetries in the crystal lattice and tend to have similar strengths [52], though on the device used in this work, the Dresselhaus effect was shown to dominate in the spin relaxation of holes [34].

The SOI is valuable for spin-based quantum computing in that it can be exploited to deliberately manipulate spin states. Following experimental reports [53] [54], Emmanuel Rashba proposed in 2005 [55] that an oscillating electric field can be used to control spin states in spintronics via electric dipole spin resonance (EDSR), explored in the "Electric Dipole Spin Resonance (EDSR)" section below. The SOI is stronger for holes than for electrons in GaAs [56], allowing spin manipulations to be performed on even shorter time scales in p-type devices.

Zeeman Splitting of Spin State Energy

Following Kramers' theorem [57], electron or hole spin states have degenerate energy levels when no external magnetic field is present. In 1896, before this theorem was proposed, Pieter

Zeeman discovered [58] that when an external magnetic field is applied, the two spin states become separated by the so-called Zeeman energy, described by the following relation:

$$\Delta E_Z = g^* \mu_B B \tag{2}$$

Here, μ_B is the Bohr magneton, B is the magnitude of the applied magnetic field, and g^* is the "effective g-factor", a proportionality constant that depends on the material composition and other parameters of the system. In this thesis, the spin-up (-down) state of a hole becomes the higher (lower) energy level when this splitting occurs.

In spin-based quantum computing, the tunability of the effective g-factor is an important functionality, as it allows qubits in an array to be addressed individually while in the same magnetic field. Past experiments using the same DQD device in this work have demonstrated the in-situ tunability of the hole g-factor via the following methods: by altering the angle at which the magnetic field is applied to the device [32] and by exploiting the spin-orbit interaction with a strongly-coupled auxiliary QD [41].

Spin Relaxation Time (T_1)

An important indicator of merit in quantum information processing on spin-based architectures is the spin lifetime, T_1. In the case that the degeneracy of the spin-states of an electron (or hole) is lifted, the lifetime of the higher-energy spin state will be limited, as it will relax to the ground state in time. For a system in which spin-down is the ground state, such as for the device in this work, the probability of a spin prepared in the higher-energy spin-up state remaining excited follows the exponentially decaying function:

$$P(\uparrow) = P_0 \exp\left[\frac{-t}{T_1}\right] \tag{3}$$

Here, P_0 is the probability of successful preparation to the spin-up state and t is the time elapsed since preparation.

Spin lifetimes across semiconductor devices vary greatly, with T_1 as long as 6 s in Si reported by Morello et al. in 2010 and 32 ms in Ge by Lawrie et al. in 2020 [59]. Interestingly, despite spin relaxation seemingly representing the destruction of spin information encoded in a higher-energy state, the phase relaxation time of a system, T_2, can be as long as $2 \times T_1$ or greater in some cases [60].

Electric Dipole Spin Resonance (EDSR)

Isidor Isaac Rabi proposed the mathematical framework of what would become nuclear magnetic resonance (NMR) in 1937 [61]. He and other researchers then demonstrated the ability to measure the magnetic moment of a beam of moving molecules experimentally in 1938 [62]. By applying a large magnetic field and a perpendicular magnetic field oscillating at high frequency, the researchers were able to rotate the molecules when the frequency of the oscillating field was at or near the Larmor precession frequency of the nuclear spins.

This behaviour can also be produced by an oscillating electric field. Of particular importance to the experiments in this work is the principle of electric dipole spin resonance (EDSR), proposed by Emmanuel Rashba in 1960 [63]. Via the SOI, the spin of an electron or hole becomes coupled to an external electric field, allowing oscillations in the field to induce changes in the electron momentum

that affect the spin state of the electron. In 2003, Rashba and Efros [64] showed that an electric field applied perpendicular to the plane of a quantum well could efficiently manipulate electron spins. Later, they determined that spins coupled more strongly to an in-plane electric field in a collaborative section of a paper published by Rashba [55] in 2005. On a semiconductor qubit apparatus, it is easier to induce a local electric field oscillating at MW frequencies than a magnetic one, making EDSR an attractive choice for the manipulation of spin states.

In 2006, Golovach et al. [65] theoretically explored the control of single electron spins on a quantum dot via EDSR. The Larmor frequency, f_{Larmor}, depends on the Zeeman energy level difference ΔE_Z between the spin-up and -down states:

$$\Delta E_Z = h f_{Larmor} \tag{4}$$

$$\therefore f_{Larmor} = \frac{g^* \mu_B B}{h} \tag{5}$$

The frequency at which the EDSR signal must be applied in order to rotate the spin of the electron is this Larmor precession frequency. Under the condition of an applied MW excitation, the rate at which the spin state cycles between the up and down states is known as the Rabi frequency, f_{Rabi}, and depends on the strength of the spin-orbit interaction in the material due to its role as the mechanism of the EDSR interaction. For quantum dots implemented in semiconductors such as GaAs and Si, the SOI of electrons is relatively weak, causing the time required to rotate a spin via the EDSR interaction to be on the order of the spin coherence time of the material. This means that in such devices, the information stored in other qubits in a larger array could decohere while performing spin manipulations on another.

Two approaches have been explored in order to remedy this severe limitation: a change of material and a change of carrier type, from electrons to holes. In the experiments leading to this work [34] [32] [41] [66], the latter method was employed, characterizing a lateral, gate-defined double quantum dot (DQD) device in GaAs/AlGaAs to isolate a single hole. In contrast with Si and Ge, holes in GaAs have a comparatively strong spin-orbit coupling, making the material a promising candidate for experimentation with EDSR. In 2019, Studenikin et al. [41] used this GaAs/AlGaAs DQD to detect the excitation of hole spins via EDSR. Zeeman-split energy levels of opposite spin in the neighbouring QDs were aligned such that the transport current from source to drain, I_{SD}, was activated when hole spins were successfully excited via EDSR. Furthermore, the effective g-factor was shown to be electrically tunable, varying with the voltage applied to a plunger gate near the left QD.

Alongside the desired effects of the increased SOI for holes were utilized successfully, additional challenges were also presented. Most importantly, common readout schemes based on the spin-blockade method become challenging in the presence of a strong SOI, as the reliance on the spin conservation of tunneling events is lifted by the introduction of spin-flip mechanisms due to the strong SOI [34]. As well, the Elzerman method, a common alternative, could not be used, as the charge detection time of the quantum point contact (QPC) was much greater than the T_1 spin lifetime of this device [42]. A latched spin-to-charge readout scheme was developed by Bogan et al. in 2019 [34] to remedy these issues. This method involves the transformation of one QD of the device into a memory register by tuning the gate voltages into the "latching regime". By translating the hole spin information into the charge occupation of the memory register, the lifetime of the spin information can long outlive T_1. The modified spin-to-charge readout scheme adapted from Bogan et al. is explored in detail in the [“Modified Spin-to-Charge Readout Technique”](#) section below.

Rabi Oscillation Experiments
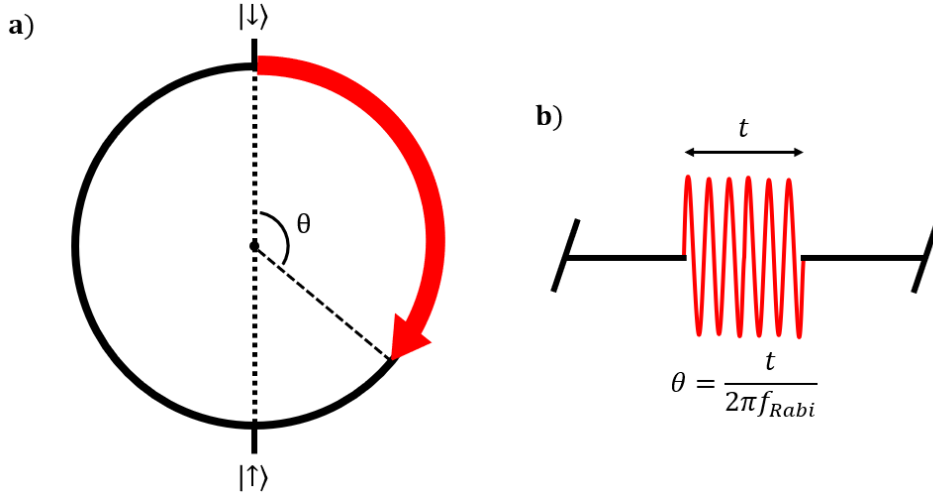
Figure 3: a) Bloch sphere representation of the action of a Rabi pulse on the hole spin state; b) Illustration of the varying gate voltage in a Rabi experiment.

As previously explained in the context of this thesis, when a hole spin is driven by an electric field oscillating at the Larmor frequency, its state rotates on the Bloch sphere between spin-up and -down at the Rabi frequency f_{Rabi} via the EDSR excitation. The plane in which this rotation occurs depends on the phase of the changing electric field. Importantly, the "in-phase" channel of the MW generator was used exclusively in the experiments contained in this thesis, meaning that all rotations are about the x-axis of the Bloch sphere. Figure 3.a) shows the rotation of the spin state on the Bloch sphere as a function of the burst duration, while Figure 3.b) shows the pulse applied to the L gate voltage. The rotation angle θ on the Bloch sphere in the rotating frame is shown as a function of the burst duration t, proportional to the Rabi frequency f_{Rabi}.

The probability of finding the spin in either state oscillates sinusoidally with a decaying envelope in its amplitude.

$$P(\uparrow) = P_0 \exp\left[\frac{-t}{T_{Rabi}}\right] \sin^2(\omega_{Rabi} t) \tag{6}$$

Here, P_0 is the maximal probability amplitude, $\omega_{Rabi} = 2\pi f_{Rabi}$ is the angular frequency of the probability oscillations, t is the duration of the oscillating electric field produced by the gate, and T_{Rabi} is the driven decay time of the probability oscillations. In many-electron devices, spatial inhomogeneity of the oscillating magnetic field used to induce electron spin resonance can cause decoherence, thus shortening T_{Rabi}. In the case of the experiments in this thesis, only a single hole spin is manipulated, eliminating this decoherence mechanism. Instead, the fluctuation of the nuclear spin bath, to which the spin is coupled via the hyperfine interaction, is the main source of Rabi oscillation decay [67].

By measuring Rabi oscillations at the Larmor frequency, the durations of the $\pi/2$- and π-pulses can be determined. For a spin in the ground state, these pulses result in a rotation from the ground state (spin-down) to the equator and excited state at the far pole of the Bloch sphere (spin-up), respectively. These pulse durations must be calibrated in order to perform composite pulse sequences such as the Ramsey, Hahn-echo, and CPMG pulsing schemes.

Ramsey Spin Evolution Experiments

a)

b)
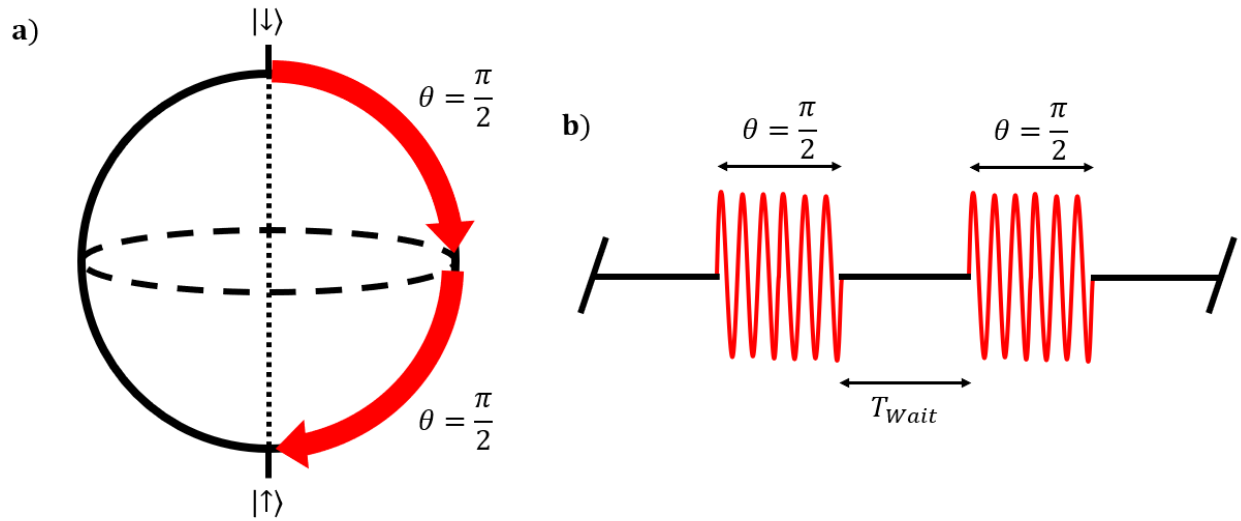
Figure 4: a) Bloch sphere representation of the action of a Ramsey sequence on the hole spin state; b) Illustration of the varying gate voltage in a Ramsey experiment. Pulse and wait durations are indicated.

Following the observation of Rabi oscillations in 1938, Norman F. Ramsey iterated on the procedure and developed a new pulsing scheme [68], seeking to reduce the introduction of noise into the resultant nuclear spins via inhomogeneities in the magnetic field applied to the beam of molecules. Rather than rotating the spins with an oscillating magnetic field throughout a single, continuous region, Ramsey proposed that the spins be rotated by oscillating magnetic fields for short periods at the beginning and end of the interaction region. Figure 4.a) depicts the spin state evolution on the Bloch sphere for a delay time of $T_{Wait} = 0$, equivalent to a Rabi burst of π duration. For increasing T_{Wait}, the hole spin is affected by its environment and thus spreads about the equator of the Bloch sphere, decreasing the coherence of the spin state after the second $\pi/2$-pulse is applied. The pulse sequence is shown in Figure 4.b) with the pulse durations and wait time labelled. Each of these would induce a $\pi/2$ rotation of the spin state on the Bloch sphere, while in between these regions, the spins would be allowed to freely precess about the z-axis at the Larmor frequency.

If the spin manipulation pulses were applied precisely at the Larmor frequency, the total action of the scheme for any wait time would be a π-rotation on the Bloch sphere sans the effect of any dephasing processes. Importantly, the dephasing effects of any inhomogeneities in the oscillating magnetic field regions would be small in comparison with the equivalent effects in the Rabi method. Furthermore, any detuning from the Larmor frequency in the magnetic field oscillations would be precisely detectable, as the resultant spin states would oscillate as a function of the delay time between the $\pi/2$-pulses with a frequency equal to the detuning.

Ramsey pulsing experiments are commonly performed in order to characterize the free precession coherence time of spin qubits, known as T_2^* [69]. In this work, the $\pi/2$-pulses were applied via MW bursts of the voltage applied to the plunger gate labelled "L" in Figure 1.a). As with the Rabi method, the probability of finding the hole in the spin-up state following a Ramsey pulse sequence is bounded by an exponentially decaying envelope.

$$P(\uparrow) = P_0 \left(1 - 0.5 \exp\left[\frac{-t}{T_2^*}\right]\right)\cos^2\left(\frac{t\Delta\omega}{2}\right) \tag{7}$$

Here, P_0 is the maximum probability amplitude, t is the delay time between the $\pi/2$-pulses, $\Delta\omega$ is the difference in frequency between the applied MW oscillations and the Larmor frequency, and T_2^* is the effective spin coherence time. For delay times of sufficient duration, the proportion of spin-up measurements is intermediate, as only the action of the final $\pi/2$-pulses affects the spin state before readout occurs.

This spin coherence time represents the time scale over which the phase differences between components of a quantum state are lost. As many quantum algorithms depend on phase differences in their operation, this represents a loss of information and limits the maximum duration of these algorithms. However, the lifetime of this information can be extended by using alternative sequences based around the concept of refocusing pulses that reverse dephasing processes, such as in the Hahn-echo and CPMG schemes.

Hahn-echo, CPMG
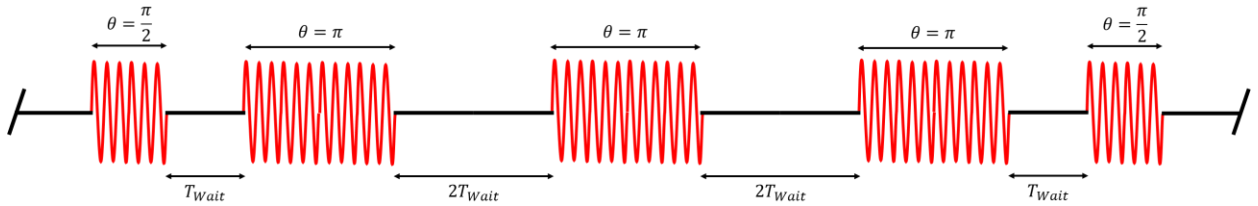
Figure 5: Illustration of the varying gate voltage in a CPMG experiment for $N_{CPMG} = 3$.

Spin echoes were first detected by Erwin Hahn in 1950 [70] after applying two $\pi/2$-pulses in quick succession and seeing an echo of the signal in the molecule spins after a delay. Carr and Purcell later recommended increasing the duration of the second pulse to a π-rotation [71]. The full Carr-Purcell-Meiboom-Gill (CPMG) pulse sequence instead involves the introduction of N_{CPMG} refocusing π-pulses between the two $\pi/2$-pulses of a Ramsey sequence in order to prolong the coherence of the spin. The Hahn-echo pulse sequence is analogous to a CPMG sequence where $N_{CPMG} = 1$.

When the microwave bursts in these sequences have frequency equal to the Larmor frequency of the hole spin states, the refocusing pulses perform a half-rotation in the rotating frame of the spin about the x-axis on the Bloch sphere, thereby reversing the direction of spin dephasing processes. For a π-pulse applied a duration T_{Wait} after the initial $\pi/2$-pulse, the "echo" of the spin state will occur after an additional delay of T_{Wait}. In pulse sequences where $N_{CPMG} > 1$, the delays between subsequent π-pulses are set to $2T_{Wait}$, thereby reproducing inverted spin dispersions at the beginning subsequent refocusing pulses. This structure is shown in the sample CPMG sequence in Figure 5. Given that spin state detection is performed via a spin-to-charge readout scheme in this thesis, a final $\pi/2$-pulse is then applied to rotate the state to a pole of the Bloch sphere. The readout mechanism can then successfully translate the spin state to a charge occupation state in the memory register.

As with the Ramsey and Rabi sequences, the probability of finding the spin in the higher-energy spin-up state is bounded by an exponentially-decaying function of the total waiting time in the sequence. The total rotation applied by a CPMG pulse sequence is dependent upon N_{CPMG}; for

even (odd) N_{CPMG}, the state will have been rotated by an odd- (even-) numbered multiple of π. This means that for pulses applied at the Larmor frequency with odd N_{CPMG}, the probability of finding the hole in the spin-up state is:

$$P(\uparrow) = P_0 \exp\left(\frac{-t}{T_2^{CPMG}}\right) \tag{8}$$

whereas for even N_{CPMG}:

$$P(\uparrow) = P_0 \left(1 - \exp\left[\frac{-t}{T_2^{CPMG}}\right]\right) \tag{9}$$

Despite this difference in decay type, the coherence time T_2^{CPMG} can be extracted in either case by fitting the data with the function corresponding to the number of refocusing pulses.

Qubit Quality Factor (QQF) and Gate Quality Factor (GQF)

In related works [69], the qubit quality factor (QQF) is used as a measure of the aptitude of a device with regard to quantum computing operations. It is most often defined by the following equation [69]:

$$QQF = f_{Rabi}T_2^* \tag{10}$$

As a product of the Rabi frequency f_{Rabi} and the spin coherence time T_2^*, the QQF is a unitless number that estimates the number of gate operations that can be performed on a qubit before spin information stored in other qubits in the same system will decohere. Spin qubit researchers seek to maximize both f_{Rabi} and T_2^* to achieve the maximal QQF of a given device as a measure of its aptitude for the implementation of quantum computing circuitry.

Some works also reference a gate quality factor (GQF):

$$GQF = f_{Rabi}T_{Rabi} \tag{11}$$

This quantity is useful as a measure of the fidelity of gate operations conducted via Rabi rotations. In many cases, the Rabi decay time T_{Rabi} is significantly longer than the effective spin coherence time T_2^*, in which case the GQF is larger than the QQF [67] [69].

The Latching Regime of the Right QD
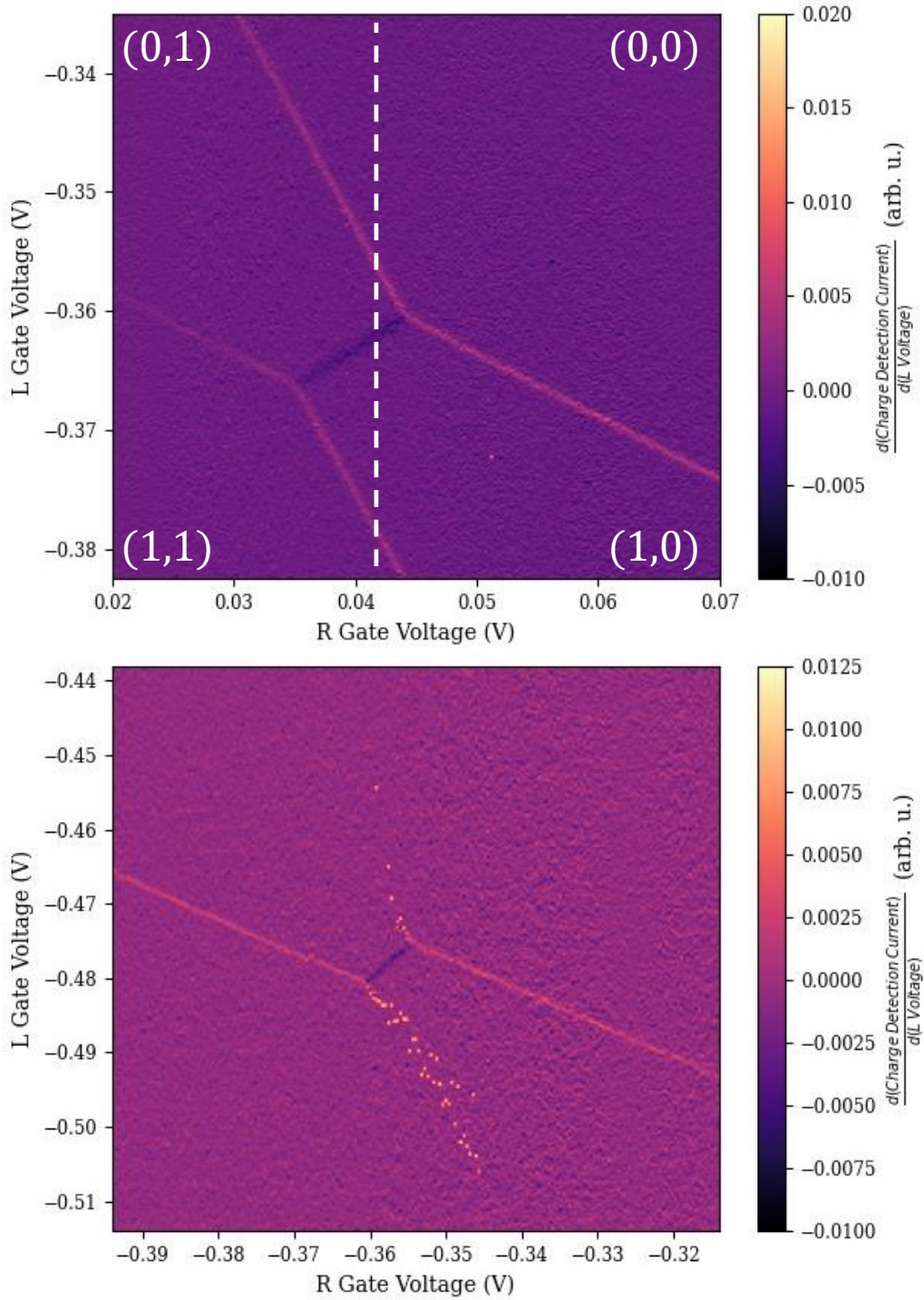
Figure 6: a) Example of a charge stability diagram measured on the DQD device with (left, right) QD occupation labelled in each region. In order to make the charge occupations regions easily distinguishable, a derivative in charge detection current is taken along the vertical axis (i.e., the voltage of the gate labelled "L" in [Figure 1.a)](#); b) Charge stability diagram measured in the latching regime. This SD shows strong latching, as the charge addition line of the right QD is replaced by sharp changes in charge detection current.

Experiments in this work were conducted in the single-hole regime. Each charge stability diagram (SD) in this regime is measured using charge detection current across the QPC near the right QD in order to make clear the boundaries between charge occupation regions even distant from regions where hole transfer occurs. Due to the layout of the device causing non-ideal capacitive coupling, the conductance across the QPC was affected by each of the other gates in the system. This caused large fluctuations in charge detection current within each occupation region and areas of similar charge detection current for different dot occupations; these characteristics are visible in Figure 10.a), in which no derivative is taken along the y-axis and the charge detection current reading itself is shown. For this reason, each charge stability diagram (SD) in this work is displayed after a derivative is taken along the vertical axis. This operation increases the visual clarity of the diagram by increasing the uniformity within each charge detection region.

The SD in Figure 6.a) was measured in the "non-latching regime", in which hole transport into and between the QDs occurs on a much shorter time scale than charge detection measurement. This measurement occurs once per clock pulse of the AWG, separated by intervals of 16 ms. Each region of the diagram has a corresponding label (n_L, n_R), where n_L (n_R) represents the number of holes on the left (right) QD. The x- and y-axes are the voltages applied to the R and L plunger gates, respectively. Charge occupation regions are separated by lines of charge addition (bright) and transfer (dark). The aforementioned capacitive coupling can also be demonstrated by visual inspection of Figure 6.a). Notice that along the dashed vertical line, only the voltage of the L plunger gate, nearer to the left QD, is altered between successive data points, yet the occupation of both QDs is affected: moving up from the bottom of the line, the ground state hole occupation of the DQD undergoes the following changes in sequence: $(1, 1) \rightarrow (1,0) \rightarrow (0,1) \rightarrow (0,0)$.

Due to the strong SOI of holes in GaAs, the Pauli spin blockade readout mechanism is made inapt for experiments on single-hole devices such as the one experimented upon in this thesis. The commonly employed alternative single-shot readout mechanism designed by Elzerman et al. [42] requires that the charge detection time be shorter than the spin relaxation time T_1. In this work, the charge detection hardware was limited to the aforementioned clock time of $\approx$ 16 ms. At the magnetic field strengths used, this measurement time was much longer than the T_1 relaxation time, which was on the order of 1 μs. These constraints necessitated the development of a readout scheme by Bogan et al. [34] that stores the spin information in a long-lived charge occupation state of an auxiliary quantum dot until charge detection readout. The modified version of this spin-to-charge readout technique used in this work is detailed in the "Modified Spin-to-Charge Readout Technique" section below.

In order to utilize this readout method, one QD on the device must be tuned into the latching regime to form a memory register. In this work, this was chosen to be the right QD, since the proximity of the QPC to the right QD, as shown in Figure 1.a), increased the resolution differences of charge occupation in the right QD in comparison to the left. The space of gate voltage configurations in which is the case is known as the "latching regime", as the hole becomes "latched" in the right QD until after charge sensing measurement occurs.

Latching was detected by measuring a SD and inspecting the charge addition line associated with the right QD. The points in the SDs in Figures 6.a) and b) were measured from the bottom to top of each column beginning with the left-most column. This meant that while subsequent points along the horizontal axis were measured at a significantly longer delay dependent on the resolution of the diagram, the temporal separation between subsequent points along the vertical axis was equal to the

charge detection time (≈ 16 ms). This order of measurement motivated the decision to take derivatives along the vertical axis in each SD, as evidence of latching would arise when observing the change in charge detection current between subsequent single-shot measurements.

Measurements taken across a charge addition (transfer) line showed a local increase (decrease) in the slope of the charge detection current over a series of points. When measuring across a charge addition line for the right QD in the latching regime, however, changes in hole occupation occur on a time scale slower than the charge detection time. This results in a sharp change between subsequent single-shot measurements from the current associated with one occupation state to another, creating a sharp change in charge detection current, seen in Figure 6.b) as bright spots after a vertical derivative is taken.

Figure 7: a) Full spin-to-charge readout scheme. Step durations are labelled where they do not vary between experiments and are not to scale; b) Illustration of a charge stability diagram with hole occupation regions labelled. Each of the four pulsing locations are labelled where they would appear if applied in the transport regime; c) Series of energy level diagrams that show changes in QD occupation and hole spin state. Diagrams in the same columns denote two different possible situations depending on hole spin state after spin manipulations are performed. Continuity between successive single-shot cycles is indicated with solid or outlined arrows at either end of each row.

Marton et al., used under CC-BY 4.0 / Adapted from original.

Readout

The Modified Spin-to-Charge Readout Technique

Central to the experiments performed in this work is the spin-to-charge readout method, a modification of the method proposed by Bogan et al. in 2019 [34]. This pulsing scheme, including a fourth pulsing level and additional steps, leads to the conversion of the spin state of a hole in the left QD of the system into the charge occupation of the right QD. Due to the latching of the right QD, the charge occupation is determined via the QPC current measured at the end of each measurement cycle.

Figure 7.a) depicts the pulsing sequence performed in each single-shot cycle. The gate voltage corresponding to each step is measured in mV relative to the driving ("D") position. The durations of each step may not be to scale and are thus labelled for clarity. All durations are constant save for the duration of the driving step, T_D, which is varied in some experiments.

An outline of a charge stability diagram is shown in Figure 7.b) to highlight the boundaries of the charge occupation regions relevant to this work. The four pulsing locations are labelled, with axis marks measured in mV relative to the driving ("D") position in the L and R gates.

Figure 7.c) is a series of energy level diagrams that correspond to the energy level alignments of the two dots and Fermi level in the left lead for each step of the cycle. The vertical lines separating the left lead, left QD, and right QD have varying thicknesses to represent the relative tunneling times ($T_L < T_{Inter} \ll T_R$). Each column of Figure 7.c) is labelled according to the step number as shown in Figure 7.a). In the first two columns, the top row of diagrams represents the hole spin state in the case that the previous single-shot cycle ended with a hole latched in the right QD, while the bottom row represents the dynamics in the case that the previous cycle ended with the right QD empty. Similarly, the top row of the last two columns represents the mechanism by which a hole is latched in the right QD at the end of the readout sequence, while the bottom row represents the mechanism by which the right QD is left empty. The continuity between the two possible occupations at the end and beginning of subsequent cycles is indicated by the arrows at the left and right sides of the figure.

In the following step-by-step explanation of the readout technique, some steps are grouped together in order to indicate the continuity of subsequent single-shot experiments according to the hole occupation state of the latched QD after measurement occurs. For these grouped steps, the upper and lower rows of energy level diagrams are explained separately in an indented subsection.

Steps 1 and 2

The cycle begins with the energy levels of both dots above the Fermi level of the left lead, with the spin-down state of the left QD above the spin-up state of the right QD.

Upper Row

A hole is latched in the spin-down state of the right QD. Despite the measurement ("M") position being located in the (0, 0) region, the hole cannot tunnel out to the right lead during the cycle due to the extended tunneling time of the latching regime, nor can it tunnel out to the left lead via the left QD due to the misalignment of the energy levels.

In step 2, however, the system is moved to the initialization ("I") position and held at the configuration for 10 µs, much longer than the inter-dot tunneling time, to allow the hole to transfer to the now-lower energy states of the left QD. The "I" position is in the (1, 0) region, meaning that the relaxation of the system will favour this mechanism over the tunneling of a new hole into the left QD from the left lead even though the empty energy levels of the left QD are below the Fermi level.

Lower Row

Both QDs are empty in step 1 following the conclusion of the previous cycle. Following the transition to the "I" position in step 2, a hole tunnels into the left QD from the left lead, appropriately populating the dot according to the ground state charge occupation.

Step 3

The system is returned to the "M" position and is held there for 10 µs, much longer than the tunneling time between the left QD and left lead. This leads to the hole exiting the left QD to the left lead according to the (0, 0) occupation at the ground state in this configuration. Following the conclusion of this step, both QDs have no holes loaded regardless of the occupation of the right QD following the end of the previous single-shot cycle.

Step 4

The system is once again moved to the "I" position in the (1, 0). During this step, a hole tunnels in to the left QD from the left lead and relaxes into the lower-energy spin-down state. This duration of this step is set to 10 µs, much longer than the T_1 relaxation time, in order to ensure that the hole is in the spin-down state before spin manipulations occur. Any remaining spin-up probability is random and thus does not result in feedback on the next cycle.

Step 5

Deviating from the original readout scheme [34], the system is now moved to the driving ("D") position, also located in the (1, 0) region but further from the (0, 0)–(1, 0) charge addition line to reduce the possibility of crossing between charge occupation regions during pulsing experiments. At this position, the spin state of the hole in the left QD is manipulated via MW bursts applied to the L gate voltage to induce spin state oscillations via EDSR. Regardless of the duration of the pulsing sequence, the final pulse concludes a set duration ($T_{OFF} = 50$ ns) before moving to the next step.

Steps 6 and 7

Following the conclusion of spin manipulation, the system is moved the transfer ("T") position in step 6, located in the (0, 1) occupation region. Importantly, the higher-energy spin-up

state of the left QD is aligned with the lower-energy spin-down state of the right QD. This alignment makes it such that the hole in the left QD can only be transferred to the right QD if it is in the spin-up state, since any other tunneling mechanism would be non-energy-conserving.

Upper Row

The hole in the left QD is in the spin-up state following the spin manipulations of the previous step. Now at the "T" position, the hole is probabilistically transferred to the spin-down state of the right QD; the energy level diagrams depict a successful transfer. After returning to the "M" position in step 7, the hole is now "latched" in the right QD. Its presence can be detected via charge sensing with the nearby QPC.

Lower Row

The hole in the left QD is in the spin-down state following the spin manipulations in the previous step. At the "T" position, the hole is unable to transfer to the right QD due to the alignment of the energy levels, and thus remains in the left QD. When the system is returned to the "M" position, the hole tunnels out to the left lead, leaving both QDs empty to be detected by charge sensing.

The structure of this readout mechanism is such that the hole occupation is correctly prepared before spin manipulation regardless of the outcome of the previous single shot experiment. This method is apt for implementation when the charge detection time is much slower than T_1 and has already seen use in other research groups [72].

Tunneling Time Tuning

In the latching configuration, the tunneling time T_R between the right QD and right lead is much longer than the measurement time by definition. Additional conditions are placed on the two other tunneling times of the DQD device by the Bogan spin-to-charge readout scheme: the inter-dot tunneling time T_C had to be of intermediate duration ($\approx$ 200 ns), while the tunneling time T_L between the left QD and left lead had to be very short ($<$ 10 ns) to allow the occupation in the left QD to be quickly controlled throughout the pulse sequence. Altering the voltages applied to the plunger gates defining the two QDs could control these tunneling times but would simultaneously affect the locations of the charge occupation regions needed in the readout method.

Once the system was tuned to the (0,0) charge occupation region in the latching regime, the voltages of the six QD gates (not including the QPC gate)0 were modified to produce these tunneling times. Due to the non-negligible capacitive coupling of both QDs to each of these gates, a significant change in the voltage of any of the gates could cause a change in the ground state hole occupation of either QD. This affected the location of each charge occupation region in L-R gate voltage space, requiring SD remeasurement after any change in the voltage configuration in order to know the location of the boundary of the (0,0) region and the triple points in gate voltage space. This is displayed in Appendix A.
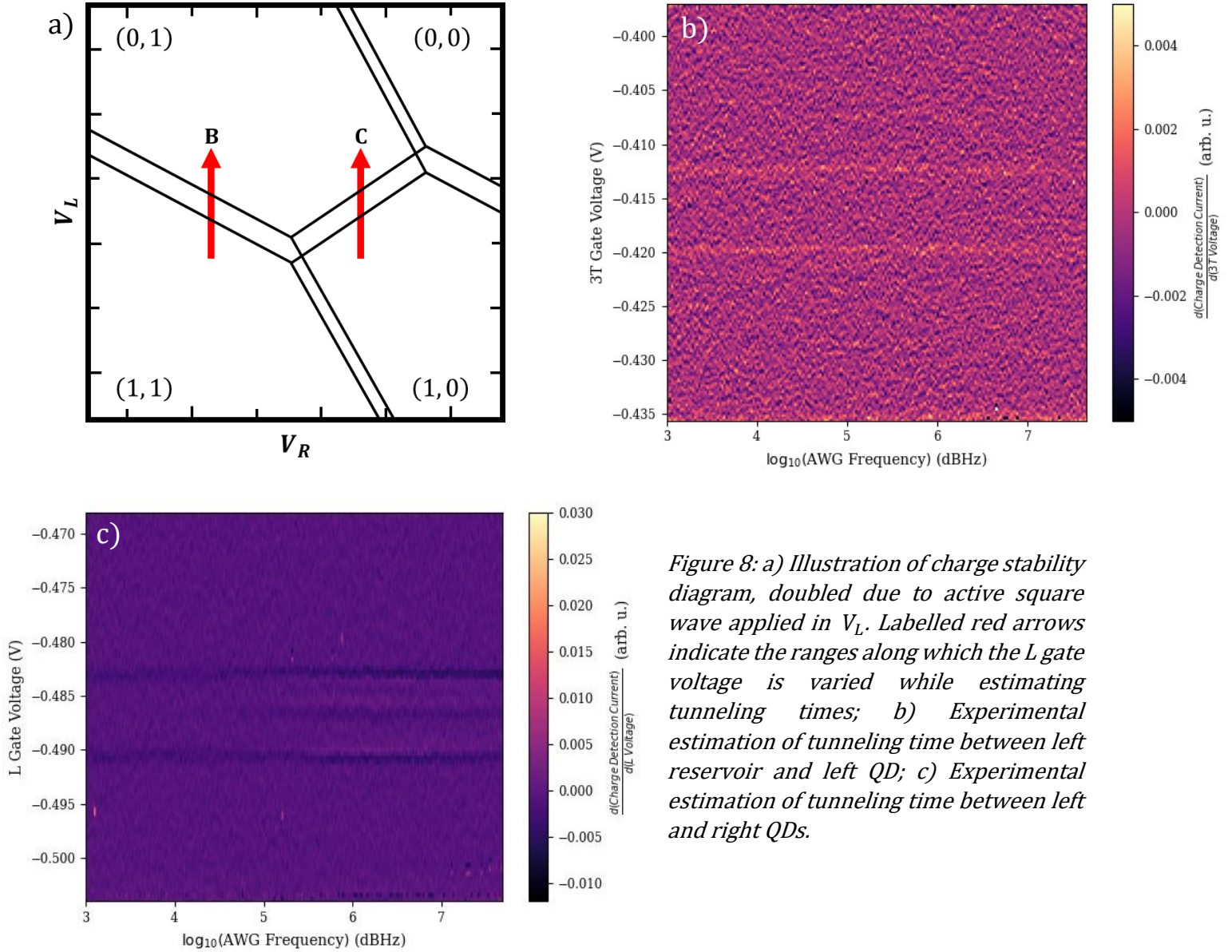
Figure 8: a) Illustration of charge stability diagram, doubled due to active square wave applied in V_L. Labelled red arrows indicate the ranges along which the L gate voltage is varied while estimating tunneling times; b) Experimental estimation of tunneling time between left reservoir and left QD; c) Experimental estimation of tunneling time between left and right QDs.

By measuring SDs after a change in the voltage of each gate individually, it was found that the SD would shift linearly in L-R voltage space along a different vector for each gate (see Appendix A). Applying these vectors to the voltages meant that experiments could retain the same position relative to the boundaries of the charge occupation regions after an arbitrary change in any gate voltage. This allowed the isolation of the change in tunneling time produced by altering the voltage of a given gate.

Figure 8 shows the results of an experimental method to estimate the tunneling times T_L and T_C when tuned as per the constraints of the readout method. A constant square wave of varying frequency is applied in the L gate voltage throughout all measurements in each diagram. Charge detection measurements were performed by varying the L gate voltage across the charge addition line associated with the left QD for Figure 8.b) and across the charge transfer line between the two

QDs in Figure 8.c). After each sweep, the frequency of the voltage oscillation is increased in logarithmic steps, as shown along the x-axis.

In Figure 8.c), the charge transfer line (dark) can be seen in double due to the application of the square pulse. The separation of ≈ 7 mV is due to the difference in voltage between the steps of the square wave. When a sufficiently high frequency is reached in the voltage oscillation, inter-dot tunneling is allowed to occur at the average of the two voltage steps of the square wave, introducing a third dark line between the two steps. This indicates that for non-resonant tunneling, $\Gamma_C = 1/T_C$ is approximately 100 ns, appropriately tuned between T_L and T_R. In Figure 8.b), no additional line appears, signifying that the tunneling rate $\Gamma_L = 1/T_L$ is greater than the largest frequency applied of the square wave. This equates to a tunneling time $T_L < 10^{-7.5}$ s ≈ 32 ns, sufficiently short for the application of the readout method.
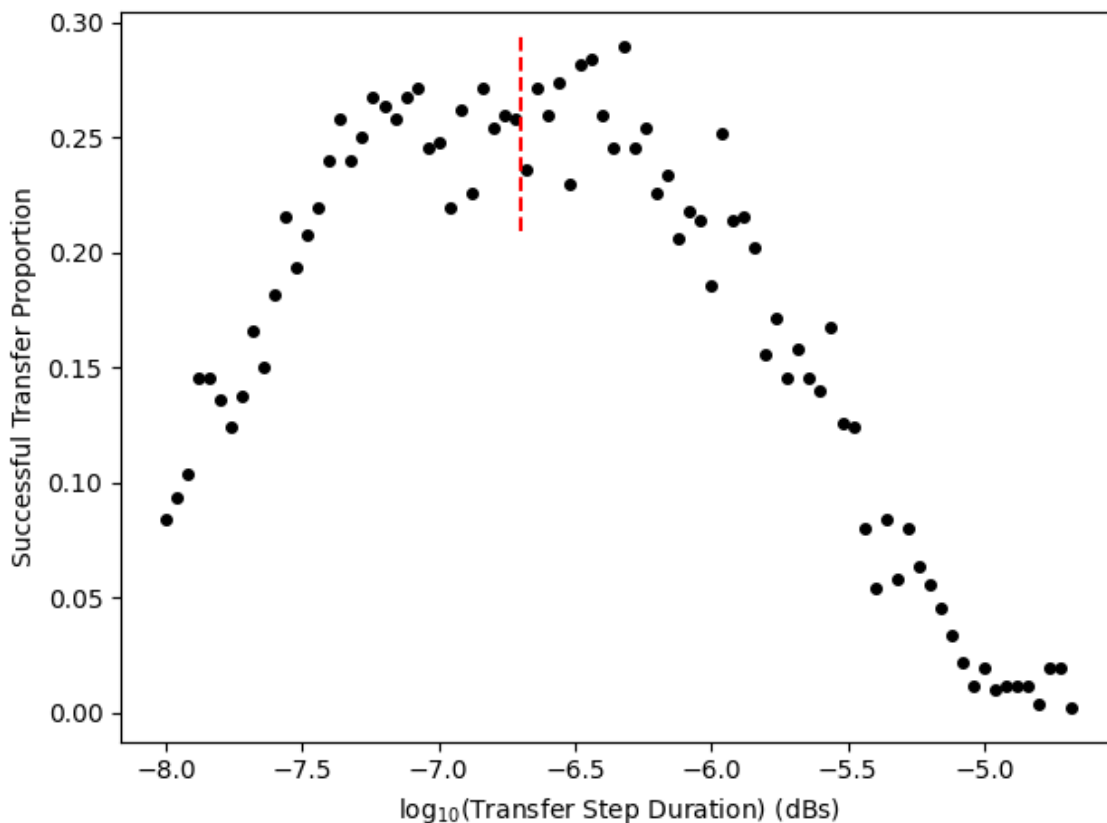
Figure 9: Measurement of spin-up readout rate as a function of the transfer step duration. The dashed vertical line indicates the duration chosen for subsequent experiments (200 ns).

Figure 9 shows the results of an experiment conducted to determine the optimal duration of the transfer step in the readout method. This transfer time is much shorter than T_C, as in the gate voltage configuration used in this experiment, one pair of energy levels between the two QDs are resonant, making the rate of hole transfer. The probability for successful hole transfer is peaked when the duration of the step, T_T, in between the approximate bounds of $10^{-7.25}$ and $10^{-6.25}$ s. For the experiments in this work, the duration of the pulsing step was set to 200 ns, highlighted with a dotted red line, to ensure the maximal probability of successful transfer.

Detection of Energy Level Alignment
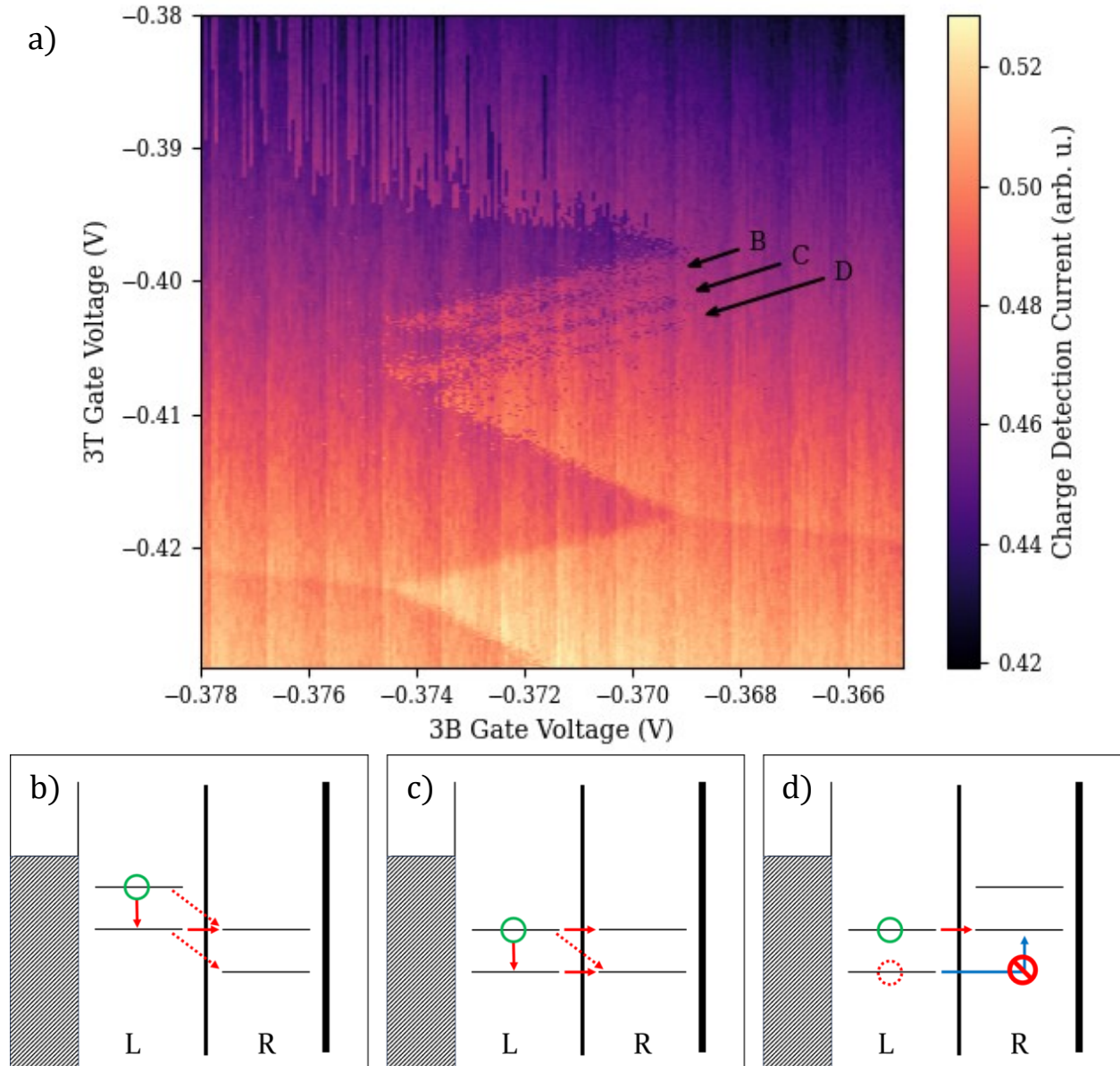
Figure 10: a) Charge stability diagram measured while three-level pulse from Bogan et al. [34] is active. The parallel lines of low charge detection current corresponding to the energy level alignments in Figures b)-d) are indicated; b)-d) Energy level diagrams depicting the allowed and disallowed hole transfer mechanisms from the left QD to the right according to the aligned energy levels.

With latching of the right QD achieved and the remaining two tunneling times tuned as required, preliminary testing involving the readout sequence could begin in order to appropriately place the pulsing locations in L-R voltage space. Figure 10.a) shows a SD measured at $B = 1.0$ T while the three-level pulse used by Bogan et al. [34] was active.

The position of each point in L-R voltage space reflects the gate voltage configuration at the "M" pulsing position. In each single-shot cycle, the system is held at the "I" position for 500 ns, much shorter than the T_1 relaxation time, to increase the likelihood that the hole is in the higher-energy spin-up state before moving to the transfer step. This allows this type of SD to be used to detect all three possible resonances in the QD energy levels at the transfer step.

Above the standard structure of the occupation regions, an irregular region of hole occupation can be seen. These are artifacts produced by applying the readout sequence at improperly chosen voltage alignments and can be ignored, since these gate voltage configurations are not employed during the readout scheme. Three dark lines parallel to the charge transfer line are visible, labelled according to the three energy label diagrams in Figures 10.b) – d). These lines appear when the "M" position is placed such that the energy levels of the two QDs allow for hole transfer between them during the transfer step. The on-resonant tunneling time is on the time scale of the duration of the transfer step, while the off-resonant tunneling time is much longer. The alignment corresponding to the line of lowest L gate voltage (Figure 10.d)) of the three involves the spin-selective transfer necessary for the readout method; thus, all pulsing experiments in this work are initialized such that the "M" position is located along this line.

The varying distance between the three lines in L gate voltage is dependent upon the applied magnetic field via the Zeeman effect. For an applied field $B = 2.0$ T, only one line of the three can be seen, disallowing the verification of the energy level alignment using this method. For magnetic fields strengths lower than 0.6 T, the lines instead become too close in voltage to resolve, affecting the accuracy of spin-to-charge conversion. Thus, magnetic fields in the range $0.7 - 1.0$ T were employed in the remainder of the experiments discussed in this thesis.

The situations depicted in Figures 10.b) – d) represent the energy level alignments that occur at each of the three lines, in order from the highest in L gate voltage to the lowest. In the Figures 10.b) and c), spin-conserving and non-conserving tunneling events are possible due to the strong SOI of holes and does not provide spin information when a transfer occurs. However, in the alignment associated with the "third line" shown in 9.d), only a hole in the higher-energy spin-up state can transfer to the right QD, as any spin non-conserving mechanism is disallowed. This condition guarantees that if the readout mechanism concludes with the detection of a hole in the right QD, the hole in the left QD must have necessarily been in the excited state of the left QD.

Once the exact voltage position of the third line was verified, it was also possible to identify the ranges of charge detection current for each of the two possible occupation states of the right QD. Given the probabilistic nature of the hole transfer in the readout method, only some of the single-shot experiments measured at the third line would lead to (0,1) charge detection measurement. Thus, a substantial portion of all measurements taken at the third line would correspond to the (0,0) charge occupation state irrespective of the spin state of the hole. The two different occupations of the right QD resulted in two different charge detection current ranges for which the signal-to-noise ratio was high enough to distinguish. By thus grouping the results, the proportion of single-shot measurements with charge detection current corresponding to the (0,1) occupation region would signify the proportion of successful excitations that were transferred to the right QD during the readout process.

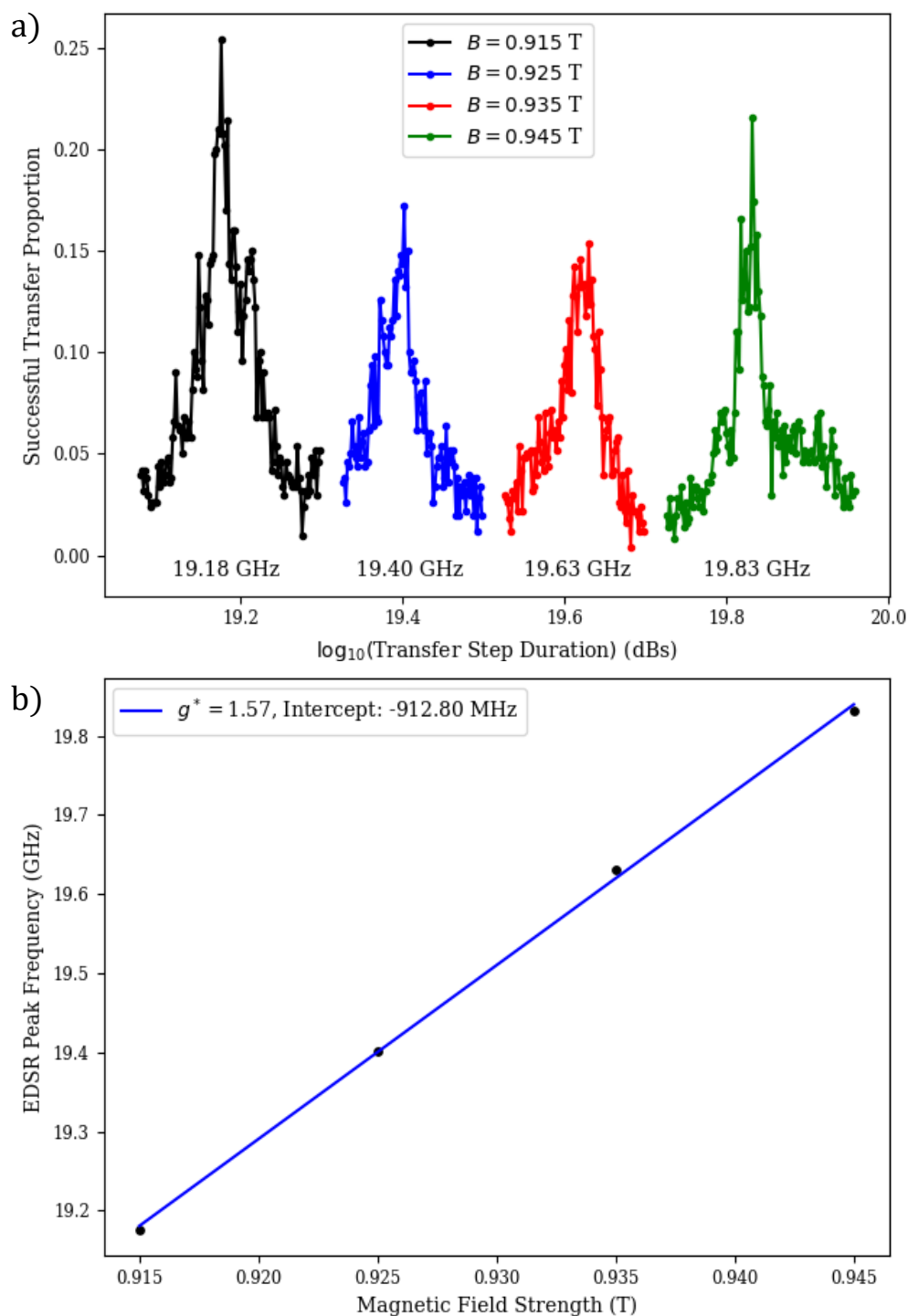Figure 11: a) EDSR signals identified as peaks in successful transfer proportion, each labelled with the approximate central frequency. The y-value of each point is the proportion of 500 single-shot cycles that resulted in a low-current measurement. The magnetic field strength was varied linearly between adjacent experiments; b) Extraction of dot effective g-factor by linearly fitting the EDSR frequency at each field strength.

Results and Discussion

For a discussion of the procedure and experimental details, please see [Appendix B](#).

Identification of EDSR, First Rabi Oscillations, and Chevrons

With the pulsing locations aptly placed, experiments involving the spin-to-charge readout scheme could begin. However, given the novelty of the employment of the latching regime in spin manipulation experiments on this device, the precise g-factor of the DQD system in its new configuration was unknown. This necessitated an initial search for an EDSR response in MW burst frequency–magnetic field parameter space.

While located at the driving position in each single-shot cycle, the voltage in the L plunger gate was modulated by the MW modulation of the gate voltage over a large range of frequencies in the $18 - 20$ GHz range. A significant increase in the proportion of lower charge sensing current measurements, signifying successful hole transfers to the right QD, would indicate a potential EDSR excitation was occurring at the MW burst frequency. The duration of the burst was set to 7 µs to increase the likelihood of detecting EDSR excitation. Given that the Rabi oscillation frequency was not known, it was possible that too short a pulse may have produced a rotation of an integer multiple of 2π, thus not producing a peak in the spin-up proportion. Instead, a longer burst produced an intermediate proportion of spin-up detections with a sufficient signal-to-noise ratio to be detected. Due to a lack of averaged results across repeated EDSR experiments, it was not possible to discern whether the shape of the EDSR peaks were Gaussian or Lorentzian; a simple extension of this work would be to investigate these characteristics by performing more experiments with greater resolution near the Larmor frequency, with varying Rabi pulse durations.

In order to verify that the peak in spin-down probability was due to EDSR excitation, the experiment was repeated for four evenly-spaced magnetic field values. Figure 11.a) depicts the EDSR peaks for four experiments performed in sequence between which the magnetic field is increased by 0.01 T. The central frequency of each of these peaks, for which a corresponding estimate is given underneath, changes approximately linearly with magnetic field strength, agreeing with the form of the Hamiltonian for the EDSR interaction and confirming that the signal seen was caused by EDSR. The g-factor for this voltage configuration was determined by inserting the central frequency for each peak, ω_{IQ}, and the corresponding magnetic field into the following equation:

$$hf_{Burst} = g^*\mu_B B \tag{12}$$

$$\therefore f_{Burst} = \frac{g^*\mu_B}{h}B \tag{13}$$

Experimental results, however, are better modelled if the function includes a constant offset. By producing a linear fit of the peak frequencies with respect to the applied magnetic field in Figure 11.b), the effective g-factor was found to be $g^* = 1.57$ for this configuration. However, the y-intercept of this fit is non-zero, disagreeing with the theoretical equation and suggesting that a non-linear change in g^* exists for small values of B. Another method revealed the same inconsistency with theory; Figure 12.a) shows the results of two successive experiments in which the duration of a MW burst was held constant at 2 µs while varying the applied magnetic field and MW burst frequency.

Once again, the slope of this graph is $g^*\mu_B/h$. By extracting a linear fit function for the points with an EDSR response, an effective g-factor of $g^* = 1.57$ is extracted with a y-intercept of -0.83 GHz. If the intercept of the fitting function is affixed to the origin, g^* decreases to 1.50 and the R^2 fitting parameter is decreased slightly. Both of these fit functions are displayed together with the extracted

data points in Figure 12.b). The standard deviation of the data in Figure 12.b) is ~23 MHz, less than 3% of the deviation of the line of best fit from the origin. This suggests that unexplained phenomena may occur for small magnetic field strengths. Given the aforementioned constraints in the isolation

a)
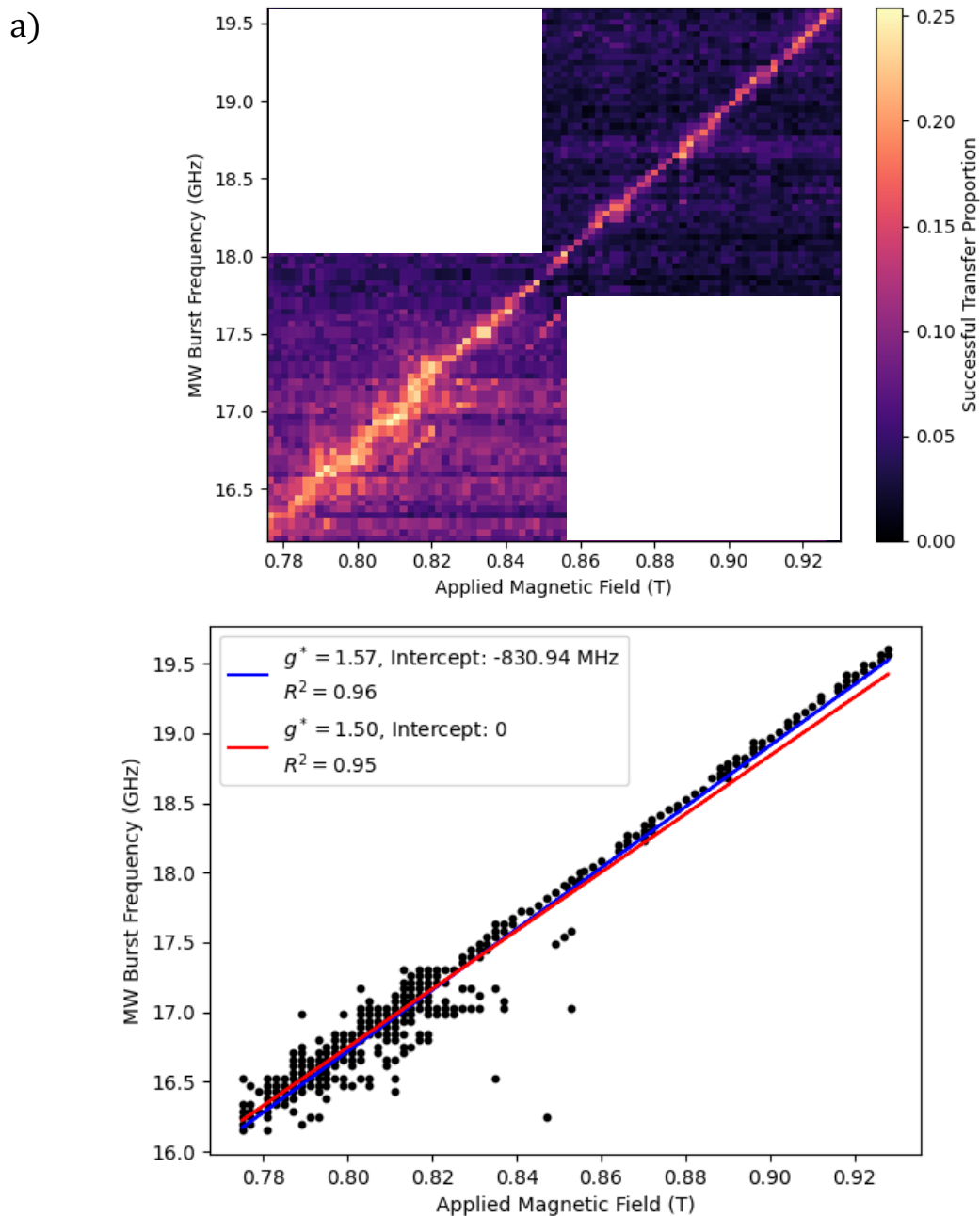
Figure 12: a) EDSR signal measured while varying MW burst frequency and magnetic field strength. Two experiments conducted consecutively are overlaid to highlight the continuity of the linear dependence of the EDSR peak frequency on B. Each point is the proportion of 500 single-shot cycles that resulted in a low-current measurement; b) Extraction of dot effective g-factor by linearly fitting the resultant data. All points for which the successful transfer proportion was above half of the maximum value were included. Fit lines for variable and fixed intercepts are shown in blue and red, respectively.

of the "third line," sufficiently small magnetic field strengths could not be employed in order to extend these experiments and observe the changes in effective g-factor near the origin. A potential extension of these experiments would be to develop methods to apply this readout mechanism at smaller magnetic field strengths and measure the EDSR peak frequency in such domains.
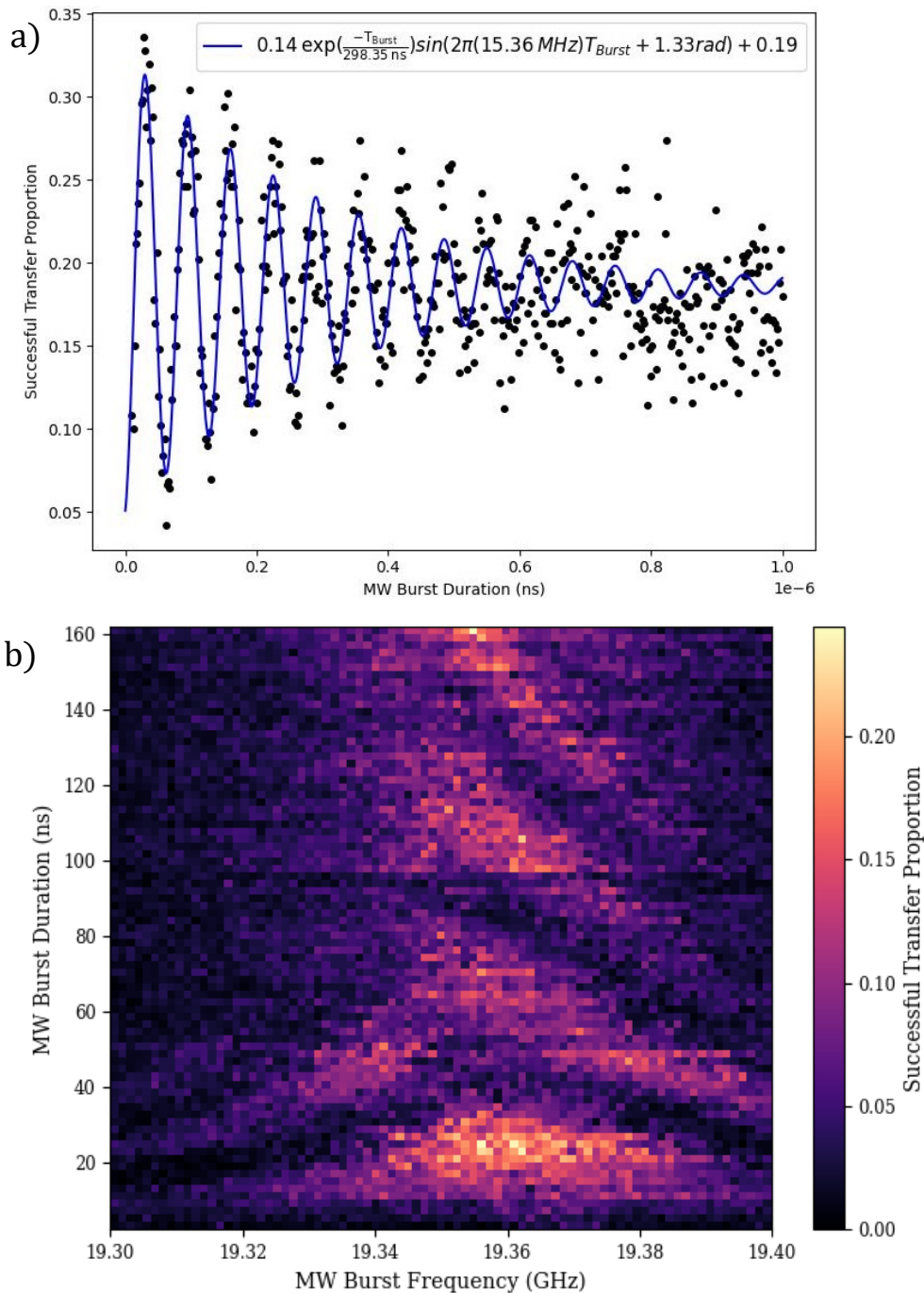
Figure 13: a) First Rabi oscillation experiment conducted at $f_{MW} = 19.38\ GHz, B = 0.925\ T$ with a decaying sinusoid fit overlaid in blue; b) Rabi chevron measured at $B = 0.925\ T$. Note that a telegraphic noise (TN) event occurred between the two experiments, necessitating an alteration of the gate voltage configuration, thus also altering the central frequency.

31

Once the EDSR identity of these spin excitations were verified, Rabi experiments were performed by varying the duration of the burst linearly. Fig 13.a) shows the first successful Rabi oscillations observed in the spin-up proportion. Fig 13.b) shows the first chevron pattern measured by repeating this procedure for changing oscillation frequencies near the central frequency.

"Sweet Spot" Frequency Search

Figure 13.a) shows that with this primitive experimental procedure, T_{Rabi} is relatively short, with coherent oscillations lost to noise for burst durations longer than 600 ns. The chevron in Figure 13.b) also reveals non-ideal characteristics, with the oscillation frequency changing sharply at $f_{MW} = 19.345$ GHz. The cause of these issues was identified to be the inconsistent output power profile at the L gate, with the amplitude of the signal delivered to the L plunger gate varying irregularly based on the frequency chosen. The unknown transfer function of the fridge, wiring, and hardware made it difficult to control the consistency of Rabi frequency across arbitrary ranges of MW burst frequency. Thus, a range of EDSR frequencies was sought for which the Rabi frequency was stable. Furthermore, the decay in the spin-down proportion for increasing burst time, T_{Rabi}, was to be simultaneously maximized.

From the results shown in Figure 12, the central frequency could be determined as a function of the magnetic field. Maintaining the MW burst at the changing EDSR peak frequency across a range of field strengths allowed a search to be conducted for "sweet spots" at which f_{Rabi} varied minimally and T_{Rabi} was as long as possible.
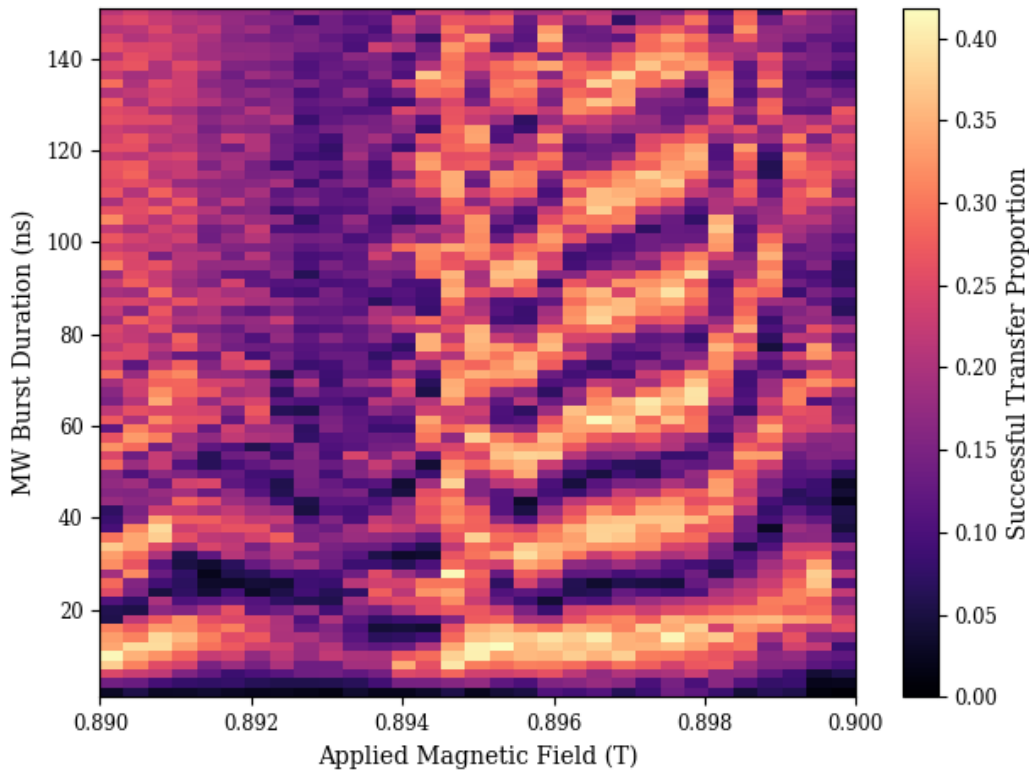
Figure 14: The results of a search for a "sweet spot" at which the Rabi frequency and decay time are maximized but do not vary greatly with small changes in the applied MW burst frequency. These characteristics are found here at and near $B = 0.897$ T.

Figure 14 shows the results of this search at a focused range of frequencies. A combination of the desired Rabi oscillation characteristics was found near the MW frequency of 18.92 GHz, corresponding to a magnetic field strength B of ≈ 0.897 T. Importantly, both f_{Rabi} and T_{Rabi} remain relatively stable between $B = 0.896$ T and 0.898 T. Due to repeated telegraphic noise events, the precise voltage configuration and magnetic field to be applied shifted at irregular intervals. Therefore, for all experiments conducted at this "sweet spot," the magnetic field strength was judiciously chosen to maintain the Larmor frequency of the hole in the left QD in this range of frequencies. Owing to the increased efficacy of the transfer function of the system at these "sweet spots", large temperature increases in the sample were likely produced and contributed to decoherence. It may thus be the case that operating at lower temperatures could extend coherence.

Figure 15.a) shows a Rabi chevron pattern measured after tuning the system to the "sweet spot", with the Larmor frequency at ≈ 18.91 GHz. Visibly, the oscillating areas of high and low spin-up proportion are continuous on both sides of the pattern sans any loss of coherence for off-central frequencies. Figure 15.b) shows a single Rabi oscillation experiment measured at the central frequency, showing the increased $T_{Rabi}(\approx 717$ ns) compared to those measured away from "sweet spot" frequencies.
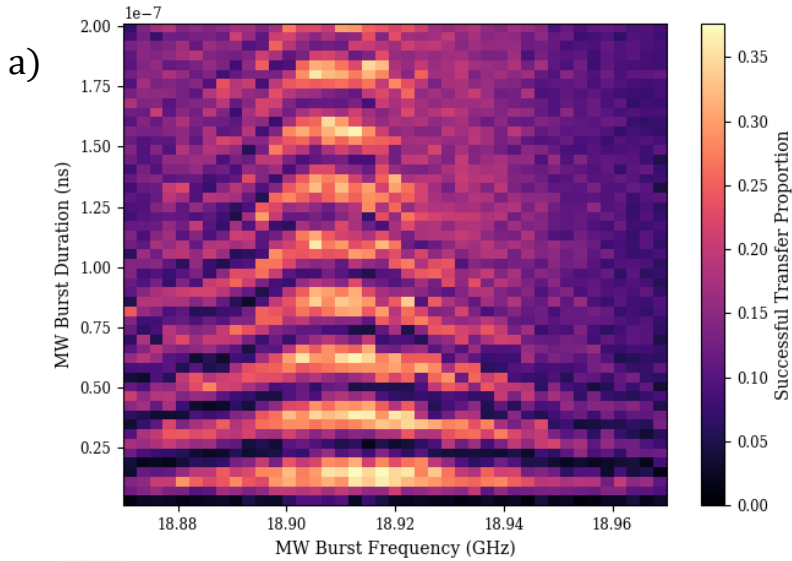
Figure 15: a) Rabi chevron measured at the "sweet spot" described above; b) Single Rabi oscillation experiment conducted at the "sweet spot". The blue overlaid line shows the best-fit line for the oscillations.

33
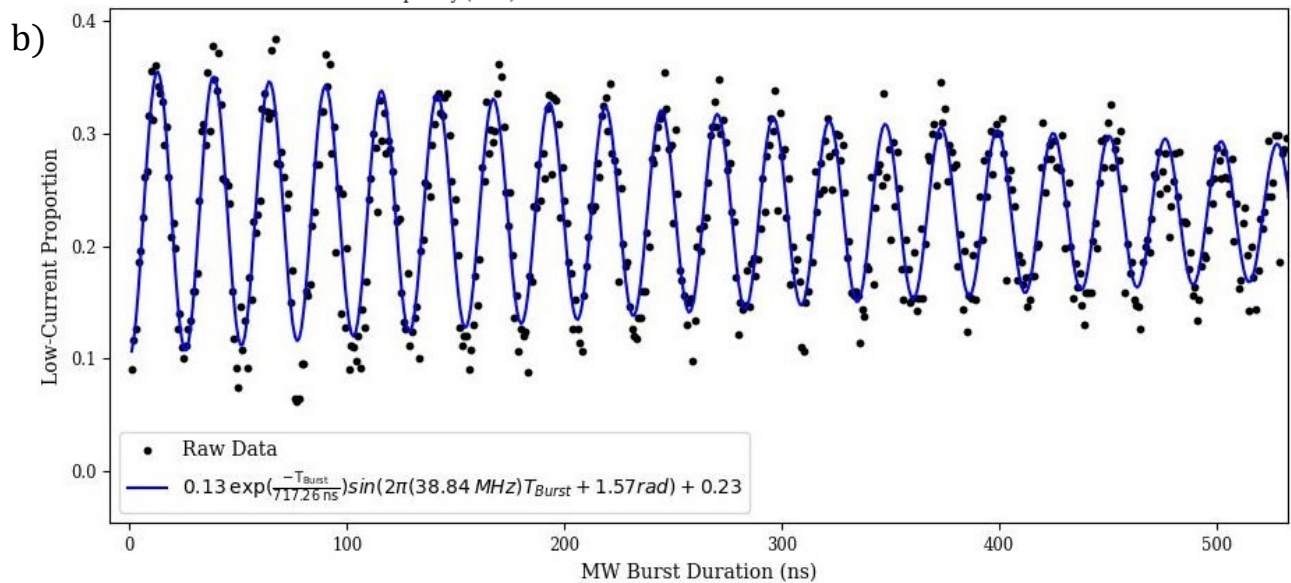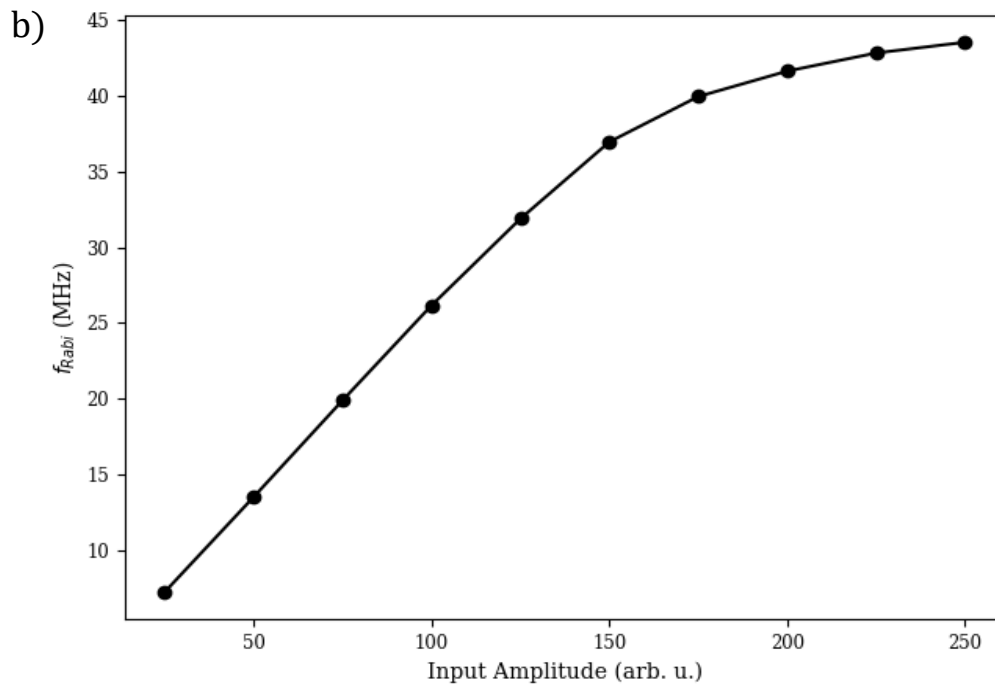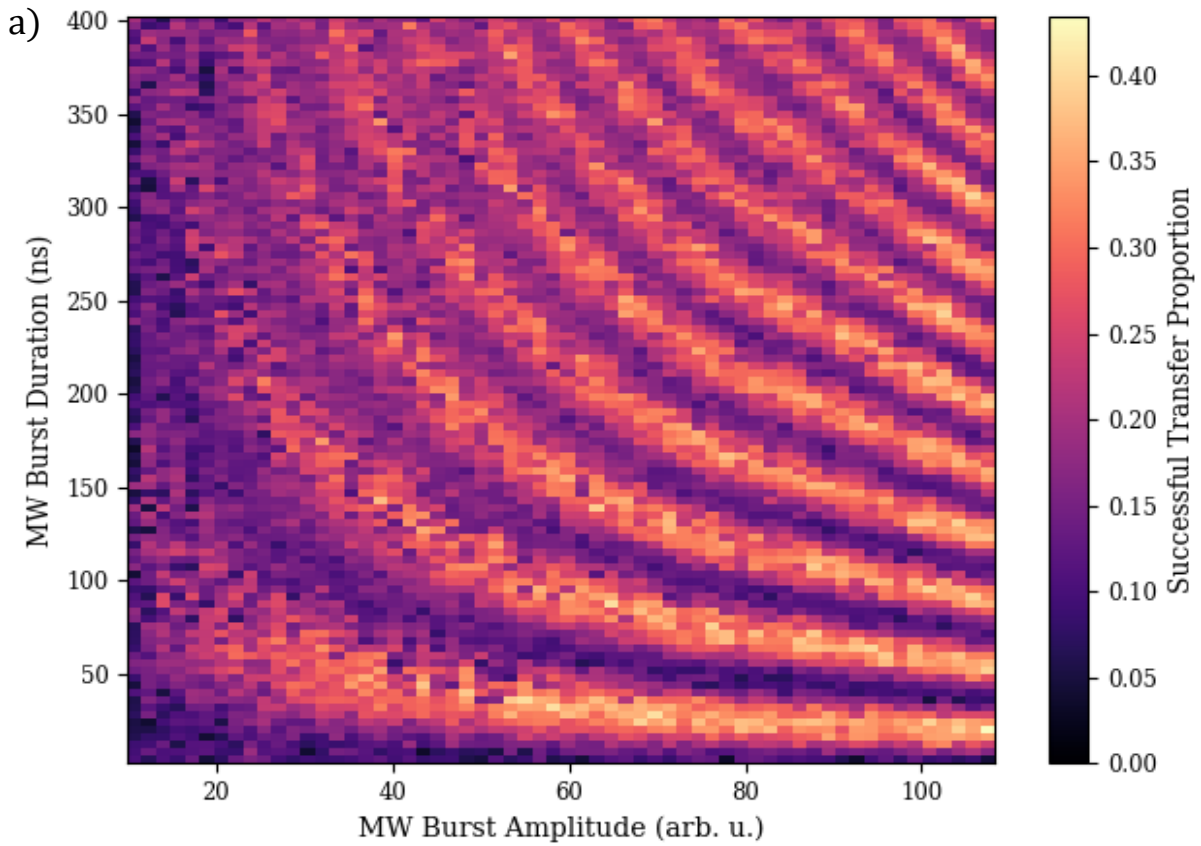
Figure 16: a) Rabi oscillations with increasing frequency and decay time with increasing MW burst amplitude; b) Separate set of Rabi oscillation experiments, from which the Rabi frequency dependence on MW burst amplitude is extracted.

The oscillation frequency is dependent on the amplitude of the MW burst, a property investigated first in Figure 16.a), then again in Figure 16.b) in a set of discrete, repeated experiments whose results are averaged. By altering the amplitude of the trigger signal sent to the MW generator from the AWG, the MW burst amplitude was increased to cause a linear increase in f_{Rabi} up to a given value, after which the frequency increased asymptotically. This relationship between the MW amplitude and f_{Rabi} is extracted from experimental data and shown in Figure 16.b). Noticeably, the Rabi oscillation frequency appears to saturate, asymptotically approaching a value at or near 45 MHz. This behaviour has been observed in other semiconductor spin qubits [73] [74] [75] [76] and is yet to be definitively explained by theory. In the experiments in this thesis, the behaviour is possibly due to the large amplitude of the driving MW oscillations causing an oscillatory variation in the dot g-factor, thus varying the Larmor frequency within each single-shot experiment. The resultant behaviour departs from the two-level approximation and is thus beyond the scope of this work. Subsequent pulsing experiments were therefore performed in the "linear regime" of Figure 16.b) with sufficiently low MW amplitudes.

While performing these Rabi experiments, it was discovered that when Rabi oscillations measured under with the same conditions were repeated, averaging of the spin-up proportions across the experiments led to an increase in the extracted parameter T_{Rabi} in comparison to single traces. In these experiments, conditions appear to remain sufficiently stable between experiments to instead increase these extracted parameters after averaging, suggesting that high-frequency noise has an effect on each trial.

The possible magnetic field dependence of the Rabi coherence time and frequency was investigated by repeating the same experiments at a lower range of magnetic fields. The new "sweet spot" frequency was identified surrounding $f_{Larmor} = 14.94$ GHz after performing the same experiments as in the previous magnetic field regime. Note that the bright bars in Figure 17.a) are caused by the significantly higher MW generator output amplitude over specific frequency ranges.

In this regime, the magnetic field strength was tuned via a new method to precisely choose the Larmor frequency of the hole. The output frequency of the MW generator was set to the "sweet spot" frequency identified in Figure 17.b) for all experiments. Between measurements of Rabi oscillation experiments shown in Figure 17.c), the magnetic field strength was varied in increments of 200 mT. The results of these Rabi traces were fitted to extract T_{Rabi}, the time constant of the exponential decay envelope of Rabi oscillations in. The largest of which would signify the closest alignment of the Larmor frequency with the previously selected $f_{MW} = 14.94$ GHz. The magnetic field value $B = 0.7198$ T was thus selected, barring minor adjustments due to telegraphic noise events, for subsequent experiments in this regime.
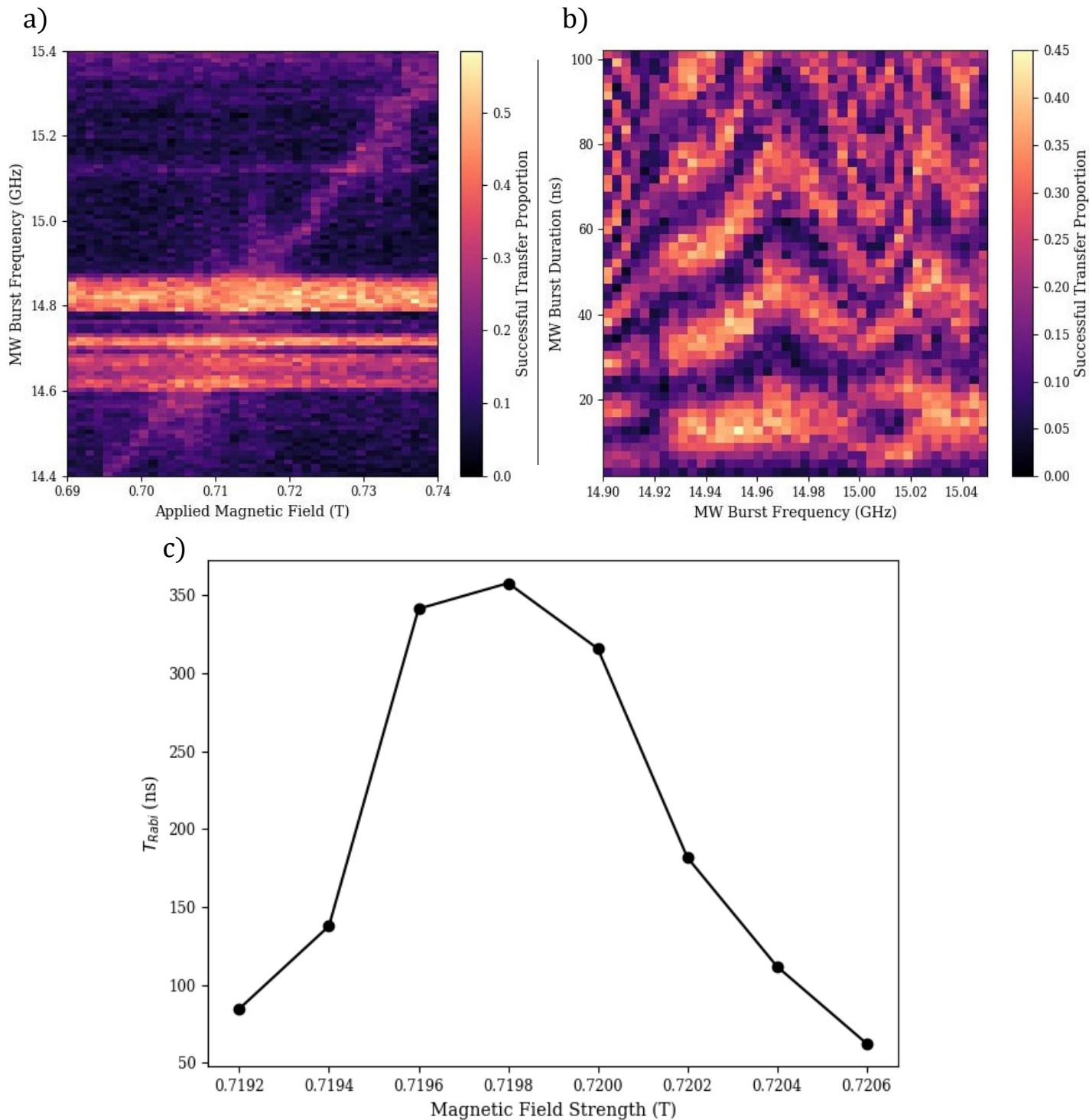
Figure 17: a) EDSR signal measured while varying MW burst frequency over a lower range of field strengths than previous experiments. Bright horizontal regions of high charge sensing current are caused by inconsistent MW output amplitude depending on frequency; b) "Sweet spot" searching experiment in this new regime, located about $f_{MW} = 14.94\ GHz$; c) Extracted T_{Rabi} for a set of experiments of varying magnetic fields. The MW burst frequency is held constant at the "sweet spot", allowing the corresponding magnetic field strength to be identified in order to maximize T_{Rabi}.

Once precisely aligned, repetitions of previous Rabi experiments yielded similar results as in the experiments in the higher-field regime. The chevron measured about this new central frequency shown in Fig. 18.a) exhibited the same reduced T_{Rabi} on the side of higher MW output frequency, just as in the set of experiments for higher B. This structure is reflected in the Rabi traces measured when determining the proper magnetic field: as the central frequency depends linearly on the magnetic field strength, an increase in magnetic field is equivalent to a translation of the chevron pattern towards higher f_{Larmor} (i.e. the right-hand side of the figure). This is possibly due to increased heating of the sample at higher MW burst frequencies. In Figure 18.b), the Rabi frequency increases with MW burst amplitude, with diminishing efficacy for at high amplitudes. Figure 18.c) shows a set of Rabi oscillations for which $T_{Rabi} = 588$ ns, the highest observed at this magnetic field strength.

The "flatness" of the chevron in Figure 18.a) may be caused by a coupling of the nuclear spins to the spin of the hole in the left QD, causing EDSR excitations of similar strength for a range of frequencies about the central frequency. A similar phenomenon was observed recently in a study of electron spins in a GaAs QD device [77], motivating a further exploration of these characteristics. It may also be due to a nuclear polarization effect, theoretically explored in a recent paper [78].
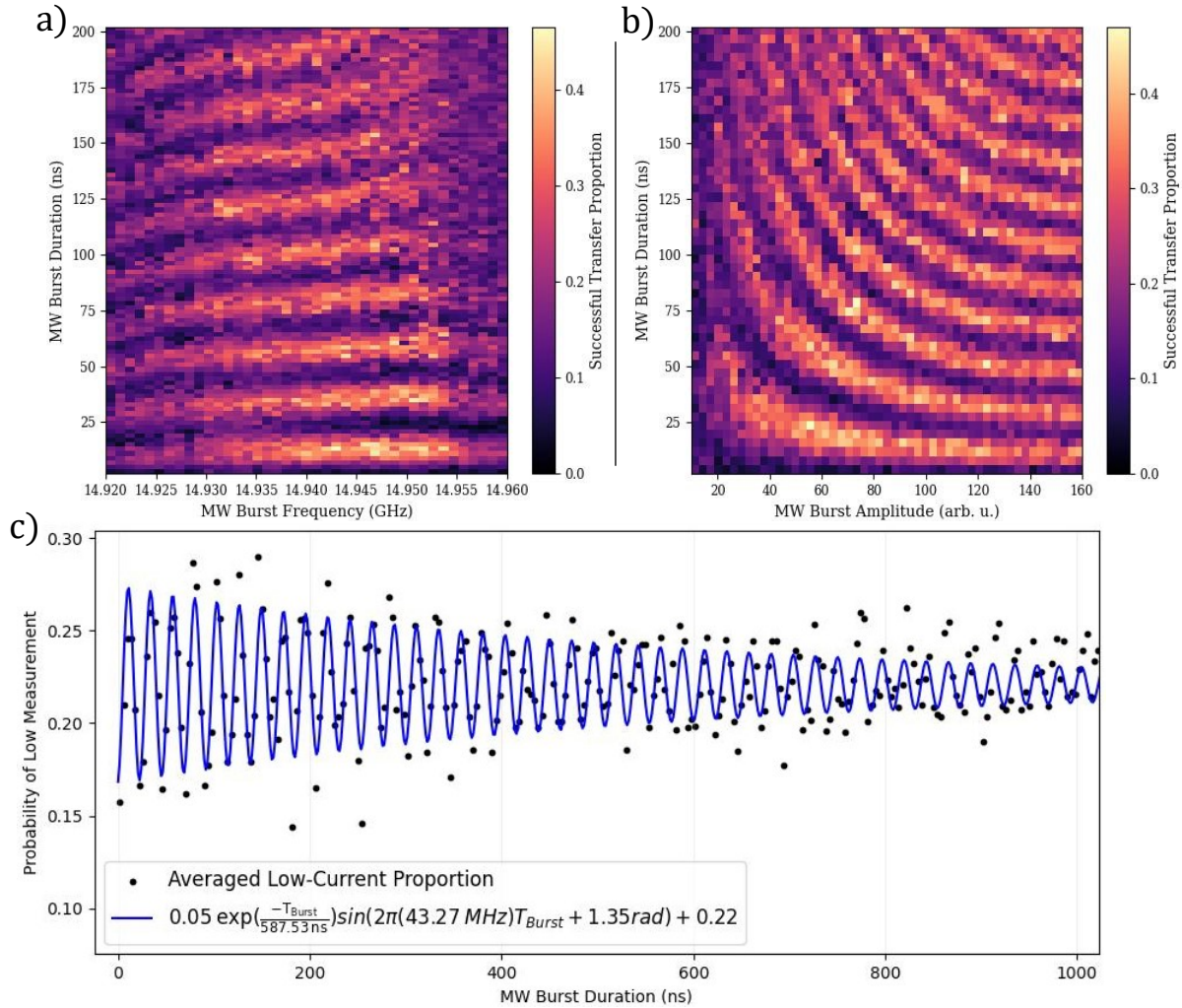
Figure 18: a) Rabi chevron measured in the low-B regime; b) Rabi oscillations with increasing frequency and decay time with increasing MW burst amplitude in low-B regime; c) Single averaged Rabi oscillation experiment with maximal $T_{Rabi} = 588$ ns.

Given that the output amplitude of the MW generator at the sample during operation was unknown even under "sweet spot" calibration, secondary measurements were performed to qualify the dependence of T_{Rabi} on the amplitude of driving oscillations. Experiments were performed in the range of MW amplitudes for which f_{Rabi} scales linearly, from which both f_{Rabi} and T_{Rabi} were extracted.
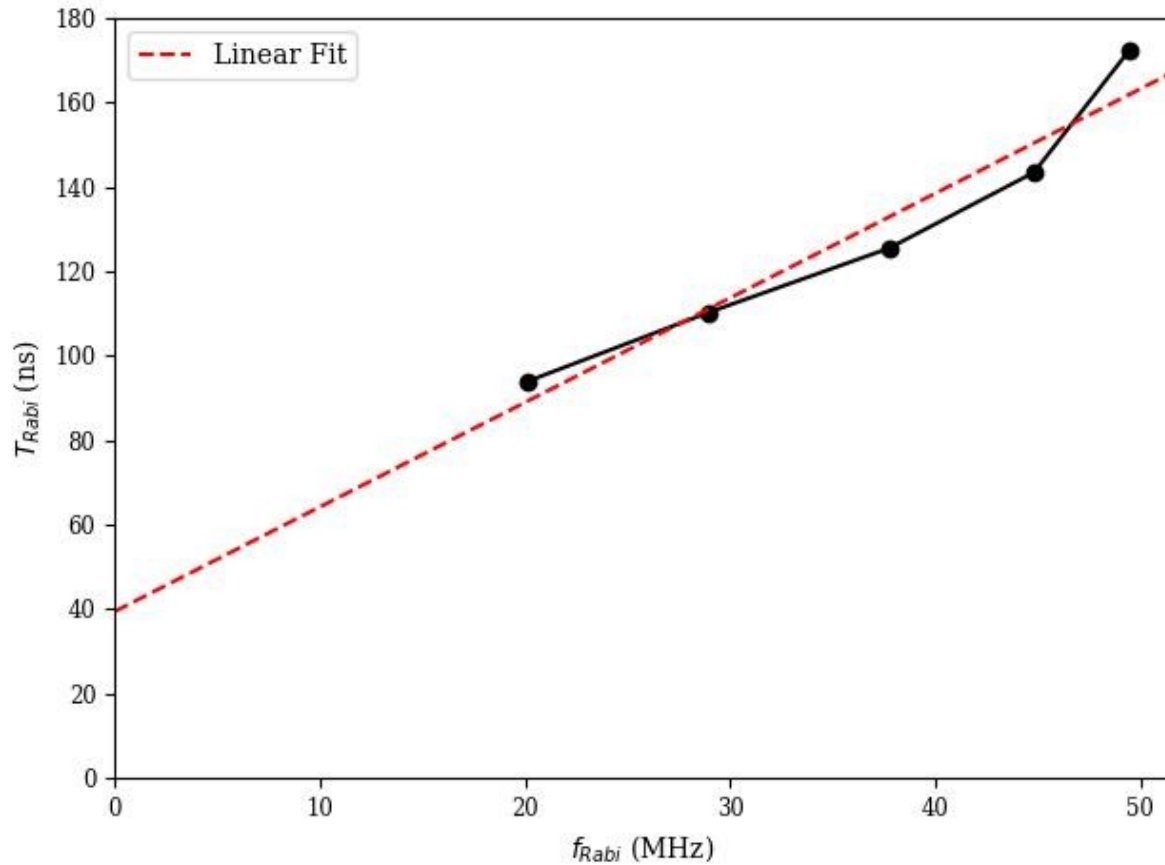
Figure 19: Comparison of Rabi frequency and decay time. Each point represents the parameters extracted from the average of six repeated experiments conducted under the same conditions. The red dotted line represents a linear fit of the data points and is extended to highlight its non-zero intercept.

As this method has not been commonly used to analyze T_{Rabi}, no comparable contemporary is available which compares f_{Rabi} and T_{Rabi} in the manner shown in Figure 19. However, theoretical analysis of driven Rabi oscillation decay in spin qubits [67] finds that the positive correlation of T_{Rabi} with f_{Rabi}, and therefore with the amplitude of the driving oscillations, implies that the Rabi coherence time is dependent most strongly on the hyperfine interaction with nuclear spins [1].

By inspection, the results may suggest a linear fit. When the line of best fit is extracted from the data, the resultant line does not meet the origin. A possible improvement of this analysis could be to include the decoherence processes involved in T_2^* decay when inspecting the coherence of driven oscillations [1], though this would require further experimentation with smaller driving field amplitudes.

Ramsey Experiments (T_2^*)

      With the "sweet spot" frequencies precisely identified and the proper pulse durations determined for each of the two magnetic field regimes, Ramsey experiments could be conducted to determine the T_2^* spin coherence time of the heavy hole. The duration of a each $\pi/2$-pulse was calibrated to and held constant at 9 ns, while the MW burst frequency and the duration between the $\pi/2$-pulses, T_{Wait}, were varied in order to produce the Ramsey fringe patterns in Figure 20.
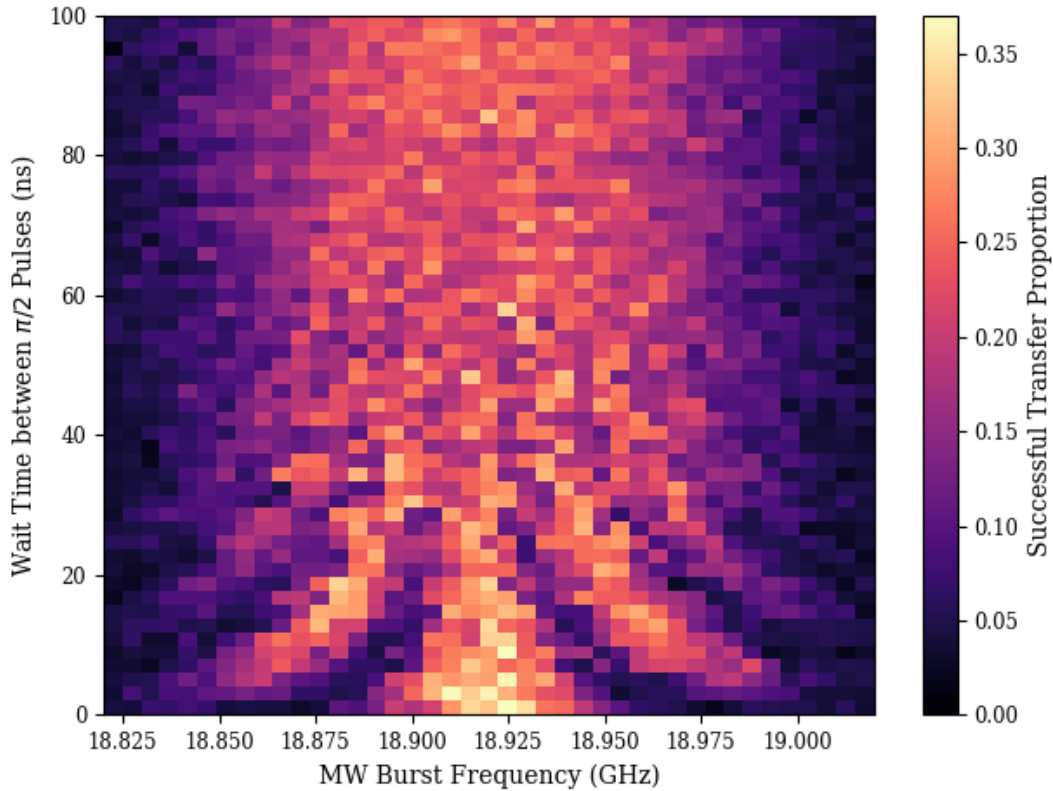
Figure 20: Ramsey fringe pattern measured in the high-B regime.

      Figure 20 shows a Ramsey fringe pattern measured at $B = 0.89$ T. For short wait times, the fringe pattern is clearly visible about the central frequency. However, for wait times beyond 60 ns, coherence is completely lost, with the visible separation of adjacent fringes becoming unclear and a single broad peak in spin-up proportion remaining about $f_{MW} = 18.92$ GHz. Repeated experiments with fine alterations of pulse durations and alignment with the central frequency did not improve results.

      Averaged Ramsey experiments along the central frequency were used to precisely determine the value of T_2^*, in which experiments were performed at the central frequency while varying the wait time logarithmically. The spin coherence time was extracted by fitting these results with an exponentially decaying function. The coherence times for the system at the two different magnetic
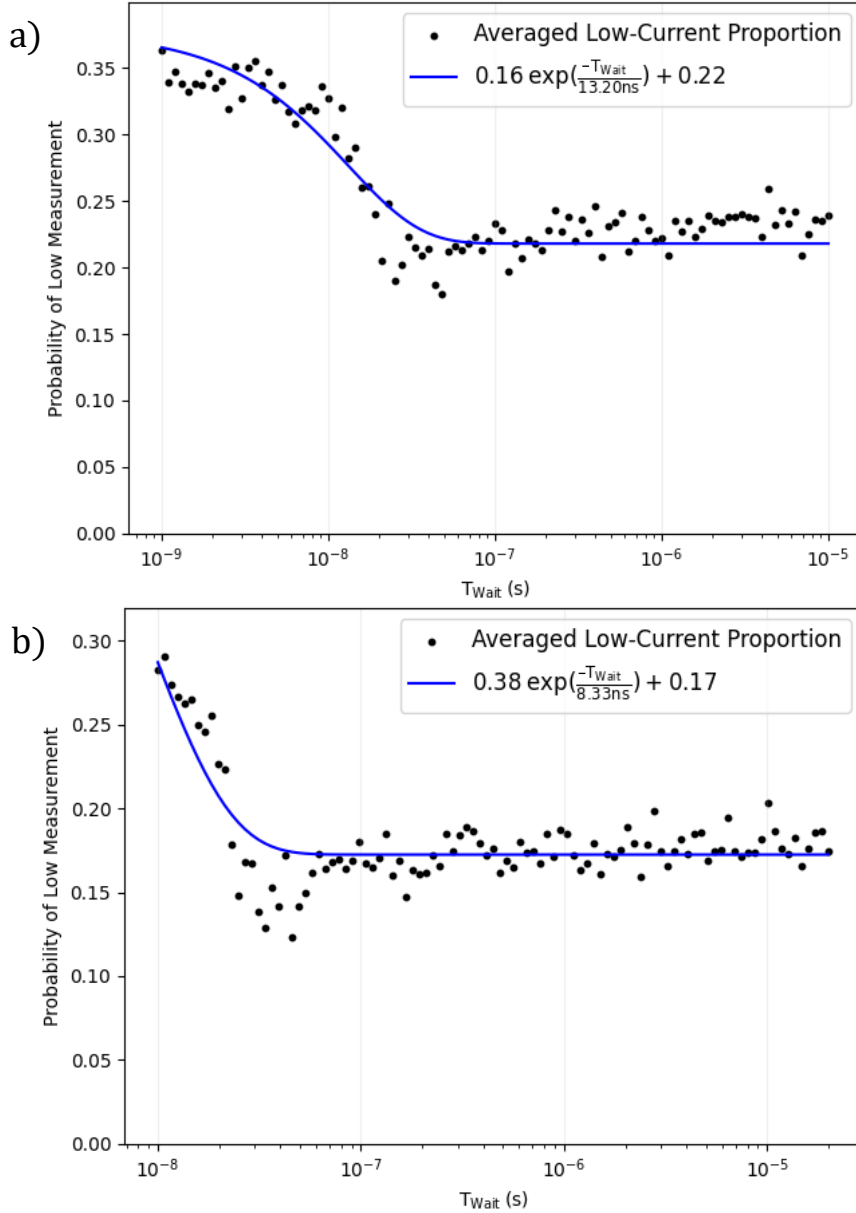
Figure 21: a) Averaged Ramsey experiments performed at the central frequency in the high-B regime; b) The same experiments performed at the central frequency in the low-B regime.

fields were similar, with $T_2^* \approx 13.2 \ ns$ extracted at $B = 0.8975$ T and 8.3 ns at $B = 0.7195$ T for the results shown in Figures 21.a) and b), respectively.

After coherence is lost in each of these Ramsey traces, the probability of the hole ending each single-shot cycle in the right QD approaches half of the peak value. This is due to the diminishing effect of the first $\pi/2$-pulse on the resultant hole-spin state. As the wait time extends to multiple spin-coherence times, only the second pulse, with a fixed 50 ns delay before charge transfer in each single-shot cycle, has an effect on the output state. Being a $\pi/2$-pulse, this results in a spin-up proportion that is half of that produced by a full π-rotation (i.e., two pulses with no wait time in between them).

The maximum extracted T_2^* coherence time of 16 ns is comparable with coherence times measured in electronic devices in GaAs [69]. This is unexpected, as the reduced hyperfine interaction of holes with the nuclei led to the prediction that p-type devices would benefit from extended coherence times. However, other characteristics of hole-based QDs may counter this effect. For example, the large effective mass of heavy holes reduces the size of the QD, reducing the number of nuclei with which it interacts. The magnitude of nuclear field strength fluctuations is inversely proportional to $1/\sqrt{N}$, where N is the number of interacting nuclei, thus increasing these perturbative effects on the QD [1]. As well, QD anisotropy due to asymmetry leads to a mixing of the energy levels of light- and heavy-holes. This increases the strength of the hyperfine interaction between heavy holes and lattice nuclei, leading to accelerated spin dephasing [79]. These two factors can be addressed by constructing a device with larger QDs and improved dot symmetry.

A recent paper by Nguyen et al. [77] proposes and implements "nuclear-spin cooling" on an electron-based, self-assembled GaAs QD device that increased T_2^* by over two orders of magnitude. In this pulsing scheme, a Rabi pulse is applied before performing a Ramsey experiment in order to reduce the standard deviation of the fluctuations in the resonant frequency of the dot. Furthermore, a quantum sensing algorithm developed by Jackson et al. [80] was successfully implemented, extending coherence times even further to a reported $T_2^* = 608$ ns, a significant increase from $T_2^* = 3.9$ ns when no cooling method was employed. Such improvements are vital for the candidacy of QD devices for quantum computing and could lead to significant coherence time increases if implemented on a p-type device with the aforementioned improvements in dot construction.

Hahn-echo and CPMG Pulse Sequence Experiments (T_2^{CPMG})

In order to continue measuring and extend spin coherence times, Hahn-echo and CPMG pulse sequences were employed. In each of these pulse sequences, one or more additional "refocusing" π-pulses are inserted between the two $\pi/2$-pulses of the Ramsey sequence. These additional pulses reverse spin-dephasing processes, thereby extending the state coherence.
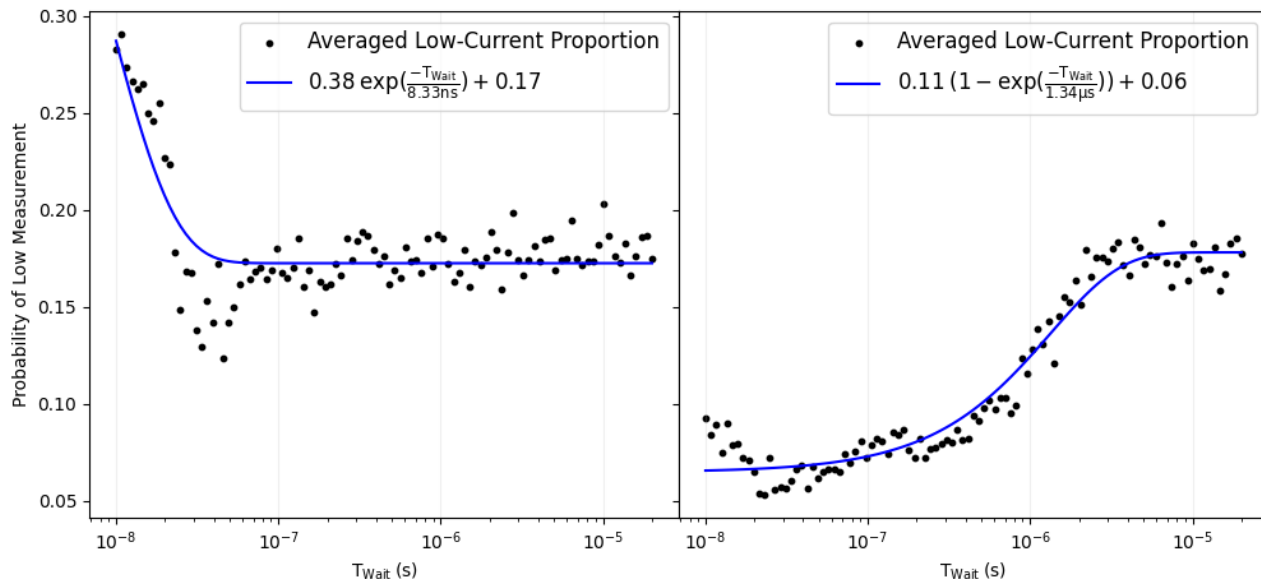

Figure 22: Averaged Ramsey (Hahn) experiment performed at the central frequency in the low-B field regime in the left (right) panel.

Figure 22 demonstrates the extension of the coherence time via the addition of a single π-pulse (i.e., the Hahn-echo pulse sequence) by contrasting their spin-up proportions on the same vertical axis. Depicted are the Ramsey and Hahn-echo measurements taken in the lower B-field regime. In the left panel, the action of two successive $\pi/2$-pulses produces a net π rotation, leading to a maximal spin-up proportion when the delay between pulses is short. In contrast, the net action of the Hahn-echo pulse sequence in the right panel is a 2π rotation, meaning a minimal spin-up proportion for short wait times. For both sequences, however, a sufficiently long delay between pulses causes only the action of the final $\pi/2$-pulse to affect the final spin state. Thus, the spin-up proportion approaches a similar intermediate value in both experiments.

Following the extension of the coherence time of the system with a single refocusing pulse, experiments employing the CPMG sequence, containing multiple refocusing pulses, were conducted with the aim of further extending of the lifetime of spin information on the left QD.

In similar works [81] [82], the number of refocusing pulses is increased exponentially to demonstrate the diminishing effectiveness of large numbers of refocusing pulses in increasing coherence time. For the experiments in this work, hardware limitations prevented large numbers of refocusing pulses to be employed. In order to perform each single-shot cycle with the desired pulse durations and voltages, a file containing the gate voltage for each step had to be uploaded to the AWG. The format of the file dictated that a voltage value be assigned for each frame in which the AWG must generate a non-zero voltage. The user-defined resolution of these frames had to be made short enough to provide the duration needed to create pulses and wait times of precise length. Furthermore, the total duration spent away from the measurement position in each single-shot cycle had to be constant throughout all experiments to prevent the average voltage from differing between pulsing experiments at the same location in voltage space. However, a maximum file size and an increase in the time between sets of measurements motivated a reduction in this resolution.

The AWG resolution was set to 1 ns when the spin-to-charge readout scheme was first implemented, allowing greater precision in the extraction of T_2^* by increasing the number of data points measured for short wait times in Ramsey experiments. In order to alter the resolution of the AWG, a full software restart on the device would be required, thereby necessitating such processes as a clock resynchronization of the secondary AWG controlling the MW generator. The time required to perform these processes was sufficiently long that TN events were likely to arise in the interim, necessitating gate voltage re-tuning and thus causing further delay the resumption of experiments. Furthermore, the collection of these data sets began concurrently with the beginning of the global helium shortage in early 2022, further accentuating the need for expedience. Thus, the resolution was not modified for Hahn-echo and CPMG sequence-based experiments. A simple extension of this project would be to decrease the resolution to equal that of a $\pi/2$-pulse (in our case, 9 ns) for such composite pulse experiments to maximize the data efficiency when uploading to the AWG, thereby increasing the maximum duration and N_{CPMG}.

The CPMG pulse sequence involves the inclusion of N_{CPMG} refocusing π-pulses between the first and last $\pi/2$-pulses. Given the aforementioned limitations, experiments involving refocusing pulses were limited to a maximum duration of 30 μs. For pulse sequences involving one or more refocusing pulses, the duration of the sequence as a function of N_{CPMG} and T_{Wait} is given by the following equation:

$$T_{total} = 2(N_{CPMG} + 1)T_{\pi/2} + N_{CPMG}T_{Wait} + T_{Off} \tag{14}$$

For all CPMG pulse sequences used, T_{total} could not exceed the duration spent at the driving step. In addition, the time spent at the driving position was held fixed at 30 μs across all single-shot cycles, a maximal value given the limitation due to file size. This meant that T_{total} was also limited to 30 μs, including π- and $\pi/2$-pulse durations and the delay between the end of the final pulse and the beginning of the transfer step. Comparable works [81] [82] analyze the extension of the coherence time by increasing N_{CPMG} exponentially and measuring the state coherence with respect to T_{total}. With a relatively short maximum T_{total} available in this work, CPMG experiments could only be conducted for small, linearly increasing values of N_{CPMG}. Experiments involving values greater than $N_{CPMG} = 3$ did not produce a range of results sufficient to extract T_2^{CPMG} with a good fit for a maximum total wait time of just under 30 μs, as the maximum possible dephasing time between subsequent refocusing pulses decreased with $1/N_{CPMG}$.

Figure 23 shows the data collected when measuring spin-up proportion at the resonant frequency for increasing T_{Wait}. Figure 23.a)-d) shows the extracted spin coherence times for each of these experiments in the high-B regime. Refocusing pulses included beyond the first do not increase the coherence time as significantly as does the Hahn-echo pulse sequence when compared with the Ramsey, which increased coherence time by nearly two orders of magnitude. Coherence time values extracted from experiments conducted at the two different magnetic field values in this work were not significantly different, as shown in Figure 23.e). However, it is possible that much larger numbers of refocusing pulses, as aforementioned, may increase T_2^{CPMG} significantly as in other works.
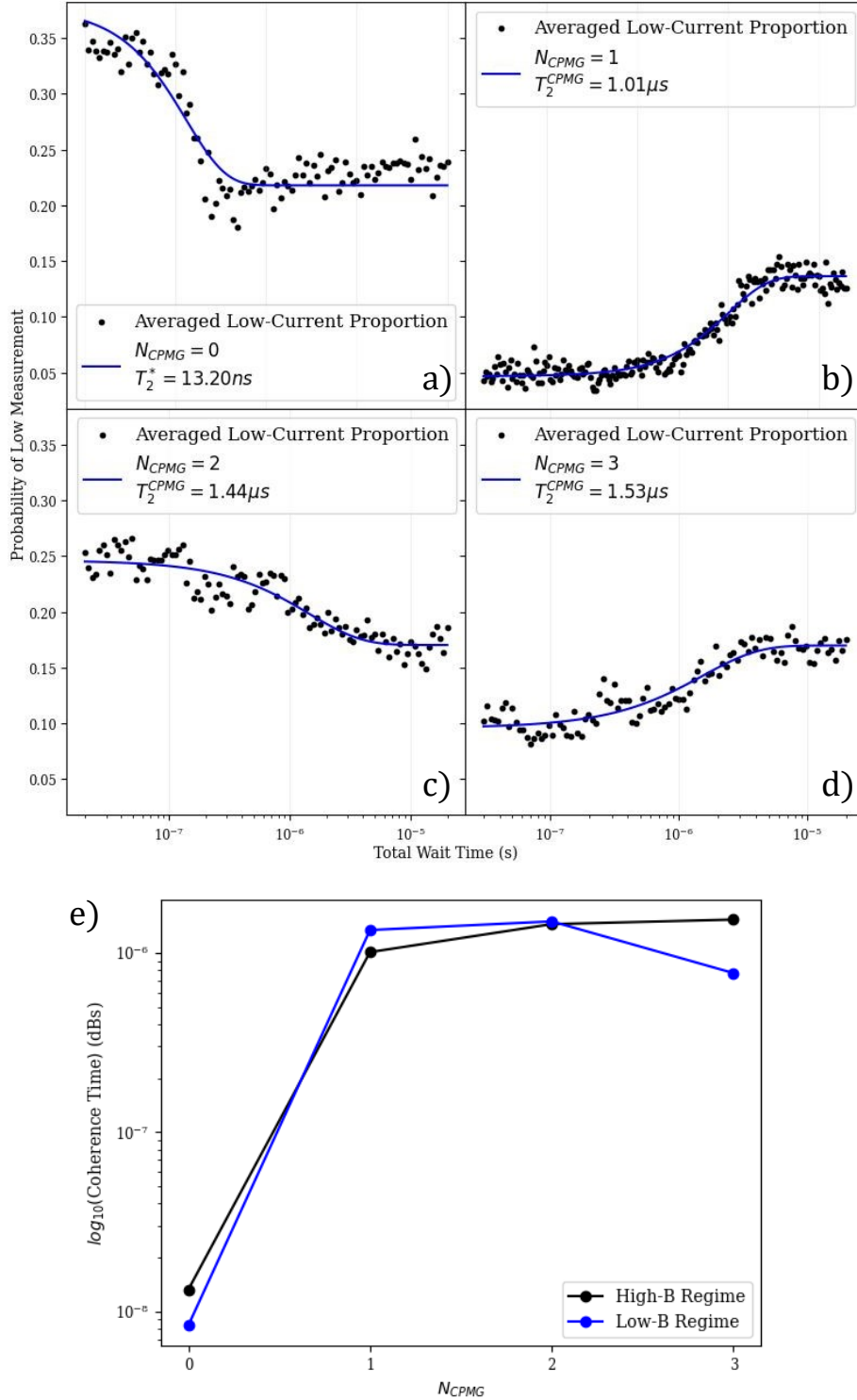
Figure 23: a)-d) Results of averaged Ramsey, Hahn-echo, and CPMG experiments for $N_{CPMG} = 2$ and 3. These experiments are performed in the high-B regime; e) Comparison of coherence times in the two magnetic field regimes, with a logarithmic scale in the y-axis to highlight the improvement after refocusing pulses are introduced as well as the similarities between the results in the two different regimes.

Qubit and Gate Quality Factors

Using the maximal values of f_{Rabi}, T_{Rabi}, and T_2^* extracted in each of in the two magnetic field regimes, the QQF and GQF were calculated.

Magnetic Field Strength (T)	Maximal f_{Rabi} (MHz)	T_2^* (ns)	QQF	Maximal T_{Rabi} (ns)	GQF
0.8975	43.6	16.6	0.72	717	31.3
0.7196	53.2	13.1	0.70	598	31.8

Table 1: Tabulation of highest Rabi oscillation parameters and spin coherence times in the two magnetic field regimes. The QQF and GQF are also calculated for each.

The QQF values are significantly lower than those measured on comparable contemporaries in varying materials and charge carriers, as high as $QQF = 52$ on a planar germanium single-hole spin DQD [83] and $QQF = 200$ on a many-electron silicon qubit [84]. Similarly, the similar GQF values of ≈ 32 are much lower than other modern devices, with a peak of 888 on a Si/SiGe single-electron spin qubit [85].

It is important to note that during Rabi experimentation, the output power of the MW generator was kept at an intermediate level to avoid possible overheating effects from the signal sent to the DQD device. For this reason, it may be possible to further extend f_{Rabi} in further experiments; therefore, the maximal QQF for this device could rise over 1 if the signal amplitude were increased, representing a simple extension of these experiments for optimization.
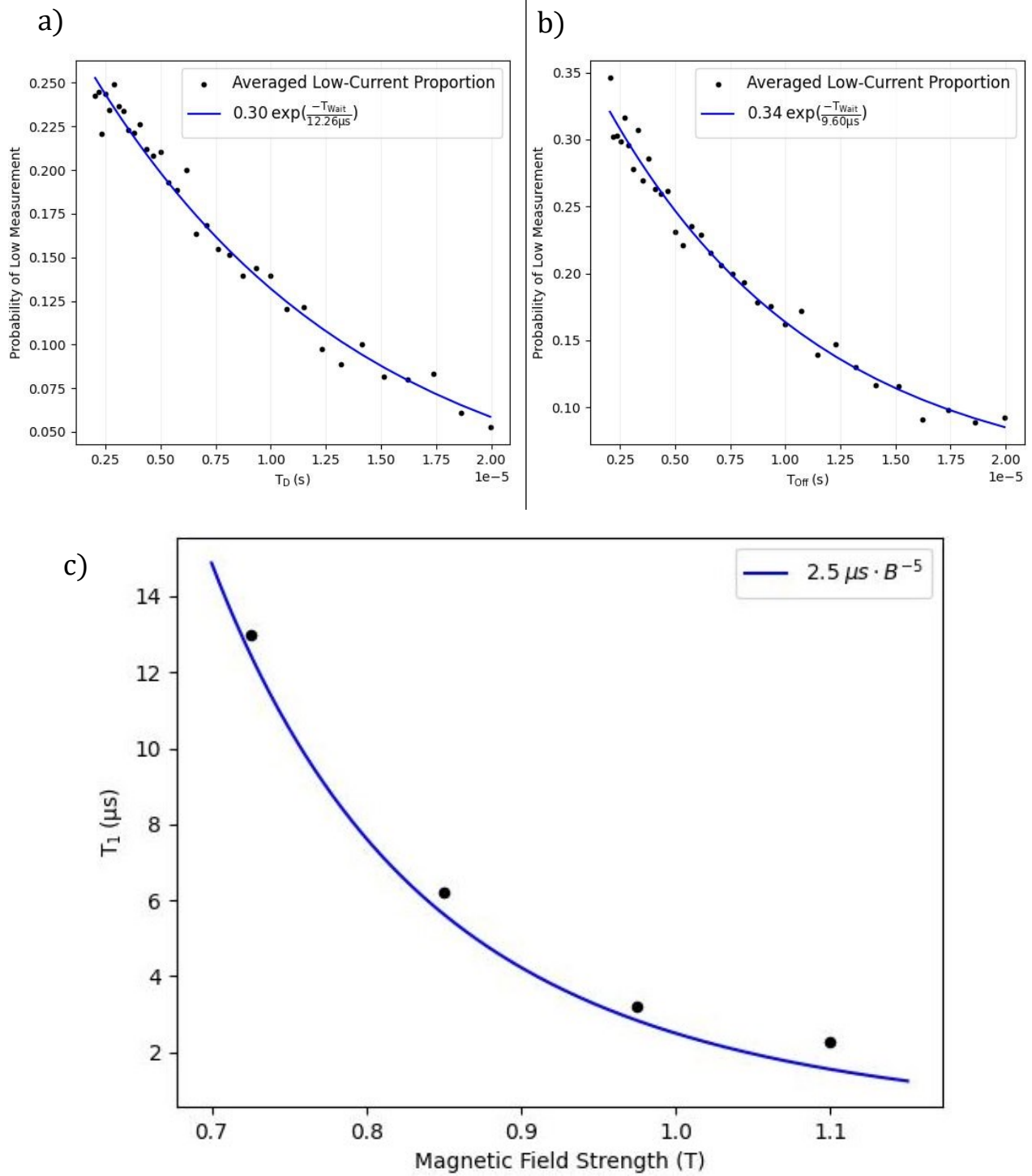
Figure 24: a) Spin relaxation time T_1 measured by varying the duration of the driving ("D") step logarithmically; b) Spin relaxation time T_1 measured by initializing the hole spin state via EDSR, then varying the delay until hole transfer logarithmically; c) Comparison of T_1 values measured by the method in a) to the fit function determined by Bogan et al. [34].

Control and Measurement of Spin Relaxation Time via Two Methods

As part of the characterization of this system, the T_1 spin relaxation time was also investigated as in previous experiments on the same sample [34]. Between the measurements of results in other works and the experiments in this work, a warm-up and cool-down of the sample was performed. The similarities in the results verify the consistency of device characteristics. In this work, however, two different methods of extracting T_1 were employed.

Figure 24 shows the results of two experiments conducted at the same magnetic field ($B =$ 0.7195 T), employing different methods of measuring T_1. Figure 24.a) displays the results retrieved via an appropriation of the method used by Bogan et al. in 2019 [34]. As in the above readout method, the holes are first emptied to ensure (0,0) hole occupation at the beginning of each single-shot cycle. The second initialization step is then omitted, while the duration of the driving step is increased logarithmically. The spin-up proportion extracted from these experiments is then fitted with an exponentially decaying function to extract T_1. The spin relaxation time of 12.97 μs determined via this method agrees closely with the fit function determined by Bogan et al. [34] for the magnetic field employed, following a B^{-5} dependence. The results of these experiments at various magnetic fields are compared to the function $T_1 = 2.5$ μs $\cdot B^{-5}$ determined in previous experiments on this device [34] are shown in Figure 24.c).

Figure 24.b) shows the data retrieved via a different method for determining T_1. In this method, the second initialization and driving steps are maintained at the durations used during Rabi, Ramsey, and other pulsing experiments. Rather than relying on the spin-up state to be initialized when a hole tunnels into the left dot during the second initialization step, the system is instead held at the initialization condition for many multiples of T_1 in order to ensure that the hole relaxes to the spin-down state. The hole is then excited to the spin-up state by a single $\pi/2$-pulse, after which time the system remains at the driving voltage for a duration T_{Off} before moving to the hole transfer step. This free evolution time is varied logarithmically to allow spin relaxation to be observed.

When applying the same fit function to this set of data, a somewhat shorter T_1 of 9.6 μs was extracted, not predicted by the B^{-5} dependence previously determined. This difference in spin relaxation time could be caused by the heating effect of MW pulsing on a gate adjacent to the left QD, in which the hole is situated while relaxation occurs. A change in device temperature and the possible production of phonons may lead to the accelerated spin relaxation.
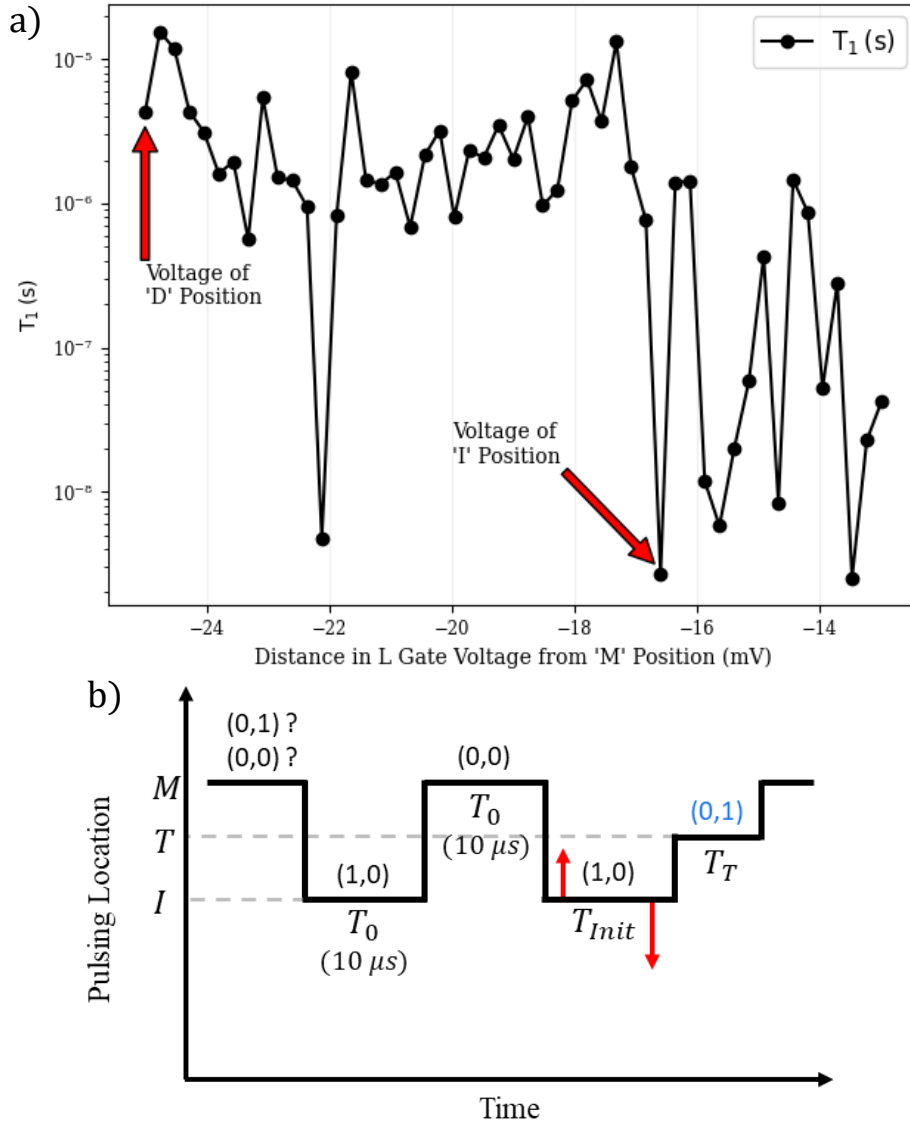
Figure 25: a) Measurement of T_1 relaxation time via the same method used in Figure 24.a) as a function of the voltage of the driving ("D") step. Indicated are the voltages of the initialization ("I") and driving ("D") positions of the readout scheme used throughout this work; b) Diagram showing the changes in the voltage of the "I" step of the readout scheme used to acquire the data shown in a).

The possible L gate voltage-dependence of T_1 was also investigated using the pulsing sequence shown in Figure 25.b). The results of this experiment, shown in Figure 25.a), shows variation in T_1 relaxation time depending on the distance in L gate voltage from the "M" position. These findings suggest the difference in relaxation time between the latest results and those found by Bogan et al. [34] could potentially be due to the difference in L gate voltage during the relaxation process. However, due to the shutdown of the wet fridge necessitated by a helium shortage, the established method of averaging multiple trials at the same gate voltage configuration was not possible to perform. In in future, repeated experiments could be conducted using each of the two methods of relaxation measurement while varying the L gate voltage at which the relaxation process occurs to further explore this phenomenon.

Electrically Tunable Dot Effective g-Factor

Alongside the characterization of the DQD device via coherence time measurements, experiments were conducted to explore electrical control of the dot g*-factor. This was achieved by altering the L gate voltage during the driving step of each single-shot cycle, thereby moving the driving position closer to the charge addition line in L-R voltage space.
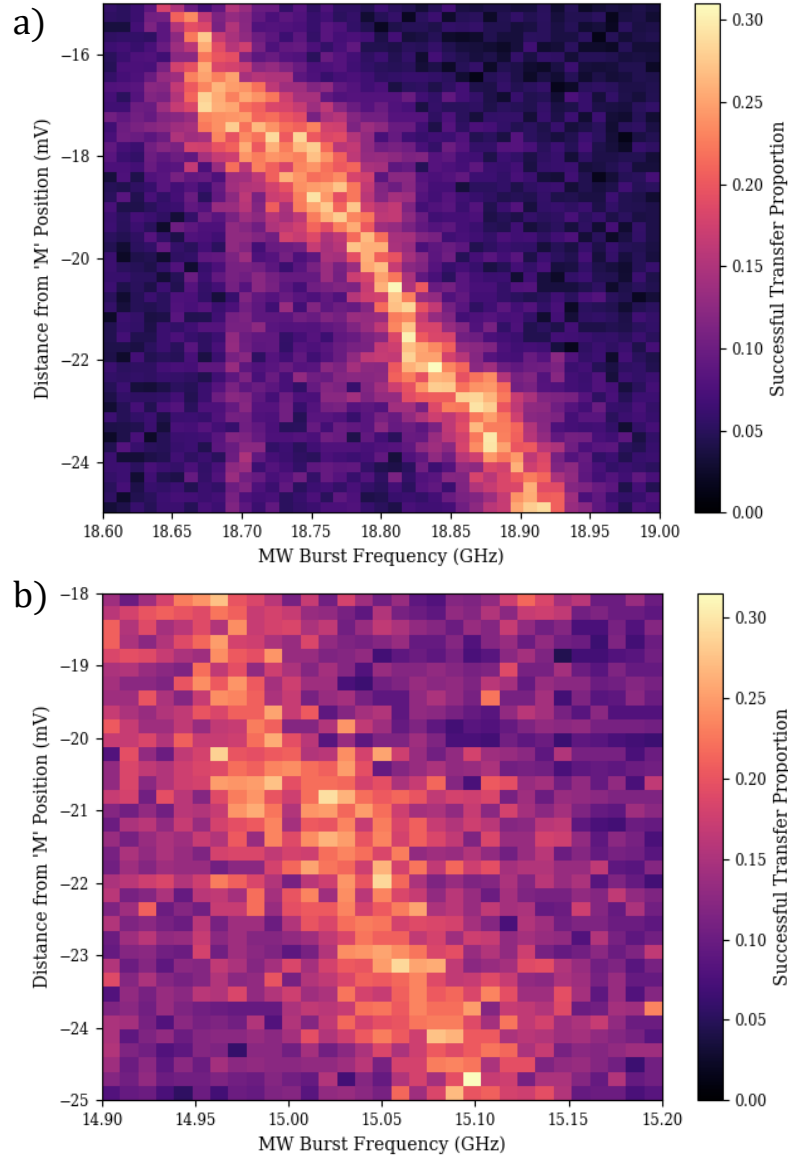
Figure 26: a) Changing EDSR central frequency for varying voltage of driving ("D") step within each single-shot cycle in high-B regime; b) Same experiment performed in low-B regime.

Figure 26.a) shows the results of one of these experiments conducted at $B = 0.89$ T. A single burst from the MW generator was applied for 2 μs for each single-shot experiment in order to produce an intermediate spin-up proportion visible regardless of proximity to a "sweet spot" of the MW generator. A near-linear dependence can be seen, with the central frequency of the dot increasing as the driving point moves away from the measurement ("M") position and therefore the (0,0) - (1,0) charge addition line. (Similar experiments began that also included variations in R gate voltage but proved unsuccessful, as voltage changes applied by the AWG were shown to not reach the

sample.) The magnitude of g^* was changed by approximately $\pm 1.4\%$. A greater range in the driving step voltage would theoretically allow for greater modification but was bounded by the presence of the charge transfer line above and the lowest voltage allowed by the AWG below.

This experiment was replicated at $B = 0.7195$ T, as shown in Figure 26.b), though the distinction between points on and off the EDSR excitation line is less than those at higher magnetic field values. This may be due to the increased MW generator output amplitude near $f_{Burst} = 15.1$ GHz, as shown in Figure 17.a). Though the range of voltages investigated was narrower than in Figure 26.a), the slope of the excitation line suggests a similar tunability. Both demonstrations, however, are less effective than the maximal capabilities demonstrated via other mechanisms [86] [87]. Nonetheless, further investigation of this voltage dependence is an attractive prospect.
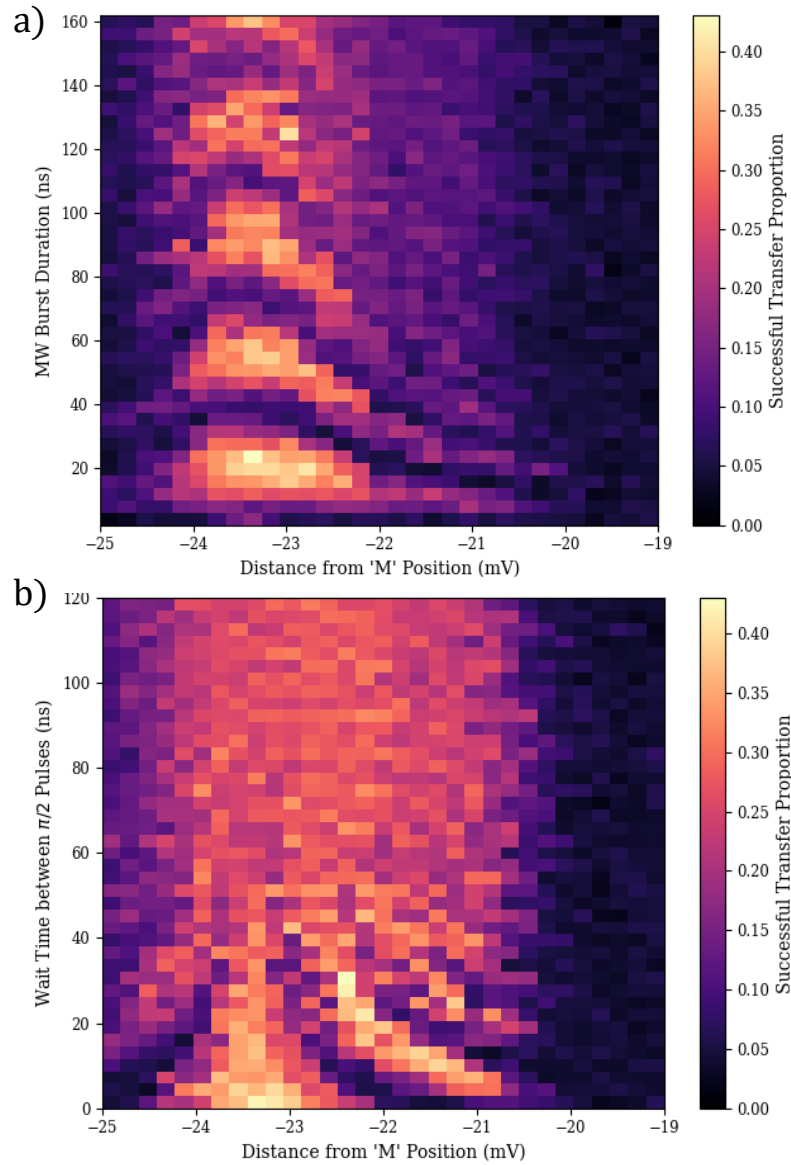
Figure 27: a) Rabi chevron produced by varying the voltage of the driving ("D") step within the single-shot cycle to alter the EDSR central frequency; b) Ramsey fringe pattern produced via the same method.

Figures 27.a) and b) show a Rabi chevron and Ramsey fringe pattern, respectively, measured in the high-B regime by exploiting the gate voltage-dependence of the g-factor. The MW burst frequency and the magnetic field were held constant, instead varying the L gate voltage detuning of the driving step. These experiments demonstrate the viability of this effective g-factor tuning method for dot addressability applications in potential large-scale quantum computer applications in the future.

This effect of electrical g-factor tuning is potentially caused by the changes in dot shape. Due to the layout of the DQD device, a single-gate voltage alteration will necessarily produce an asymmetrical change in potential across the QD. Thus, voltage detuning during the spin manipulation step of the readout scheme will cause a change in dot shape, affecting light-hole-heavy-hole mixing and therefore the Zeeman energy between the hole spin states [88]. An additional extension of these experiments would be to investigate the dependence of the dot g-factor on the voltages of the other gates in the system. This would require a modification of the wiring to allow MW frequency voltage modulation of gates other than the L gate. Combined with a greater range of gate voltages accessible within each single-shot cycle via hardware improvements, future experiments may lead to a greater tunability of g^*.

Conclusions and Outlook

The results presented in this work are the first successful study of the coherence characteristics of a single heavy hole in a lateral GaAs/AlGaAs double quantum dot device tuned to the latching regime. Preliminary results of a new method for electrical tuning of the dot effective g-factor were also presented.

The coherence characteristics of a single hole in a lateral gated GaAs/AlGaAs double quantum dot device have been studied. In contrast to the projected improvements in coherence times, the maximal T_2^* coherence time of 16 ns measured on the p-type device are similar to the coherence time of 10 ns reported in few-electron devices [43]. The maximal qubit quality factor measured in these experiments was ≈ 0.72, well underneath such recently-achieved peaks as 200 in silicon [84]. Similarly, the maximal gate quality factor of 32 does not approach the peak value of 888 achieved in Si/SiGe [85]. This may be attributable to dot anisotropy due to the non-uniform shape of the quantum dot, affecting the light-hole-heavy-hole mixing [79] [88]. Modification of the dot geometry to reduce anisotropy could thus extend coherence times. Additionally, the relatively large effective mass of heavy holes when compared with electrons leads to a reduction in the size of the quantum dot itself. As the strength of the nuclear effective field fluctuation scales with $1/\sqrt{N}$, where N represents the number of nuclear magnetic moments that interact directly with the hole spin, the reduced size of the dot lowers the number of nuclei that can interact, thus increasing the magnitude of the nuclear field fluctuations experienced by the hole spin [1] [89]. This effect can be reduced by constructing larger quantum dots or utilizing materials in which heavy holes have a lighter effective mass, such as strained germanium. As well, new methods of optically cooling nuclear fluctuations [77] [80] may also help to extend coherence times.

The electric tunability of the dot effective g-factor was demonstrated in a number of these experiments, an important functionality with regard to scalability in quantum computing using similar dot architectures in the future. In order to make such measurements possible in the latching regime, the modified spin-to-charge readout technique adapted from Bogan et al. [34] was implemented to allow spin manipulations to be performed in each single-shot experiment despite the unavailability of conventional readout methods such as Pauli spin blockade and Elzerman readout. The voltage detuning of the driving position relative to the measurement position was altered in both the L and R gates until the RF voltage line to the R gate became inoperable. Due to this limitation, the voltage range of the driving position in the L gate was limited by moving into a different dot occupation region (namely, the (1,1) region) for too long a period, potentially producing unexpected effects in the hole spin evolution. A simple extension of this work would be to perform subsequent experiments with this functionality restored. This would enable the further investigation of the effect of dot capacitive coupling to non-adjacent gate voltages on the dot effective g-factor.

In this work, only a single-qubit X-gate was applied via microwave burst manipulation of the L gate. This signal was produced in the in-phase ("I") channel of the MW generator; to demonstrate full single-qubit control and study phase dependence in the spin rotation, a Y-gate operation could be performed using the quadrature ("Q") output channel. In order to continue the employment of the latched readout technique in future experiments involving two-qubit gates, it would be necessary to construct triple- or quadruple-dot devices, creating an additional dot to act as a qubit and possibly a corresponding memory register.

Despite the observed counterbalancing of the increased spin-orbit coupling by the dephasing effects of the increased nuclear field fluctuation and light hole-heavy hole mixing, gallium arsenide remains a promising material for the implementation of hybrid quantum devices. Its direct band gap makes it a natural candidate for such applications as photon-to-spin transducers, linking photonic and electronic quantum information devices. This functionality would be essential to create optoelectronic quantum networks in the future. Other semiconductors with longer reported coherence times such as silicon and germanium have indirect band gaps, reducing their applicability in this regard and maintaining the importance of GaAs for the future.

References

[1] V. Marton, A. Sachrajda, M. Korkusinski, A. Bogan and S. Studenikin, "Coherence Characteristics of a GaAs Single Heavy-Hole Spin Qubit Using a Modified Single-Shot Latching Readout Technique," *Nanomaterials*, vol. 13, no. 5, p. 950, 2023.

[2] R. Landauer, "Irreversibility and Heat Generation in the Computing Process," *IBM Journal of Research and Development*, vol. 5, no. 3, pp. 183-191, 1961.

[3] Y. I. Manin, "Computable and Uncomputable," in *Mathematics as Metaphor: Selected Essays of Yuri I. Manin*, Providence, American Mathematical Society, 2007, pp. 77-78.

[4] R. Feynman, *Simulating Physics with Computers,* Pasadena: California Institute of Technology, 1981.

[5] D. Deutsch and R. Jozsa, "Rapid solution of problems by quantum computation," in *Proceedings of the Royal Society of London. Series A: Mathematical and Physical Sciences*, London, 1992.

[6] L. K. Grover, "A fast quantum mechanical algorithm for database search," in *Proceedings of the twenty-eighth annual ACM symposium on Theory of computing - STOC '96*, Philadelphia, 1996.

[7] P. W. Shor, "Algorithms for quantum computation: discrete logarithms and factoring," in *Proceedings 35th Annual Symposium on Foundations of Computer Science*, Santa Fe, 1994.

[8] D. P. DiVincenzo, "The Physical Implementation of Quantum Computation," *Fortschritte der Physik,* vol. 48, no. 9-11, pp. 771-783, 2000.

[9] J. I. Cirac and P. Zoller, "Quantum Computations with Cold Trapped Ions," *Physical Review Letters,* vol. 74, no. 20, pp. 4091-4094, 1994.

[10] C. Monroe, D. M. Meekhof, B. E. King, W. M. Itano and D. J. Wineland, "Demonstration of a Fundamental Quantum Logic Gate," *Physical Review Letters,* vol. 75, no. 25, pp. 4714-4717, 1995.

[11] D. G. Cory, A. F. Fahmy and T. F. Havel, "Ensemble quantum computing by NMR spectroscopy," in *Proceedings of the National Academy of Sciences*, 1997.

[12] D. Loss and D. P. DiVincenzo, "Quantum computation with quantum dots," *Physical Review A,* vol. 57, no. 1, pp. 120-126, 1997.

[13] A. Barenco, D. Deutsch and A. Ekert, "Conditional Quantum Dynamics and Logic Gates," *Physical Review Letters,* vol. 74, no. 20, pp. 4083-4086, 1995.

[14] A. M. Tyryshkin, S. Tojo, J. J. L. Morton, H. Riemann, N. V. Abrosimov, P. Becker, H.-J. Pohl, T. Schenkel, M. L. W. Thewalt, K. M. Itoh and S. A. Lyon, "Electron spin coherence exceeding seconds in high-purity silicon," *Nature Materials,* vol. 11, no. 2, p. 143–147, 2011.

[15] K. Saeedi, S. Simmons, J. Z. Salvail, P. Dluhy, H. Riemann, N. V. Abrosimov, P. Becker, H.-J. Pohl, J. J. L. Morton and M. L. W. Thewalt, "Room-Temperature Quantum Bit Storage Exceeding 39 Minutes Using Ionized Donors in Silicon-28," *Science,* vol. 342, no. 6160, p. 830–833, 2013.

[16] N. W. Hendrickx, D. P. Franke, A. Sammak, G. Scappucci and M. Veldhorst, "Fast two-qubit logic with holes in germanium," *Nature,* vol. 577, no. 7791, p. 487–491, 2020.

[17] J. M. Nichol, L. A. Orona, S. P. Harvey, S. Fallahi, G. C. Gardner, M. J. Manfra and A. Yacoby, "High-fidelity entangling gate for double-quantum-dot spin qubits," *npj Quantum Information,* vol. 3, no. 1, 2017.

[18] L. A. Tracy, T. W. Hargett and J. L. Reno, "Few-hole double quantum dot in an undoped GaAs/AlGaAs heterostructure," *Applied Physics Letters,* vol. 104, no. 12, 2014.

[19] X. L. Liu, D. Hug and L. M. K. Vandersypen, "Gate-defined graphene double quantum dot and excited state spectroscopy," *Nano Letters,* vol. 10, no. 5, pp. 1623-1627, 2010.

[20] L. Gaudreau, G. Granger, A. Kam, G. C. Aers, S. A. Studenikin, P. Zawadzki, M. Pioro-Ladrière, Z. R. Wasilewski and A. S. Sachrajda, "Coherent control of three-spin states in a triple quantum dot," *Nature Physics,* vol. 8, no. 1, pp. 54-58, 2011.

[21] M. R. Delbecq, T. Nakajima, P. Stano, T. Otsuka, S. Amaha, J. Yoneda, K. Takeda, G. Allison, A. Ludwig, A. D. Wieck and S. Tarucha, "Quantum Dephasing in a Gated GaAs Triple Quantum Dot due to Nonergodic Noise," *Physical Review Letters,* vol. 116, no. 4, 2016.

[22] A. Noiri, K. Kawasaki, T. Otsuka, T. Nakajima, J. Yoneda, S. Amaha, M. R. Delbecq, K. Takeda, G. Allison, A. Ludwig, A. D. Wieck and S. Tarucha, "A triangular triple quantum dot with tunable tunnel couplings," *Semiconductor Science and Technology,* vol. 32, no. 8, 2017.

[23] T. Otsuka, T. Nakajima, M. R. Delbecq, S. Amaha, J. Yoneda, K. Takeda, G. Allison, T. Ito, R. Sugawara, A. Noiri, A. Ludwig, A. D. Wieck and S. Tarucha, "Single-electron Spin Resonance in a Quadruple Quantum Dot," *Scientific Reports,* vol. 6, no. 1, 2016.

[24] T. Ito, T. Otsuka, S. Amaha, M. R. Delbecq, T. Nakajima, J. Yoneda, K. Takeda, G. Allison, A. Noiri, K. Kawasaki and S. Tarucha, "Detection and control of charge states in a quintuple quantum dot," *Scientific Reports,* vol. 6, no. 1, 2016.

[25] C. Volk, A. M. J. Zwerver, U. Mukhopadhyay, P. T. Eendebak, C. J. van Diepen, J. P. Dehollain, T. Hensgens, T. Fujita, C. Reichl, W. Wegscheider and L. M. K. Vandersypen, "Loading a quantum-dot based "Qubyte" register," *npj Quantum Information,* vol. 5, no. 1, 2019.

[26] J. Fischer, W. A. Coish, D. V. Bulaev and D. Loss, "Spin decoherence of a heavy hole coupled to nuclear spins in a quantum dot," *Physical Review B,* vol. 78, no. 15, 2008.

[27] J. Fischer and D. Loss, "Hybridization and Spin Decoherence in Heavy-Hole Quantum Dots," *Physical Review Letters,* vol. 105, no. 26, 2010.

[28] X. J. Wang, S. Chesi and W. A. Coish, "Spin-Echo Dynamics of a Heavy Hole in a Quantum Dot," *Physical Review Letters,* vol. 109, no. 23, 2012.

[29] F. Nichele, A. N. Pal, R. Winkler, C. Gerl, W. Wegscheider, T. Ihn and K. Ensslin, "Spin-orbit splitting and effective masses in p-type GaAs two-dimensional hole gases," *Physical Review B,* vol. 89, no. 8, 2014.

[30] M. Ciorga, A. S. Sachrajda, P. Hawrylak, C. Gould, P. Zawadzki, S. Jullian, Y. Feng and Z. Wasilewski, "Addition spectrum of a lateral dot from Coulomb and spin-blockade spectroscopy," *Physical Review B,* vol. 61, no. 24, pp. R16315-R16318, 2000.

[31] P. C. Spruijtenburg, J. Ridderbos, F. Mueller, A. W. Leenstra, M. Brauns, A. A. I. Aarnink, W. G. van der Wiel and F. A. Zwanenburg, "Single-hole tunneling through a two-dimensional hole gas in intrinsic silicon," *Applied Physics Letters,* vol. 102, no. 19, 2013.

[32] A. Bogan, S. A. Studenikin, M. Korkusinski, G. C. Aers, L. Gaudreau, P. Zawadzki, A. S. Sachrajda, L. A. Tracy, J. L. Reno and T. W. Hargett, "Consequences of Spin-Orbit Coupling at the Single Hole Level: Spin-Flip Tunneling and the Anisotropic g Factor," *Physical Review Letters,* vol. 118, no. 16, 2017.

[33] L. A. Tracy, J. L. Reno and T. W. Hargett, "Fabrication and Characterization of a Single Hole Transistory in p-type GaAs/AlGaAs Heterostructures," Sandia National Labs, Albuquerque, 2015.

[34] A. Bogan, S. Studenikin, M. Korkusinski, L. Gaudreau, P. Zawadzki, A. Sachrajda, L. Tracy, J. Reno and T. Hargett, "Single hole spin relaxation probed by fast single-shot latched charge sensing," *Communications Physics,* vol. 2, no. 1, 2019.

[35] R. Winkler, "Electron and Hole States in Quasi-Two-Dimensional Systems," in *Spin-orbit Coupling Effects in Two-Dimensional Electron and Hole Systems*, Erlangen, Springer Tracts in Modern Physics, 2003, pp. 47-48.

[36] T. Flissikowski, I. A. Akimov, A. Hundt and F. Henneberger, "Single-hole spin relaxation in a quantum dot," *Physical Review B,* vol. 68, no. 16, 2003.

[37] A. I. Ekimov and A. A. Onushchenko, "Quantum size effect in three-dimensional microscopic semiconductor crystals," *Journal of Experimental and Theoretical Physics Letters,* vol. 34, no. 6, pp. 363-366, 1981.

[38] R. Dingle, H. L. Störmer, A. C. Gossard and W. Wiegmann, "Electron mobilities in modulation-doped semiconductor heterojunction superlattices," *Applied Physics Letters,* vol. 33, no. 7, pp. 665-667, 1978.

[39] L. B. A. Gaudreau, M. Korkusinski, S. Studenikin, D. G. Austing and A. S. Sachrajda, "Entanglement distribution schemes employing coherent photon-to-spin conversion in

semiconductor quantum dot circuits," *Semiconductor Science and Technology,* vol. 9, p. 32, 2017.

[40] F. H. L. Koppens, C. Buizert, K. J. Tielrooij, I. T. Vink, K. C. Nowack, T. Meunier, L. P. Kouwenhoven and L. M. K. Vandersypen, "Driven coherent oscillations of a single electron spin in a quantum dot," *Nature,* vol. 442, no. 7104, pp. 766-771, 2006.

[41] S. Studenikin, M. Korkusinski, M. Takahashi, J. Ducatel, A. Padawer-Blatt, A. Bogan, D. G. Austing, L. Gaudreau, P. Zawadzki, A. Sachrajda, Y. Hirayama, L. Tracy, J. Reno and T. Hargett, "Electrically tunable effective g-factor of a single hole in a lateral GaAs/AlGaAs quantum dot," *Communications Physics,* vol. 2, no. 1, 2019.

[42] J. M. Elzerman, R. Hanson, L. H. Willems van Beveren, B. Witkamp, L. M. K. Vandersypen and L. P. Kouwenhoven, "Single-shot read-out of an individual electron spin in a quantum dot," *Nature,* vol. 430, no. 6998, p. 431–435, 2004.

[43] J. R. Petta, A. C. Johnson, J. M. Taylor, E. A. Laird, A. Yacoby, M. D. Lukin, C. M. Marcus, M. P. Hanson and A. C. Gossard, "Coherent Manipulation of Coupled Electron Spins in Semiconductor Quantum Dots," *Science,* vol. 309, no. 5744, p. 2180–2184, 2005.

[44] G. Burkard, T. D. Ladd, A. Pan, J. M. Nichol and J. R. Petta, "Semiconductor spin qubits," *Reviews of Modern Physics,* vol. 95, no. 2, 2023.

[45] D. M. Zajac, A. J. Sigillito, M. Russ, F. Borjans, J. M. Taylor, G. Burkard and J. R. Petta, "Resonantly driven CNOT gate for electron spins," *Science,* vol. 359, no. 6374, p. 439–442, 2018.

[46] T. M. Lu, D. R. Luhman, K. Lai, D. C. Tsui, L. N. Pfeiffer and K. W. West, "Undoped high mobility two-dimensional hole-channel GaAs/Al(x)Ga(1−x)As heterostructure field-effect transistors with atomic-layer-deposited dielectric," *Applied Physics Letters,* vol. 90, no. 11, 2007.

[47] J. Ducatel, A. Padawer-Blatt, A. Bogan, M. Korkusinski, P. Zawadzki, A. Sachrajda, S. Studenikin, L. Tracy, J. Reno and T. Hargett, "Single-hole couplings in GaAs/AlGaAs double dots probed with transport and EDSR spectroscopy," *Applied Physics Letters,* vol. 118, no. 21, 2021.

[48] A. B. Zorin, "The thermocoax cable as the microwave frequency filter for single electron circuits," *Review of Scientific Instruments,* vol. 66, no. 8, p. 4296–4300, 1995.

[49] A. V. Feshchenko, O.-P. Saira, J. T. Peltonen and J. P. Pekola, "Thermal conductance of Nb thin films at sub-kelvin temperatures," *Scientific Reports,* vol. 7, no. 1, 2017.

[50] B. J. van Wees, H. van Houten, C. W. J. Beenakker, J. G. Williamson, L. P. Kouwenhoven, D. van der Marel and C. T. Foxon, "Quantized conductance of point contacts in a two-dimensional electron gas," *Physical Review Letters,* vol. 60, no. 9, p. 848–850, 1988.

[51] M. Field, C. G. Smith, M. Pepper, D. A. Ritchie, J. E. F. Frost, G. A. C. Jones and D. G. Hasko, "Measurements of Coulomb blockade with a noninvasive voltage probe," *Physical Review Letters,* vol. 70, no. 9, pp. 1311-1314, 1993.

[52] D. V. Bulaev and D. Loss, "Spin Relaxation and Decoherence of Holes in Quantum Dots," *Physical Review Letters,* vol. 95, no. 7, 2005.

[53] S. K. Watson, R. M. Potok, C. M. Marcus and V. Umansky, "Experimental Realization of a Quantum Spin Pump," *Physical Review Letters,* vol. 91, no. 25, 2003.

[54] L. P. Rokhinson, V. Larkina, Y. B. Lyanda-Geller, L. N. Pfeiffer and K. W. West, "Spin Separation in Cyclotron Motion," *Physical Review Letters,* vol. 93, no. 14, 2004.

[55] E. I. Rashba, "Spin Dynamics and Spin Transport," *Journal of Superconductivity,* vol. 18, no. 2, pp. 137-144, 2005.

[56] F. Nichele, S. Chesi, S. Hennel, A. Wittmann, C. Gerl, W. Wegscheider, D. Loss, T. Ihn and K. Ensslin, "Characterization of Spin-Orbit Interactions of GaAs Heavy Holes Using a Quantum Point Contact," *Physical Review Letters,* vol. 113, no. 4, 2014.

[57] H. A. Kramers, "Théorie générale de la rotation paramagnétique dans les cristaux," in *Proceedings of the Royal Netherlands Academy of Arts and Sciences*, Amsterdam, 1930.

[58] P. Zeeman, "Over de invloed eener magnetisatie op den aard van het door een stof uitgezonden licht [On the influence of magnetism on the nature of the light emitted by a substance]," in *Koninklijk Akademie van Wetenschappen te Amsterdam*, Amsterdam, 1896.

[59] W. I. L. Lawrie, N. W. Hendrickx, F. van Riggelen, M. Russ, L. Petit, A. Sammak, G. Scappucci and M. Veldhorst, "Spin Relaxation Benchmarks and Individual Qubit Addressability for Holes in Quantum Dots," *Nano Letters,* vol. 20, no. 10, p. 7237–7242, 2020.

[60] H. M. Sevian and J. L. Skinner, "T_2 can be greater than $2T_1$," *The Journal of Chemical Physics,* vol. 91, no. 3, p. 1775–1782, 1989.

[61] I. I. Rabi, "Space Quantization in a Gyrating Magnetic Field," *Physical Review,* vol. 51, no. 8, p. 652–654, 1937.

[62] I. I. Rabi, J. R. Zacharias, S. Millman and P. Kusch, "A New Method of Measuring Nuclear Magnetic Moment," *Physical Review,* vol. 53, no. 4, p. 318, 1938.

[63] E. I. Rashba, "Properties of semiconductors with an extremum loop. I. Cyclotron and combinational resonance in a magnetic field perpendicular to the plane of the loop," *Soviet Physics, Solid State,* vol. 2, pp. 1109-1122, 1960.

[64] E. I. Rashba and A. L. Efros, "Orbital Mechanisms of Electron-Spin Manipulation by an Electric Field," *Physical Review Letters,* vol. 91, no. 12, 2003.

[65] V. N. Golovach, M. Borhani and D. Loss, "Electric-dipole-induced spin resonance in quantum dots," *Physical Review B,* vol. 74, no. 16, 2006.

[66] S. Studenikin, M. Korkusinski, A. Bogan, L. Gaudreau, D. G. Austing, A. S. Sachrajda, L. Tracy, J. Reno and T. Hargett, "Single-hole physics in GaAs/AlGaAs double quantum dot system with

strong spin–orbit interaction," *Semiconductor Science and Technology,* vol. 36, no. 5, p. 053001, 2021.

[67] F. H. L. Koppens, D. Klauser, W. A. Coish, K. C. Nowack, L. P. Kouwenhoven, D. Loss and L. M. K. Vandersypen, "Universal Phase Shift and Nonexponential Decay of Driven Single-Spin Oscillations," *Physical Review Letters,* vol. 99, no. 10, 2007.

[68] N. F. Ramsey, "A Molecular Beam Resonance Method with Separated Oscillating Fields," *Physical Review,* vol. 78, no. 6, p. 695–699, 1950.

[69] P. Stano and D. Loss, "Review of performance metrics of spin qubits in gated semiconducting nanostructures," *Nature Reviews Physics,* vol. 4, no. 10, p. 672–688, 2022.

[70] E. L. Hahn, "Spin Echoes," *Physical Review,* vol. 80, no. 4, p. 580–594, 1950.

[71] H. Y. Carr and E. M. Purcell, "Effects of Diffusion on Free Precession in Nuclear Magnetic Resonance Experiments," *Physical Review,* vol. 94, no. 3, p. 630–638, 1954.

[72] J. Corrigan, J. P. Dodson, B. Thorgrimsson, S. F. Neyens, T. J. Knapp, T. McJunkin, S. N. Coppersmith and M. A. Eriksson, "Latched readout for the quantum dot hybrid qubit," *Applied Physics Letters,* vol. 122, no. 7, 2023.

[73] J. Yoneda, T. Otsuka, T. Nakajima, T. Takakura, T. Obata, M. Pioro-Ladrière, H. Lu, C. J. Palmstrøm, A. C. Gossard and S. Tarucha, "Fast Electrical Control of Single Electron Spins in Quantum Dots with Vanishing Influence from Nuclear Spins," *Physical Review Letters,* vol. 113, no. 26, 2014.

[74] T. Nakajima, A. Noiri, K. Kawasaki, J. Yoneda, P. Stano, S. Amaha, T. Otsuka, K. Takeda, M. R. Delbecq, G. Allison, A. Ludwig, A. D. Wieck, D. Loss and S. Tarucha, "Coherence of a Driven Electron Spin Qubit Actively Decoupled from Quasistatic Noise," *Physical Review X,* vol. 10, no. 1, 2020.

[75] E. Vahapoglu, J. P. Slack-Smith, R. C. C. Leon, W. H. Lim, F. E. Hudson, T. Day, J. D. Cifuentes, T. Tanttu, C. H. Yang, A. Saraiva, N. V. Abrosimov, H.-J. Pohl, M. L. W. Thewalt, A. Laucht, A. S. Dzurak and J. J. Pla, "Coherent control of electron spin qubits in silicon using a global field," *npj Quantum Information,* vol. 8, no. 1, 2022.

[76] B. Undseth, X. Xue, M. Mehmandoost, M. Rimbach-Russ, P. T. Eendebak, N. Samkharadze, A. Sammak, V. V. Dobrovitski, G. Scappucci and L. M. K. Vandersypen, "Nonlinear Response and Crosstalk of Electrically Driven Silicon Spin Qubits," *Physical Review Applied,* vol. 19, no. 4, 2023.

[77] G. N. Nguyen, C. Spinnler, M. R. Hogg, L. Zhai, A. Javadi, C. A. Schrader, M. Erbe, M. Wyss, J. Ritzmann, H.-G. Babin, A. D. Wieck, A. Ludwig and R. J. Warburton, "Enhanced Electron Spin Coherence in a GaAs Quantum Emitter," *Physical Review Letters,* vol. 131, no. 21, 2023.

[78] P. Stano, T. Nakajima, A. Noiri, S. Tarucha and D. Loss, "Dynamical nuclear spin polarization in a quantum dot with an electron spin driven by electric dipole spin resonance," *Physical Review B,* vol. 108, no. 15, 2023.

[79] R. Kaji, S. Ohno, T. Hozumi and S. Adachi, "Effects of valence band mixing on hole spin coherence via hole-nuclei hyperfine interaction in InAlAs quantum dots," *Journal of Applied Physics,* vol. 113, no. 20, 2013.

[80] D. M. Jackson, U. Haeusler, L. Zaporski, J. H. Bodey, N. Shofer, E. Clarke, M. Hugues, M. Atatüre, C. Le Gall and D. A. Gangloff, "Optimal Purification of a Spin Ensemble by Quantum-Algorithmic Feedback," *Physical Review X,* vol. 12, no. 3, 2022.

[81] N. Piot, B. Brun, V. Schmitt, S. Zihlmann, V. P. Michal, A. Apra, J. C. Abadillo-Uriel, X. Jehl, B. Bertrand, H. Niebojewski, L. Hutin, M. Vinet, M. Urdampilleta, T. Meunier, Y.-M. Niquet, R. Maurand and S. D. Franceschi, "A single hole spin with enhanced coherence in natural silicon," *Nature Nanotechnology,* vol. 17, no. 10, p. 1072–1077, 2022.

[82] J. Medford, Ł. Cywiński, C. Barthel, C. M. Marcus, M. P. Hanson and A. C. Gossard, "Scaling of Dynamical Decoupling for Spin Qubits," *Physical Review Letters,* vol. 108, no. 8, 2012.

[83] D. Jirovec, A. Hofmann, A. Ballabio, P. M. Mutter, G. Tavani, M. Botifoll, A. Crippa, J. Kukucka, O. Sagi, F. Martins, J. Saez-Mollejo, I. Prieto, M. Borovkov, J. Arbiol, D. Chrastina, G. Isella and G. Katsaros, "A singlet-triplet hole spin qubit in planar Ge," *Nature Materials,* vol. 20, no. 8, p. 1106–1112, 2021.

[84] R. C. C. Y. C. H. H. J. C. C. Leon, J. Camirand Lemyre, T. Tanttu, W. Huang, J. Y. Huang, F. E. Hudson, K. M. Itoh, A. Laucht, M. Pioro-Ladrière, A. Saraiva and A. S. Dzurak, "Bell-state tomography in a silicon many-electron artificial molecule," *Nature Communications,* vol. 12, no. 1, 2021.

[85] J. T. K. O. T. N. T. D. M. R. A. G. H. T. Yoneda, T. Kodera, S. Oda, Y. Hoshi, N. Usami, K. M. Itoh and S. Tarucha, "A quantum-dot spin qubit with coherence limited by charge noise and fidelity higher than 99.9%," *Nature Nanotechnology,* vol. 13, no. 2, p. 102–106, 2017.

[86] S. C. ten Kate, M. F. Ritter, A. Fuhrer, J. Jung, S. G. Schellingerhout, E. P. A. M. Bakkers, H. Riel and F. Nichele, "Small Charging Energies and g-Factor Anisotropy in PbTe Quantum Dots," *Nano Letters,* vol. 22, no. 17, p. 7049–7056, 2022.

[87] W. Sheng, "g-factor tuning in self-assembled quantum dots," *Applied Physics Letters,* vol. 96, no. 13, 2010.

[88] S. Amasha, K. MacLean, I. P. Radu, D. M. Zumbühl, M. A. Kastner, M. P. Hanson and A. C. Gossard, "Electrical Control of Spin Relaxation in a Quantum Dot," *Physical Review Letters,* vol. 100, no. 4, 2008.

[89] A. V. Khaetskii, D. Loss and L. Glazman, "Electron Spin Decoherence in Quantum Dots due to Interaction with Nuclei," *Physical Review Letters,* vol. 88, no. 18, 2002.

Appendix A: Capacitive Coupling and Stability Diagram Drift

While tuning the tunneling times of the DQD via gate voltage adjustment, the capacitive coupling of the QDs to each of the gates was investigated. When the voltage applied to a given gate was modified, the boundaries of each charge occupation region in L-R gate voltage parameter space were altered. In order to make reproducible measurements to estimate the tunneling times as displayed in Figure 8.b) and c), it was necessary to locate the new locations of the charge addition and transfer lines in L-R gate voltage parameter space.
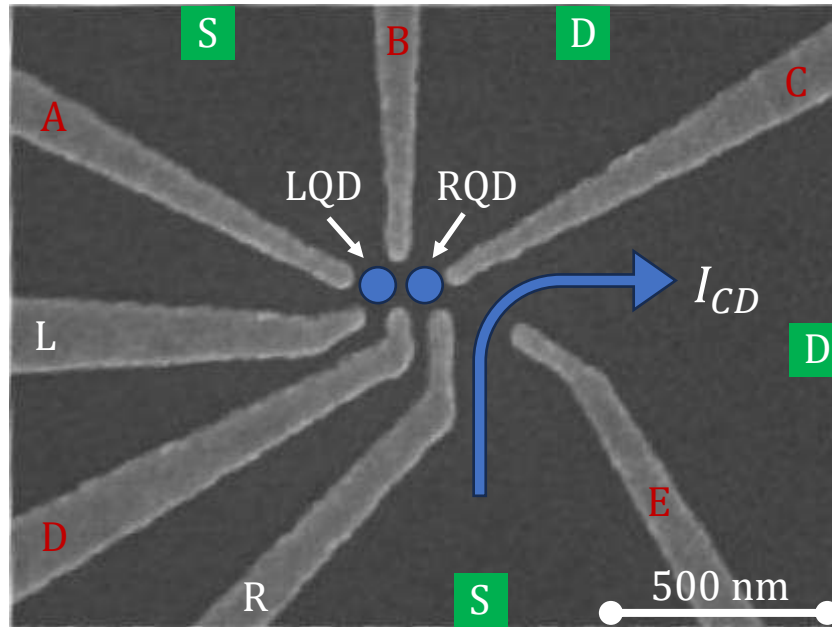
Courtesy of Sandia National Laboratories

Figure A1: Scanning electron microscope image of a GaAs DQD device similar to the one used in this work. All labelling from Figure 1.a) is repeated. Additionally, the five other gates defining the DQD device are labelled in red with the letters A through E for ease of reference.

It was found that the "movement" of the SD structure was linearly correlated with the change in voltage of gates A through D as labelled in Figure A1. (The voltage applied to gate E was chosen in each experiment to maximize charge detection fidelity, as explained in the "Quantum Point Contacts (QPCs)" section above.) By measuring a new SD after modifying the voltage of just one of gates A through D by a set amount (10 mV), the relative magnitudes of their effects on QD occupation could be estimated. A vector for each of these gates was then extracted by calculating the change of location in L-R gate voltage parameter space of the two visible triple points. This allowed for the prediction of the location of the charge occupation region boundaries after any arbitrary gate voltage change, expediting the process of tuning into the latching regime of the right QD.

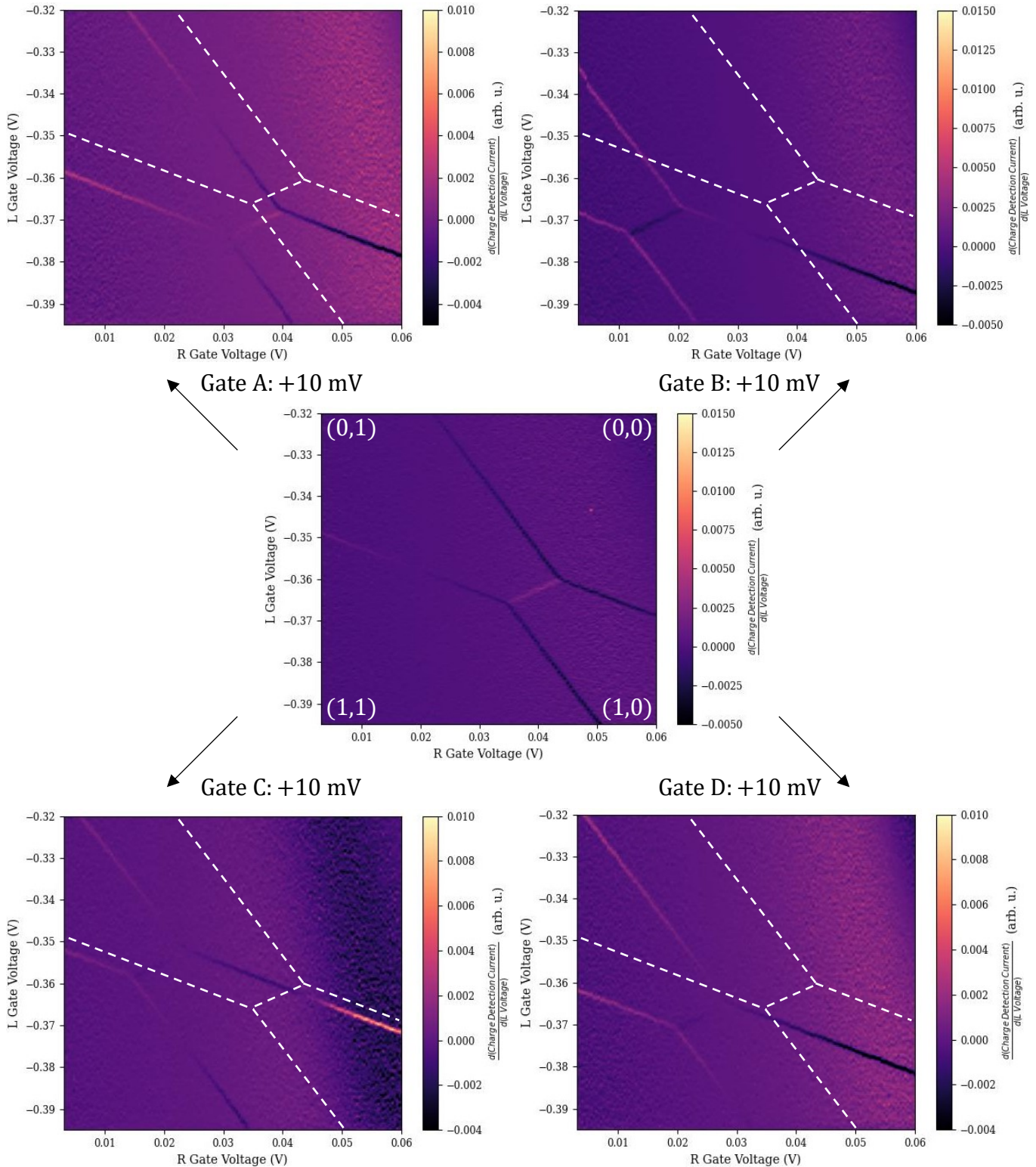The results of these experiments are shown in Figure A2.

Figure A2: Stability diagrams measured to determine the drift of charge occupation regions in L-R gate voltage parameter space. Each of the peripheral diagrams is measured with all gate voltages identical to the central diagram, save for the indicated gate. The position of the occupation region boundaries in the central diagram is overlaid on each of the other diagrams in white dashed lines.

Appendix B: Experimental Procedures and Details

The experimental results shown in the various figures contained in this thesis can be grouped into two categories by their types of data:

Measured in, or derived from, QPC Current	Spin-up proportion derived from QPC Current and subsequently processed
Figures: 2, 6, 8bc, 10a, A2	Figures: 9, 11, 12, 13-24, 25a, 26, 27

Table 2: Lists of figures according to their constituent data types.

Experimental procedures within these categories are largely similar and are explored separately below. In both cases, however, the acquisition time of each experiment was dependent upon the resolution chosen for each independent variable studied. Each measurement was performed on a clock cycle with a length of ~16 ms. When sweeping a gate voltage, a longer delay of a second or more also occurred after each "trace" was completed, as the swept variable was returned to its initial value. In any instance where pulsing parameters were changed via the AWG, a delay of multiple seconds was also required in order to transfer the waveform file to the hardware.

Figures with "Raw" QPC Current

In the experiments shown in these figures, one or more parameters such as gate voltages, applied magnetic field strength, and plunger gate voltage oscillation frequency are altered while the current passing through the QPC is measured. In "heat map" style diagrams measured in QPC current, each point represents one charge detection measurement, and a singular measurement is made for each configuration of the independent variable(s) before moving to the next.

Some peculiarities of the device and hardware placed certain constraints on experimental design. Owing to the experience of researchers who had studied the device previously, it was known that "sweeping" (varying between successive measurements) two gates together created inconsistent results and artifacts that did not appear if the same experiments were repeated when varying one gate at a time. In order to study the effects of pairs of gate voltages, one would be "swept" while the other was "stepped" (varied only after the other gate had "swept" through all of its configurations).

Figures with Spin-Up Proportion Extracted

In the experiments shown in these figures, a large number of single-shot experiments were performed consecutively without changing the configuration of gate voltages, pulsing step durations, or any other independent variable. The proportion of successful transfers of a hole to the latched RQD was determined by grouping the many QPC current measurements at each configuration into two groups and calculating the percentage of measurements indicating that a hole was transferred. Lower (higher) QPC current measurements meant that the RQD contained a hole (was empty) at measurement time. By tuning the QPC gate voltage for each experiment, as explored in the "Quantum

section above, the charge detection values of the two possible occupation states were made to be sufficiently different to be reliably distinguishable.

The number of single-shot cycles performed at each configuration of independent variables was chosen depending on the desired data acquisition time for the experiment. For instance, experiments in which only one independent variable was varied, such as in Figure 11.a), determined the successful transfer proportion across 500 single-shot cycles, while "heat map"-style experiments varying two independent variables, such as in Figures 18.a) and b), only utilised 200 single-shot cycles per point of the figure in order to reduce data acquisition time. Importantly, these single-shot measurements could be performed on successive cycles, as the configuration did not have to be changed.

In some cases, the results of multiple identical experiments performed in succession were averaged (and thus increased the data acquisition time multiplicatively), such as in Figure 18.c). These averaged results were found to produce greater coherence times for Rabi experiments, suggesting that such a method was apt to produce a more accurate estimate of T_{Rabi} for this device. Consequently, all Ramsey, Hahn-echo, and CPMG experiments measuring phase coherence times were averaged in the same fashion, usually for sets of 6 identical experiments. Due to the consecutive measurement of these repetitions, the temporal separation between the experiments to be combined and averaged was on the order of hours.